Theoretically Predicted Production Cross-Section of a W-boson and a charm quark in a proton-proton collisions.

By

Muhammad Irfan

SUBMITTED IN PARTIAL FULFILLMENT OF THE
REQUIREMENT FOR THE DEGREE OF
MASTER OF PHILOSOPHY
AT
DEPARTMENT OF PHYSICS
QUAID-I-AZAM UNIVERSITY,ISLAMABAD

Certificate

The undersigned hereby certify that they have read and recommend to the department of physics for acceptance of thesis entitled **"Theoretically predicted production cross-section of W-boson and a charm quark in a proton-proton collisions"** by **Muhammad Irfan** in partial fullfillment of the requirements for the degree of **Master of Philosophy**.

_____

Supervisor:
Dr. Shamona Fawad Qazi
Associate Professor
Department of Physics
Quaid-i-Azam University
Islamabad.

_____

Submitted Through:
Dr. Kshif Sabeeh
Professor
Department of Physics
Quaid-i-Azam University
Islamabad.

Copyright Notice

Author: **Muhammad Irfan**

Title: **"Theoretically Predicted Production Cross-section of a W-boson and a charm quark in a proton-proton collisions."**

Department: **Physics**

Degree: M.Phil   Convocation: year:

_____

Signature of Author

This thesis is dedicated to *my parents*

Acknowledgments

Muhammad Irfan March 2022.

Abstract

The measurement of W and charm quark production cross section, through hadron collision provides a deep understanding of the structure of proton. The production of W boson and charm are best examples of hard scattering processes at Large Hadron Collider. Cross sections of W and c-quark and their ratios have been experimentally measured by the CMS detector at LHC in proton-proton collisions at various center of mass energies.

We have studied the theoretical prediction of these cross sections in proton-proton collisions at CoM energies, $\sqrt{s} = 13\ TeV$, $13.6\ TeV$ and $14\ TeV$. The prediction are made using MADGRAPH and Parton Distribution Function (PDF) sets, such as CT14nlo, NNPDF3.1nlo, ABMP16nlo, CT10nlo and HERAPDF20.

The inclusive cross-section $\sigma(W^{\pm} + c)$ predicted at 13 TeV is $(1056.319 \pm 11.58 \pm 11.92 \pm 12)$[pb], at 13.6 TeV it is $(1095.14 \pm 11.62 \pm 12.52 \pm 12.60)$[pb] and at 14 TeV it is found to be $(1140.67 \pm 11.38 \pm 11.79 \pm 11.84)$[pb] using CT10nlo PDF. Theoretically predicted production cross section and cross section ratios of $W^{+} + \bar{c}$ and $W^{-} + c$ are compared with the measured results of CMS for 13 TeV only.

Chapter 1

Introduction to Particle Physics

This is the introductory chapter of my thesis deals with the study of the elementary particles and their source. Which includes the detail study about lepton ,quark, mediators and the forces of interactions. There is also a brief taste of unification in the last.

1.1 Elementary Particle Physics

The Elementary particle physics is to answer a question , 'What is matter made of'. at the elementary level. It is a fact that atom/matter empty at subatomic level having chunk of matter. The chunks are smaller in number and have different types such as electron, neutron, proton, meson, vector boson, neutrino and so on. These fundamental particles are copies not just similar but exactly the same. For example if you have seen an electron you have seen them all.

As the elementary particles are vary small so we cannot deal with them like macroscopic bodies. So we have to to use less direct mean means to probe an elementary particle interaction. All the information we get from experiment is one of the three forms i.e scattering, decay and bound state. In scattering, we trigger a target particle with other particle/radiation and record variation in angle of deflection. Decay is a process in which a particle disintegrates and we study their remains. The bound state is when two or more particles combine together and form a bound state and we study their properties in a combined state.

The world of every day life is governed by classical mechanics. But for the particles that travel with a speed near to the speed of light, the classical rules are modified by the general relativity. As they are very small compared to the size of classical objects so classical mechanics is modified by quantum mechanics. So the thing is that, due to small size and higher speed they come under the domain of quantum field theory(which incorporates both relativity and quantum mechanics). There is distinction between type of mechanics and force laws. For example the Newton's universal law of gravitation describes the type of interaction and Newton's laws of motion describes the mechanics of that interaction. Meaning that the interaction tells you about the type of force, and mechanics tells about how to use that force to find its motion.

However, some general features of this behavior have nothing to do with the detail form of the interactions. Instead they follow directly from relativity, quantum mechanics, or from the combination of the two. For example, in relativity, energy and momentum are always conserved, but (rest) is not. Thus the decay $\Delta \to p + \pi$ is perfectly acceptable even though the weight of Δ more than the sum of π and p. In classical physics, where mass is strictly conserved, such a process would not be possible. Furthermore, as we will demonstrate, relativity allows for particles with zero (rest) mass - the concept of a mass-less particle is absurd in classical mechanics. Both photons and gluons have no mass.

1.1.1 Production/Source of Elementary Particles

Some particles such as electron, proton and neutron are stable and from basic constituent of matter. In order to produce electron, there is no problem, just take a piece of matter and heat it electron will come popping out of the matter and, in order to produce a beam of electrons just put that heating piece of metal between positive and negative charge plates. For the production of protons just ionize the ^1_1H atom and you will get proton. From three other sources, other distinct particles can be produce, cosmic rays, particle accelerators and nuclear reactors.

1.1.1.1 Cosmic rays

Cosmic rays are high energy rays/atomic nuclei coming from the outside of the solar system. When these rays interact with the particles in outer atmosphere of earth, they produce a shower of particles, which is showering on us all the time. Source of these rays is something of a mystery but it is believed that it is coming from the active galactic nuclei and supernova explosion of star. The advantage of the comic rays are the free source of particles that have high energy range. But, flux of these rays per unit time is very low that strikes any detector and also they are uncontrollable.

1.1.2 Nuclear reactors

Nuclear reactor is a device used to to initiate and control a fission nuclear chain reaction. When a nucleus disintegrates it produces a variety of particles such as alpha particle (which is a combined state of neutron and proton), beta rays (electron or positron) and gamma rays.

1.1.2.1 Particle Accelerators

In particle accelerators, electrons or protons accelerate to a high speed(relative to the speed of light) and collide with each other or bombard at some stationary target. The resultant particle can be detected by skillful arrangement of absorber and magnetic field. There are some heavier particle in Standard model and in-order to produce heavier particles we need higher collision energy. That is the reason why historically light weight particles were discovered first and with the passage of time the accelerators became more advanced and heavier particles were also discovered.List of particles and their discoveries are listed in Fig. 1.1 Detection of particles

Particle	Year	Discovered	Technique
e^-	1897	Thomson	Discharge in gases
p	1919	Rutherford	Radioactivity
n	1932	Chadwik	Radioactivity
e^+	1933	Anderson	Cosmic-rays
$\mu^{+/-}$	1937	Neddermeyer, Anderson	Cosmic-rays
$\pi^{+/-}$	1947	Powell, Occhialini, Lattes	Cosmic-rays
$K^{+/-}$	1947	Rochester, Butler	Cosmic-rays
π^0	1949	Bjorklund	Accelerator
K^0	1951	Armenteros	Cosmic-rays
Λ^0	1950	Hopper	Cosmic-rays
anything else	1955 $\rightarrow$ today	various groups	Accelerators

Figure 1.1: Above figure show the particle there discovery and the technique used

will be discussed in the next chapter in detail.

1.1.3 The Standard Model

The Standard Model is a theory that classifies all known elementary particles as well as three of the universe's four fundamental forces. It also explains their masses, charge and spin. Despite the fact that the Standard Model is thought to be theoretically self-consistent and has showed huge effectiveness in delivering experimental predictions.

The particles having unknown internal structure are called elementary particles. There are three basic type of elementary particle in Standard model i.e, leptons,

Quarks, Mediators and Higgs boson. All the matter is made of the above three types of particles and Higgs boson is the mass giving particle. On the basis of spin they are known to be fermions or bosons.

1.1.3.1 Leptons

Leptons are spin half particles and are also called fermions. They obey Pauli's exclusion principle, in which no two particles can have the same state in a atom. As they have electric charge, mass and weak charge that is why they interact by electromagnetic force, gravitational force and weak force. They do not have any color charge so they do not interact with each other through strong force. They are
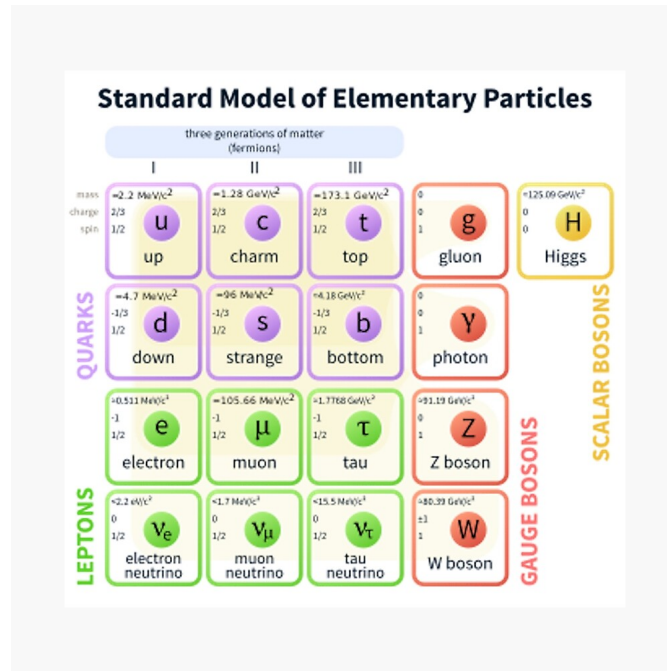

Figure 1.2: Particle in standard model

six in number. Classification on the basis of their charge, electron number, moun number and tau is listed in Table 1.1. They have three generations. There are

Generation	l	L_τ	L_μ	L_e	Q
	e	0	0	1	-1
I	v_e	0	0	1	0
	μ	0	1	0	-1
II	v_μ	0	1	0	0
	τ	1	0	0	-1
III	v_τ	1	0	0	0

Table 1.1: Classification of Fermions

also corresponding six anti-leptons with opposite electric charges, hence there are actually twelve leptons.

1.1.3.2 Quarks

A quark is a basic particle and a fundamental element of matter. There are total six 'flavors' of quarks. quarks are classified on the basis of charge, strangeness, charm, beauty, truth, upness, and downness. Their classification is shown in Table 1.2. For anti-quarks all the quantum numbers will be reversed. Quarks have mass, fractional

q	Q	d	u	s	c	b	t
First Generation							
d	$-\frac{1}{3}$	-1	0	0	0	0	0
u	$\frac{2}{3}$	0	1	0	0	0	0
second generation							
s	$-\frac{1}{3}$	0	0	-1	0	0	0
c	$\frac{2}{3}$	0	0	0	1	0	0
Third generation							
b	$-\frac{1}{3}$	0	0	0	0	-1	0
t	$\frac{2}{3}$	0	0	0	0	0	1

Table 1.2: Quarks Classification

electric charge and colour charge so they can interact by strong, gravitational and electromagnetic force. Quarks have a color charge, although other matter particles are colorless. As a result of phenomena known as color confinement, they are never observed in isolated form.They can be found within hadrons or in quark-gluon plasmas. Hadrons are of two types, baryons(having three quarks) and mesons(having quark and antiquark pair). Baryons are fermions and mesons are bosons.

1.1.3.3 Mediator

The particles that mediate forces between two particles are called mediator. They have integer spin of 0, $1\hbar$ and $2\hbar$, therefore they are also called guage boson. They are four in number. The bosons with spin 1 and 2 are vector boson. Which include photons, gluons, graviton, W and Z boson. The scalar boson (Higgs boson) is the mass giving particle to all the particle in SM. The interaction that exchanges particular mediator is given in Table 1.3

1.1.3.4 Interaction

The particles of Standard Model interact through four type of forces. There are four types of interactions which are mediated by the specific boson listed in Table1.3.

Interaction	Mediator
strong	gluon,G
electromagnetic	photon ,γ
weak	W^{+-} ,Z^o
gravity	graviton, g

Table 1.3: Mediators

The quarks in the neutron and proton, as well as the neutrons and protons within the nuclei, are bound by strong interactions. The gluon, a massless particle, mediates the inter-quark force.

Electromagnetic interactions are responsible for almost all extra-nuclear physics events, including bound states of electrons with nuclei, i.e, atoms and molecules, as well as inter-molecular forces in liquids and solids. Photon exchange mediates these interactions.

The gradual process of nuclear, β-decay, which involves the emission of an electron and neutrino by a radioactive nucleus, is an example of weak interaction. The W and Z^o bosons, with masses 100 times that of the proton, operate as weak interaction mediators.

All kind of particles are affected by gravitational interactions. Gravity is by far the weakest of all the basic interactions on the size of particle physics experiments, yet it is dominating on the scale of the universe. It is thought to be mediated via the graviton which is a spin 2 boson.

1.1.4 Weak Interaction

Neutrinos are the particles that interact only weakly, all leptons and quarks are also weakly interacting. There are three carrier particles, two of which are charged (W^+, W^-) and one of which is neutral (Z), mediate the weak interaction. The mediating particle are heavy with masses of 80.4 GeV [31] for $W^\pm$ bosons and 91.2 GeV for the Z^o boson which makes the interaction range of these boson very short, upto $\approx 2.5 \times 10^{-18}$

The Z boson mediates processes like electron-neutron scattering, whereas the W boson is responsible for the β-decay, which drives the sun's nuclear reactions.

1.1.5 Electromagnetic Interaction

Electromagnetic force is present between all electrically charged particles. Quantum electrodynamics(QED) describes electromagnetic interaction. It is mediated by phton which is massless and charge-less particle. Self coupling is not possible because photon is charge-less particle. The mass-lessness of photon leads to infinite range of EM interaction. The strength of EM interaction decreases as square of distance between them.

The so-called fine structure constant(α) determines the coupling strength of the EM interaction,

$$\alpha_{EW} = e^2/4\pi\epsilon\hbar c \approx 1/137 \tag{1.1}$$

Where ϵ, e and $\hbar$ are the permittivity of free space, electric charge and plank constant respectively. The value may change with energy such as at high energy or short distance, its value increases. This effect is caused by the vaccum polarization(production and absorption of virtual e^+ and e^- pair) around the interacting particles, which changes there charge distribution.

QED is a mathematically abelian gauge theory with a U(1) symmetry, with its Lagrangian written as,

$$L_{U(1)_{EM}} = -\frac{1}{4\mu_o} F_{\mu v}^i F_i^{\mu v} + \bar{\psi}(\iota\gamma^\mu S_\mu - mc^2)\psi \tag{1.2}$$

$$\text{with } F_{\mu v} = \partial_\mu A_v - \partial_v A_\mu$$
$$S_\mu = \partial_\mu - \iota e A_\mu$$

The Quantum field of interaction of charged particles is $\bar{\psi}$ and ψ, S_μ is the covariant derivative, gamma matrix is donated by γ^μ and the electromagnetic tensor is $F_{\mu v}$

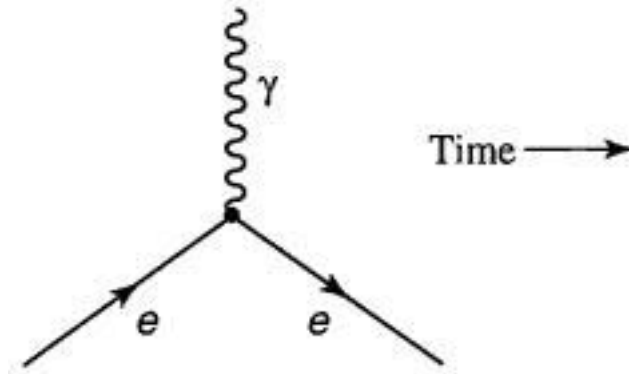In Feynman diagrams, all electromagnetic phenomena is reducible to Fig. 1.3

Figure 1.3: Feynman Diagram

This shows that a particle 'e' having electric charge enters, absorbs a photon (γ) and emits as charge particle 'e'. The time is moving along horizontal to the right. To represent an anti particle just reverse the direction of arrow representing the particle. The line represents real particle and at each vertex conservation of momentum and energy takes place. Some other process are shown in Fig. 1.4 The first Feynman diagram is for Moller scattering, in which two incoming electron

(a) Moller's Scattering

(b) Bhabha Scattering

Figure 1.4: scattering

interact with each other by exchanging a photon and the two electrons exit. While in the second one electron and positron annihilate and form a photon, the photon again produces electron and positron pair.

1.1.6 Electroweak Interaction

The electroweak interaction in particle physics is unification of electromagnetic and weak interaction. At low energy these two interactions are very different from each other. At unification energy which is around 246 GeV it becomes a single force. So at approximately $10^{15}K$ the electromagnetic and and weak forces merge to a single

force called electroweak force. The essential contrasts being the huge masses of the Z and $W^{\pm}$ bosons. Both interactions are explained by an $SU(2)_L \times U(1)_Y$ symmetry in an unified non-abelian gauge theory. The Lagrangian is given as,

$$L_{SU(2)\times U(1)} = \bar{\psi}\iota\gamma_\mu S^\mu \psi - \frac{1}{4}B^\iota_{\mu v}B^{\mu v}_\iota - \frac{1}{4}W^\iota_{\mu v}W^{\mu v}_\iota \tag{1.3}$$

where,

$$
\begin{array}{rcl}
S_\mu & = & \partial_\mu \;+\; \iota\frac{g'}{2}YB_\mu \;+\; \iota\frac{g}{2}\tau_a W^a_\mu \\
B_{\mu v} & = & \partial B_\mu \;-\; \partial B_v \\
W^\iota_{\mu v} & = & \partial_\mu W^\iota_v \;-\; \partial_v W^\iota_\mu \;-\; g\epsilon_{ijk}W^j_\mu W^k_v
\end{array}
$$

ψ represents the quantum field of fermions, γ^μ are the gamma-matrices, , D_μ is the derivative, the gauge coupling is represented by g and g' of the SU(2) and U(1) fields, and $W_{\mu v}$ and $B_{\mu v}$ are the field strength tensors. The hyper charge operator Y in the equation is defined as $Y = 2(Q - I_3)$, where I_3 is the third component of weak iso-spin conserved quantity in electroweak interactions. For left handed fermions, I_3 is $\pm\frac{1}{2}$ and for right handed particles its value is zero. The $W^{\pm}$ pair only with the left handed fermions. The third component of iso-spin has three states(W^+, W^- and W^o) for left handed particles and one neutral singlet state (B^o). The observed $W^{\pm}$ bosons are represented by the W^+ and W^- states. The combination of W^o and B^o gives us the neutral mediators.

In electroweak theory, all the particles are massless which would violate local gauge in-variance condition. Later Higgs, Engler, and Brout proved that when gauge bosons interact with the scalar field $V(\phi)$ and its mediator, the Higgs boson, local gauge invariance is retained and the gauge bosons gain mass. The vacuum expectation value v of the Higgs field is non-zero, which induces spontaneous symmetry breakdown by selecting a vacuum state v and the masses of the elementary particles are generated. The Yukawa coupling for the bosons,

$$m_W = \frac{g}{2}v, m_{Z^o} = \frac{v}{2}\sqrt{g^2 + g\prime^2} \tag{1.4}$$

for fermoins :

$$m_f = \frac{1}{\sqrt{2}}g_f v \tag{1.5}$$

g_f is yukawa coupling where f in subscript represent the flavour of the fermions.

A Z boson or a photon may mediate any process involving just charged particles in the start and final states. As the Z^o boson has greater mass due to this the reactions induced by Z^o are suppressed. In these kind of interaction flavour changing is not allowed. Such interactions are known as neutral currents (NC). The reactions involving $W^{\pm}$ mediator are called charged current(CC). Which can also cause change in flavour of one of the particle in the process. Lepton number is a conserved quantity so the flavour changing in case of lepton is allowed only in same generation. The flavour changing across the generation is possible and is represented by the CKM matrix.

$$\begin{pmatrix} d' \\ s' \\ b' \end{pmatrix} = \begin{pmatrix} X_{ud} & X_{us} & X_{ub} \\ X_{cd} & X_{cs} & X_{cb} \\ X_{td} & X_{ts} & X_{tb} \end{pmatrix} \begin{pmatrix} d \\ s \\ c \end{pmatrix} \tag{1.6}$$

The value of coupling strength is determined experimentally[31] and the value is greater for the elements along the diagonal which are close to one. The contribution of the other elements are small but not zero and therefore the cross generation decay is also allowed.

1.1.7 Strong Interaction

The theory that explains strong interaction is Quantum Chromodynamics(QCD), which describes the structure as well as the interaction. The strong interaction mediated by massless gluons and act only on quarks. Combinations of quarks form hadrons (baryon and meson). Hadron states like Δ^{++}(uuu) require an extra degree of freedom (quantum number), that Pauli exclusion principle holds. The degree of freedom is colour and is interpreted as charge of QCD. Quarks are colour singlet and gluon share bi-colour. QCD is a non-abelian gauge theory with SU(3) symmetry that belongs to the group of non-abelian gauge theories.

(a) Fundamental Feynman Diagram

(b) Three gloun vertices

(c) Four gloun vertices
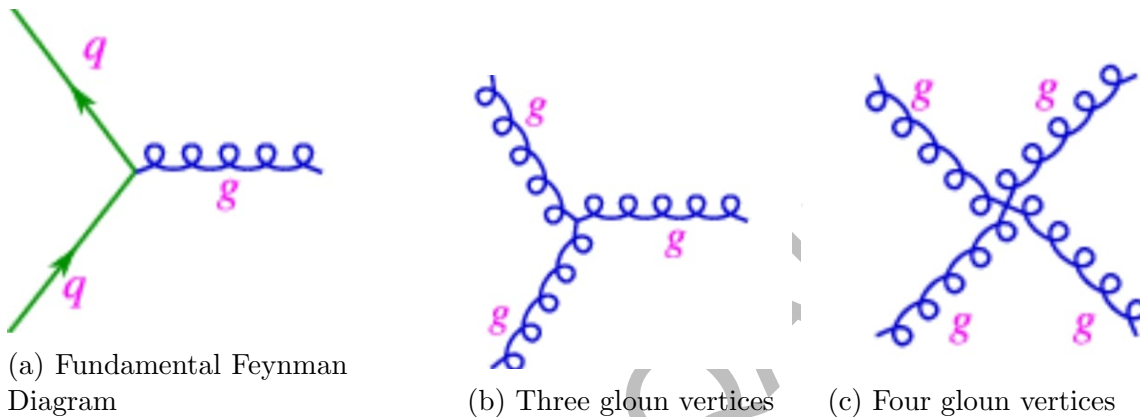
Figure 1.5: Feynman Diagrams of QCD

There are total eight number of gluons. Gluons are bi-cloured with one unit of positive colour and one negative unit. As gluons have colour charge so they can also self couple with each other. So in addition to the fundamental quark-gloun vertices there two more gloun-gloun vertices i.e three gluon vertices and four gluon vertices.

The simplest Feynman diagrams that represent the strong interaction are shown in Fig. 1.5

1.1.8 Limitations of SM

SM gives a succinct and accurate account of the characteristics of the fundamental components, as well as electromagnetic, strong and weak interactions between them. It covers most of the experimental results ranging up to the highest energy upto 1TeV. But it still has limitations, such as gravity is not included. Although neutrinos are thought to be massless, there is mounting evidence that they do have mass. Also, it looks that understanding some of our universe's key properties, including the prevalence of "dark matter" and the enormous matter-antimatter imbalance, would necessitate the development of new and previously undiscovered physics.

1.2 Grand Unification

The coupling constant$(\alpha_e, \alpha_s, \alpha_w)$ strength varies with changing the energy. The α_e value increases with the increase in energy due to vacuum polarization and also the decrease in shielding effect between the charge particle. The rest of the coupling constants decrease with the increase in energy as shown in the Fig. 1.6.
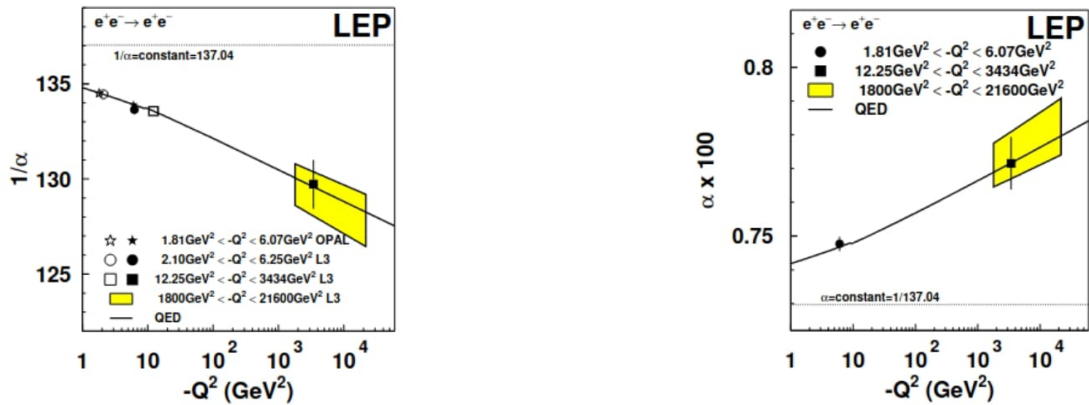
(a) Running coupling constant of QED with energy Q^2

(b) Running coupling constant of QCD with energy Q^2

Figure 1.6: Running Coupling Constants

A Grand Unified Theory (GUT) a is a particle physics model in which the electromagnet, weak and strong guage interaction of the Standard Model interactions are combined into a single force at high energies. There are many theoretical models of GUT but no one has the experimental confirmation. Electromagnetic and weak interaction are unified at high energy and GUT models indicate that the strong and electroweak interactions will merge into a single electro-nuclear interaction at even greater energies. One bigger gauge symmetry characterizes this interaction, resulting in numerous force carriers but a single unified coupling constant as can be seen in Fig. 1.7
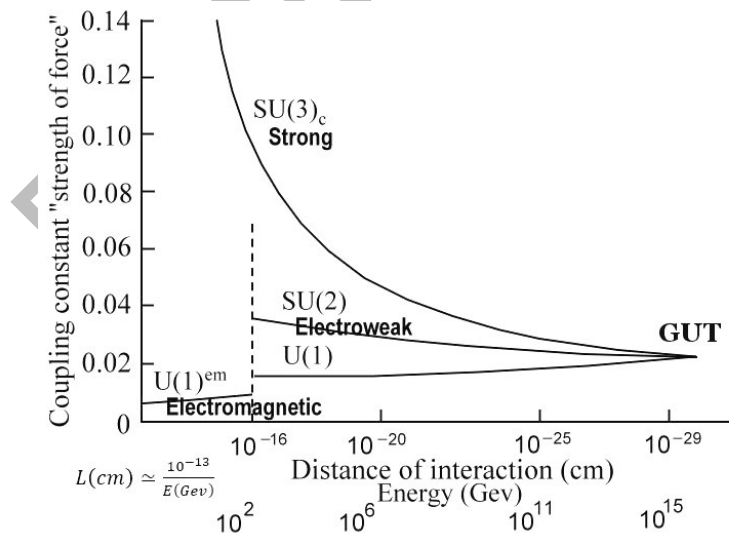
Figure 1.7: Merging of Coupling constant at High Energy

Chapter 2

Compact Moun Solenoid (CMS)

Particle accelerators are the world's most accurate microscopes, allowing researchers to investigate the fundamental building elements of matter in unprecedented detail. Particles are accelerated and collided in an accelerator, and their products are recorded in complicated detection systems.

The Large Hadron Collider (LHC) at CERN is the most advanced machine in terms of energy to date, allowing for the most precise depiction of observable matter's underlying structure. Four complicated multi-purpose experiments at the LHC record and analyse protons or heavy ions collisions, ATLAS[16], CMS[17], ALICE[1] and LHCb [22]. ATLAS and CMS cover most topics of particle physics, LHCb is specially designed for the measurement of CP violation and B hadron decays. By colliding heavy ions ALICE is trying to study Quark Gloun Plasma properties. My work is mostly related to LHC and CMS, so in this chapter we will discus LHC and CMS.

2.1 Large Hadron Collider (LHC)

The Large Hadron Collider, or LHC [26], is enormous scientific equipment that straddles the Franco-Swiss border in Geneva, Switzerland, and is run by the CERN. This accelerator was built to study the particles that existed after the Big Bang for a fraction of a second.
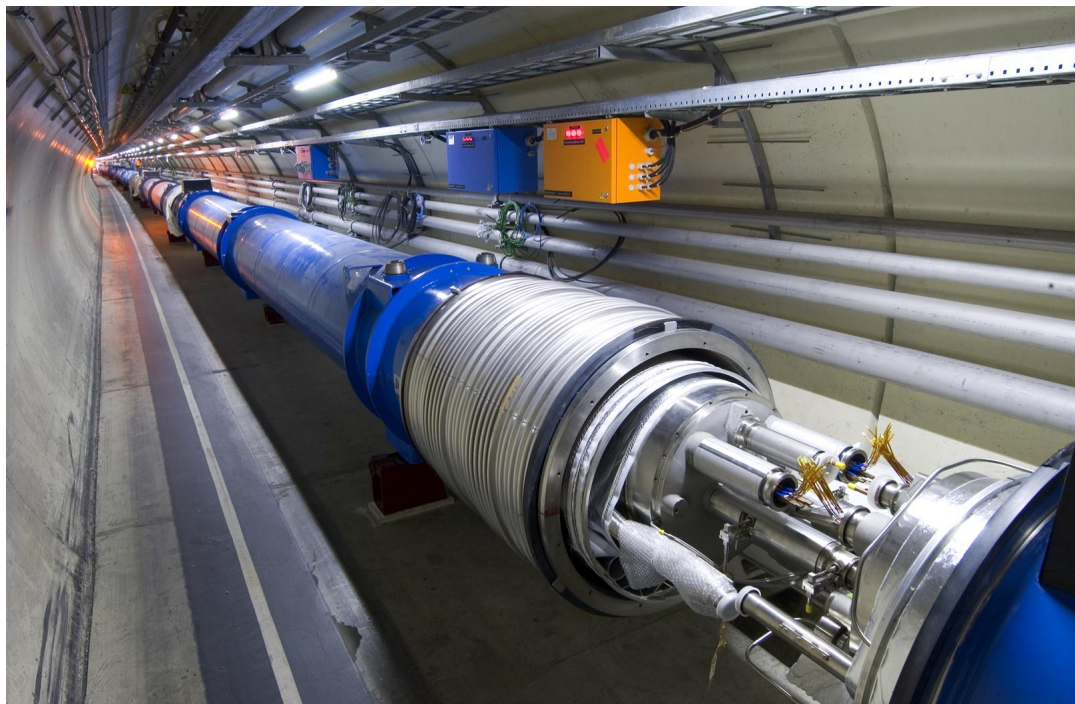
Figure 2.1: LHC at CERN

It has a circumference of 27 km and is installed about 100 m below the ground inside a 3.8 m wide tunnel. The purpose to install it 100 m below the ground is to prevent the outside particles to enter the equipment and also to prevent the produced particles from going out to the environment. It was originally built to collide e^+ and e^- [LEP[14]] beams, now LHC accelerator is used to accelerate proton -proton(pp), proton-lead(pPb) and lead-lead(PbPb) beams upto a center of mass energy of $\sqrt{s}$=14 TeV.

In Fig.2.2 we can see a series of accelerators used to accelerate proton beams to different higher energies step by step. First of all proton ions are produced by ionizing hydrogen atoms in strong electric field and fed into to a linear accelerator. LINAC-3(linear accelerator) is for accelerating heavy ions and LINAC-2 is for accelerating protons. In LINAC the energy of proton is increased upto 50 MeV, from where it is sent into mult-circular booster synchroton which increase its energy upto 1.4 GeV. Then in PS(proton Synchroton) its energy is further increased to 26 GeV. The ions are then directed to SPS (The second largest machine at cern complex), here its energy is further increased up to 450 GeV. There are two circular rings for acceleration of two beams of hadrons in LHC. From SPS the beam of ions is transfered to one of the LHC rings. In LHC there are superconducting radio frequency cavity systems. These cavities oscillate with frequency of 400 MHz. A single cavity made of niobium sprayed on copper, may attain a maximum accelerating voltage of 2 MV, equating to a total of 16 MV for the whole beam. The oscillating field forms bunches of ions (proton or heavy ions), each bunch have a total of 1.15×10^{11} protons or heavy ions and there are approximately 2808 bunches. These bunches are kept rotating by a strong magnetic field in two different tube like rings. These tubes are kept at ultra high vacuum and at very low temperature of 1.9 K. There are 1232 super conducting dipole magnetic made of NbTi to provide the required magnetic field. These magnetic dipole operate at a temperature of 2 K. The cooling
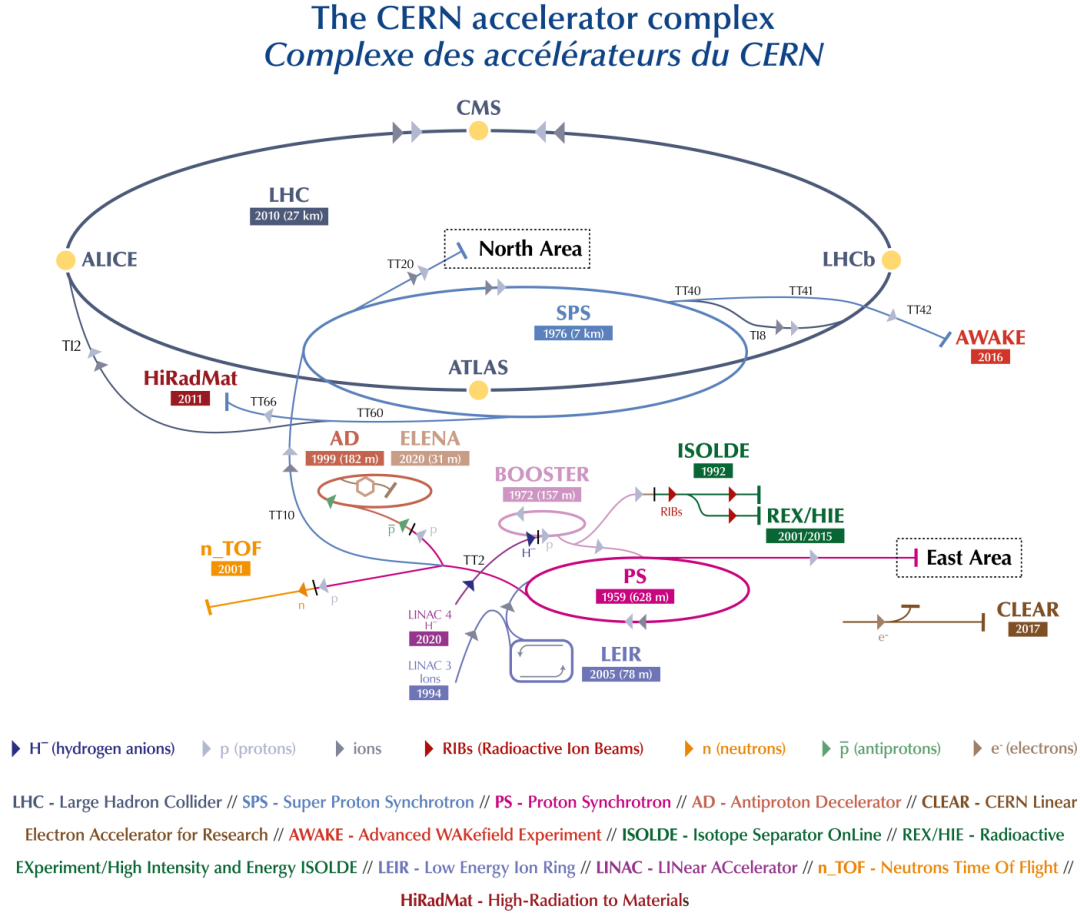
Figure 2.2: Different stages of acceleration and position of different Detector in CERN [33]

is done by liquid helium. These magnets provide about 8 T of magnetic field. In order to overcome the coulomb repulsion between protons there are 392 quadrupoles to keep the beam focused. Once the protons are accelerated to the required energy, they are brought together in order to collide in the four experiments (CMS, ATLAS, ALICE, LHCb). Whenever the energy of colliding particle passes some threshold energy, new particles are produced which open door to new particles and study of their properties.

Some basic terminology and attributes of colliding experiments are as follows,

2.1.0.0.1 Particle flux The number of beam particles passing through a unit area held perpendicular and with velocity v_b is called particle flux it has units of number per second.

$$\Phi = AN_bv_b \tag{2.1}$$

Where Φ represents the flux, A is the perpendicular area, N_b is the number of particles in beam and v_b represents the velocity of the beam.

2.1.0.0.2 Interaction Rate *Number of colliding/interacting particles in unit time* is known as interaction rate R

$$R = \frac{dN}{dt} = f N_1 N_2 \tag{2.2}$$

where f represent the frequency , N_1 and N_2 are the number of particles in beam 1 and 2. The interaction rate for the beam having Gaussian distribution is given as,

$$R = f \frac{N_1 N_2}{4\pi \sigma_x \sigma_y} \tag{2.3}$$

The beam's Gaussian horizontal and vertical widths are σ_x and σ_y , respectively.

2.1.0.0.3 Cross section Probability of an interaction can be shown in terms of effective area known as cross section. It is used to describe the total yield of the interaction regardless of the energy and spacial distribution of emitted particles.

$$A = 4\pi \sigma_x \sigma_y \tag{2.4}$$

Cross section is measured in barn(bn) 1bn $= 10^{-24} cm^2 = 10^{-27} m^2$.

2.1.0.0.4 Luminosity Luminosity is the measure of the number of possible collisions per unit surface during a particular time. The larger the value of luminosity, the greater the number of collisions. It is an important indicator of an accelerator's performance. The instantaneous luminosity depends on many factors such as number of bunches, number of particle in each bunch and also different parameters of the machine. Instantanious Luminosity is given as,

$$L_{inst} = \frac{N_b n_b f \gamma}{4\pi \xi_n \beta^*} F \tag{2.5}$$

Here f is the frequency, N_b is the number of particles in each bunch, n_b represents the number of bunches , γ is the relativistic factor, β is a beta-function at collision point and ξ_n represents the transverse beam emmittance. F is geometric luminosity reduction, this is proportional to the crossing angle of the beams at the point of contact. The instantaneous luminosity for CMS and ATLAS is approximately $10^{34} cm^{-2} s^{-1}$ at the interaction point.

2.2 Compact Moun Solenoid (CMS)

Compact Moun Solenoid (CMS) has its name, Compact, because it has smaller dimensions compared to its mass, it has advanced system for muon detection and solenoid is because having a solenoidal magnet given as a large magnetic field of 4T which is 100,000 times greater than earth magnetic field. CMS and ATLAS are both general purpose detectors but the difference is that there are different magnet system and both have different technical solutions. Compact Moun Solenoid is designed to study the standard model including higgs boson, physics beyond the standard model and search for dark matter particles.

The shape of CMS detector is cylindrical around the LHC beam pipe. In the central part there are layer of cylindrical detectors and in backward and forward regions there are two end-caps. Different components of CMS detector are shown in Fig. 2.3
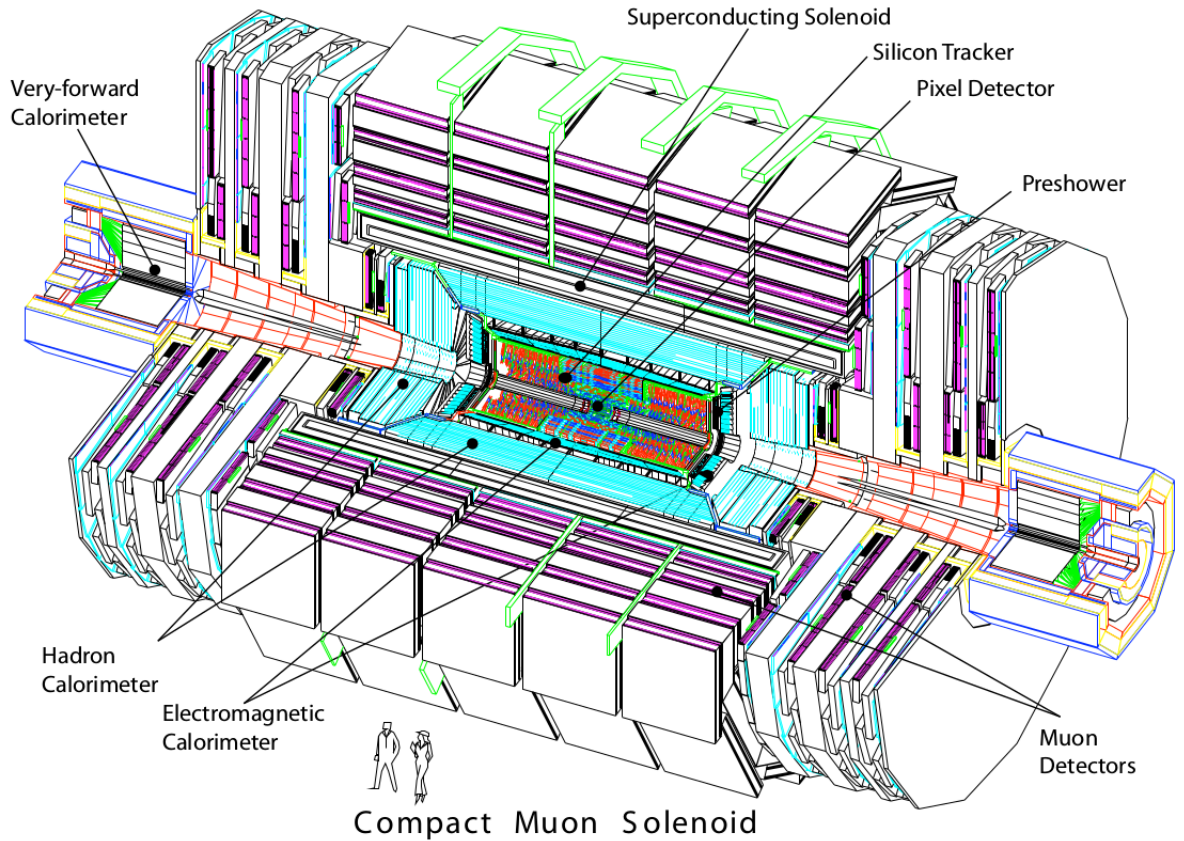
Figure 2.3: CMS detector and its different components [7]

2.3 Co-ordinate System

The nominal point of collision is the origin of the coordinate system which is inside the detector. The direction of x-axis is directed towards the middle of LHC ring, y-axis is pointing upward and the direction of the beam is the z-axis as shown in Fig. 2.4 While using the cylindrical co-ordinates (r, θ, z) the xy-plane is the transverse
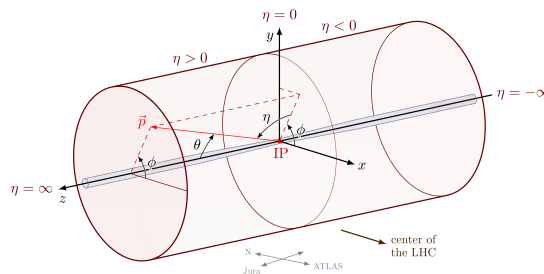
Figure 2.4: CMS Co-ordinate system

plane and azimuthal as well as radial components are defined in it. Z-axis is in the direction of beam, the polar angle(0, -π) is measured referencing to the z-axis whereas azimuthal angle(-π, π) is measured in reference to x-axis.

The trajectories of the particles are displayed on the transverse plane(xy-plane). From the x and y components of momentum of the recorded data, we calculate

transverse momentum P_T as,

$$P_T = \sqrt{P_x^2 + P_y^2} \tag{2.6}$$

Rapidity of the particles is calculated as,

$$y = \frac{1}{2} \ln \frac{(E + p_z)}{(E - p_z)} \tag{2.7}$$

At large energies when we can neglect the mass, it becomes the pseudo-rapidity which is given as,

$$y = \frac{1}{2} \ln \frac{(E + p_z)}{(E - p_z)} \Rightarrow -\frac{1}{2} \tan \frac{\theta}{2} = \eta \tag{2.8}$$

where,

$$\frac{m}{E} \qquad << \qquad 1$$

When a particle escapes detection, the total transverse energy, defined as the transverse missing momentum P_T^{miss}, indicates discrepancy. It is the sum of neutrinos p_T in a hermetic detector, and is the entire negative momentum of a replicated object's projection on the xy-plane.

2.4 Tracker

The central path of LHC , which is hollow is known as tracker. The tracker consists of barrel and two end caps. The tracker is built with silicon pixels and silicon strips. There are 10 tracking layers in barrel region which covers the region from radii 25 cm to 110 cm and along z-axis it covers 120cm. There are four layers in the inner barrel (TIB) and six in the outer barrel (TOB). It also features 12 discs in the end cap area with radii up to 110 cm and z up to 280 cm, 3 inner discs (TID) within the TOB and 9 end cap discs (TEC) outside the TOB with radii up to 110 cm and z up to 280 cm. It is used to measure the particle momenta and their path and to reconstruct the secondary vertices of long lived heavy particles as well as to reconstruct the primary vertices. In CMS there are two tracking devices, the inner(pixel) and outer(strip detector) in the center of CMS as they operate at high radiation region it is most likely to be damage by the high radiation/particle flux. In order to minimize the damage these detectors operate in low temperature environment of -10^oC The tracking system of CMS is illustrated in the Fig. 2.5

There are 15148 modules of strip detectors surrounding the pixel detectors such that there are a total of 9.3 million strips. The inner layers have a spatial resolution of 13–38 m, whereas the outer layers have a spatial resolution of 18–47 m.

2.5 Electromagnetic Calorimeter ECAL

The electromagnetic calorimeter (ECAL)[19] is a device that measures electron and photon energy. With the information supplied by the tracker, it also has a role in identification of particles. The ECAL surrounds the barrel region and is placed inside the solenoid. The ECAL is homogeneous (both absorber and santillator at

(a) The tracking system
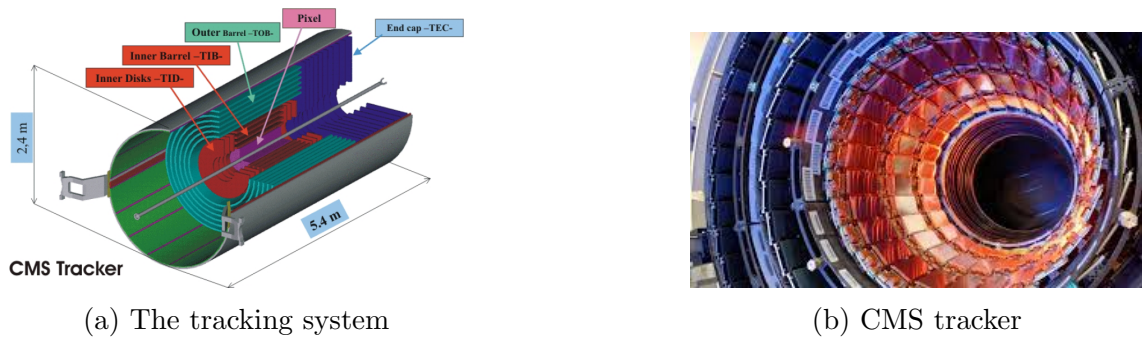
(b) CMS tracker

Figure 2.5: Visualization of CMS Tracker

the same time) calorimeter and its crystals are made of lead tungsten (PbWO_4). The radiation distance of the ECAL is small ($X_o = 0.89 \times 10^{-2}$), having very high density of $8.2 g/cm^3$, and a smaller Moli'ere radius ($R_M = 2.19 \times 10^{-2}$). The ECAL has two regions the barrel and end caps. The pseudorapidity coverage of the two end caps is upto $|\eta| = 3$ and the barrel regions has pseudorapidity of $|\eta| = 1.5$. Each crystal's face cross section in the barrel region is 22×22 mm^2 and 28.6×28.6 mm^2 in the end cap discs. Avalanche photo diodes are glued to the back of each crystal in the barrel region to collect the scintillation light produced by the passing particles, in the end caps for this purpose vaccum photo triodes(VPT) are used. The end caps cover the region between $1.5 < |\eta| < 3.0$.

In the region of $1.65 < |\eta| < 2.61$, a preshower detector is positioned in front of each of the ECAL endcaps. It is a sampling calorimeter, and is made up of alternating layers of lead radiators and silicon strip sensors. Its primary goal is to distinguish photons emitted by $\pi^o \to \gamma\gamma$ decays and the prompt photons. It is also possible to enhance the location determination of electrons and photons.

(a) ECAL Geometry

(b) Insertion of the ECAL super-module in the ECAL barrel
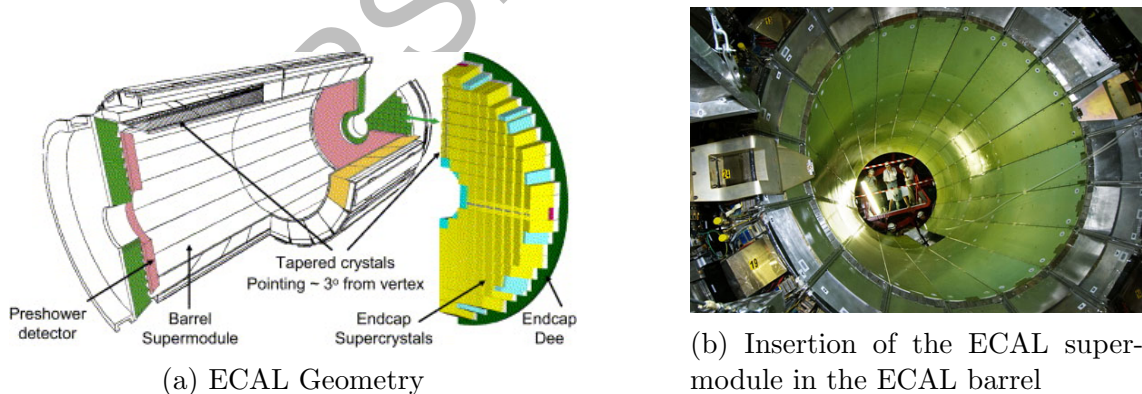
Figure 2.6: Electromagnetic Calorimeter

2.6 Hadronic Calorimeter HCAL

Hadronic calorimeter[18] is used to study the direction of the hadronic jets and the missing P_T(transverse momentum). The existence of neutrinos is indicated by HCAL. There are four subsection of HCAL the hadron barrel (HB), hadron outer (HO), hadron end caps (HE) and hadron forward (HF). The HB and HE

are placed inside the super conducting solenoid and ECAL. HB and HE consist of different interchanging layers of Brass absorber (56.5 mm thick) and scintillating plastic plates (3.7 mm thick)layer. $'eta < 1.4$ is cover by the hadron barrel and the hadron cap cover the region of $1.5 < \eta < 3.0$. There are total 70000 interchanging scintillators in the HCAL which are connected to the hybrid photo diodes by the wavelength shift fibers for readout.

The outer HO helps to identify late showers and improves the energy resolution of high-transverse momentum jets in the middle area and is located outside the magnet due to less space, covering the area $|\eta| < 1.26$. Solenoid is used as absorb-er and before the moun system there is a scintillator plate (10 mm). Two layers of HO scintillator are put on either side of a 19.5 cm thick block of iron due to the poor absorber depth in the very centre region. The last section of HCAL is HF located outside the solenoid covering the area of $3.0 < \eta < 5.0$. The HF(hadron forward) is built of steel plate which is absorber (5 mm) and quarz-fibres which an active medium. It is the most sensitive component to the EM(electromagnet) of hadronic showers. Quartz can withstand the severity of radiation since the forward calorimeter has to deal with an unrivalled particle flow due to the usage of short and long fibres. The photon and electrons form a shower, which is detected by the short fibres. Hadrons generate signal in both regions of the HCAL, accumulating huge amounts of energy in the short fibres. HF calorimeters are designed to verify high-energy jets with a precision of 20 to 30 at 1 Tev.
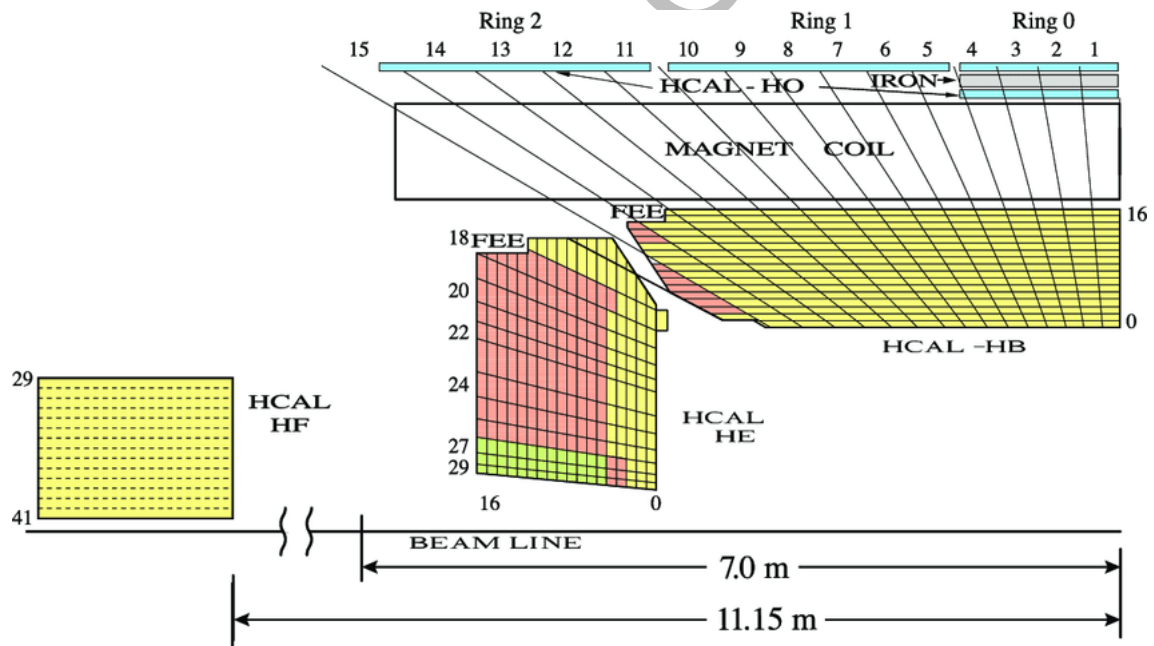
Figure 2.7: Hadron Calorimeter

2.7 Superconducting Solenoid

CMS magnet is at the centre of the experiment. The charged particles' paths were bent along the radius of the CMS emerging from the interaction point by the su-perconducting magnet. The intricacy is like shooting two bullets from a distance of 10 kilometres apart, and even though the interaction is as precise as their meeting

halfway but not combusting in each other. The momentum resolution of the particles may also be calculated since high-energy particles have a less curved path due to the magnetic field. The energy loss is decreased by using liquid helium to chill the to -271.3^oC.

The dipole magnet is used for bending the beam and there are 1232 dipole magnet in the super conducting solenoid and quadrapole magnetic is used to focus the beam nad they 392 in total. The solenoid is surrounded by liquid helium, which allows to flow 19.14 A current with minimal resistance. The flux returns to the iron yoke, which has five wheels and two end caps, each with three discs. The yoke's basic function is to make the magnetic field in the tracker more uniform and to prevent field wandering by returning the solenoid's magnetic flux. For a detailed map of the CMS magnetic field, cosmic mouns are employed for exact replication and MC (Monte Carlo) event simulation. The magnetic field precision of the tracker has been measured to be greater than one.

2.8 Muon System

The muon system[42], which is the heart of the CMS detector, is responsible for muon detection, momentum measurement, and triggering. In the tracker the muon are less impacted by the radiative losses than electron, hence employing them in event reconstruction improves mass resolution. Gaseous particle detectors are placed in the CMS muon system to accommodate for the form of the solenoid magnet and varying background circumstances, as shown in Fig.2.8

The muon detector in CMS barrel which cover the area of $|\eta| < 1.2$ having low muon flux the drift tubes are placed. The drift cells have a tube cross section of 13 $\times 42$ mm^2 and are filled with a mixture of gases consisting of 85 percent Ar and 15 percent CO_2. The end caps having the cathode strip chambers(CSC) covering the region of $0.9 < \eta < 2.4$ the mixture of gases chosen for the CMS detector have 10% CF_4, 40 % of Ar and 50% of carbon dioxide and in between there resistive plate chambers to improve trigger capability and momentum resolution.

The resistive plate chambers are the double chambers that run in avalanche mode to provide reliable operation at high speed. High resistance plates are separated by gas-filled chamber(2 mm) with pick-up readout strips in the middle. RPCs give spatial resolution, a substantially quicker time resolution than the 25 ns across two bunch crossings, and a fair estimate of the traversing particle's transverse momentum.

2.9 Pattern Recognition

Because newly found particles disintegrate into more stable particles, they are often unstable. Particles moving along the tracker create unique signatures, which are subsequently used to identify them in each layer they travel through. It may be determined if a new particle is present or not, as seen in Fig. 2.9
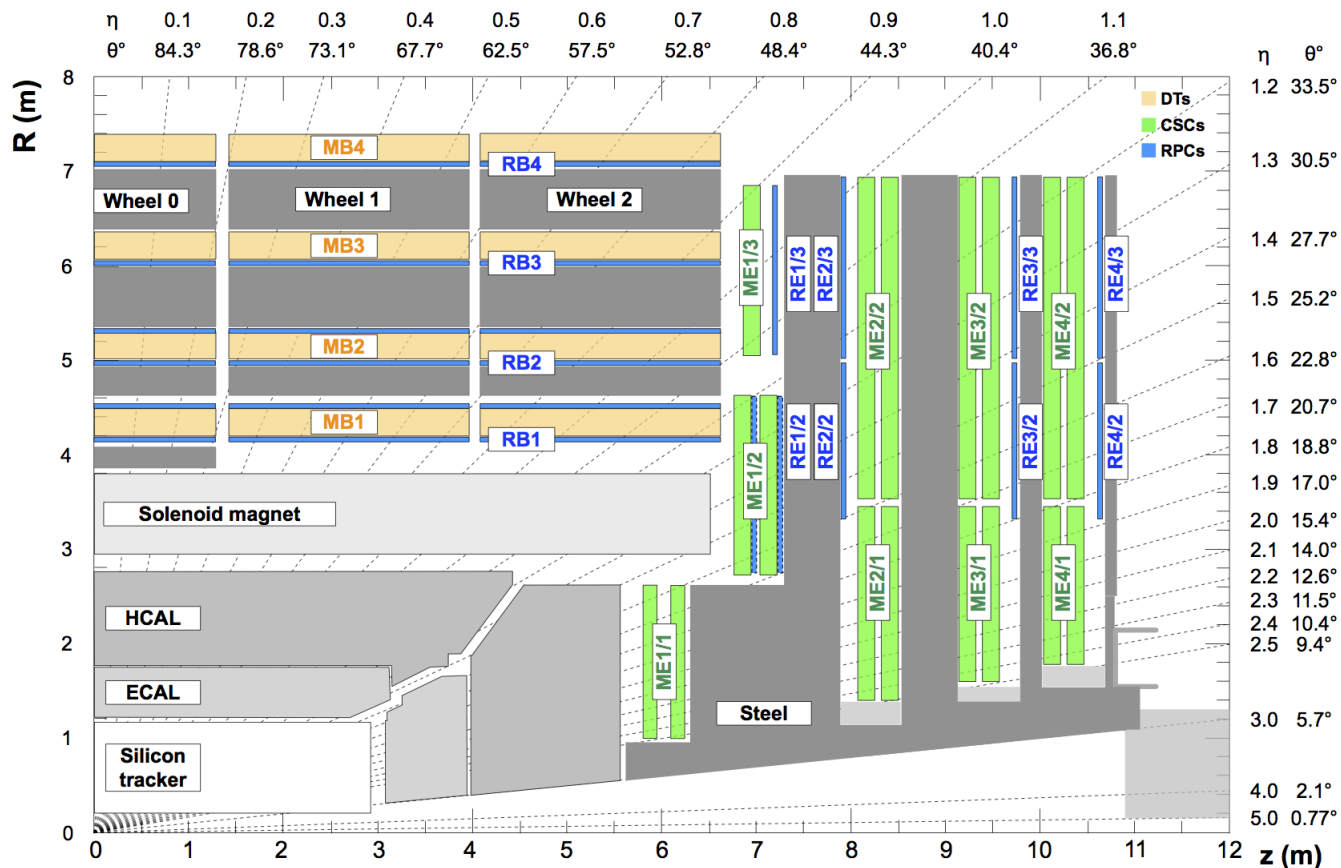
Figure 2.8: Illustration one quarter Muon System [42]

2.10 Trigger System

The LHC's bunch crossing rate exceeds 40 MHz[8][32] at full capacity, leading in around 10^9 pp collision/second at the interaction site. Because reading and storing all of the collision data is difficult, triggers are used to decrease the rate to a bearable level. These also serve as filters for potentially intriguing event fingerprints that might be employed in further physics research. The choice to read out the entire event data is made using a two-tiered system, with the first level (L1) consisting of specialised hardware triggers and the second level (HLT) consisting of a processing farm.

There are three sub-system in L1 Calorimeter Trigger ,Muon trigger and global Trigger.The L1 trigger pre-selects events of interest for the HLT to investigate further. The L1 trigger is in charge of detecting various leptons, E_T and quark jets. The HLT hardware consists of a processor farm with about 13000 CPUs that choose events using offline-quality reconstruction methods. Several processing stages, referred to as the HLT-path, are performed on the data in a predetermined order, rebuilding physical objects and making selections based on these objects. With each phase, the algorithms and refining of the reconstruction become more complex, therefore it's best to start with the data from the calorimeters and muon system before moving on to the more complex track reconstruction.
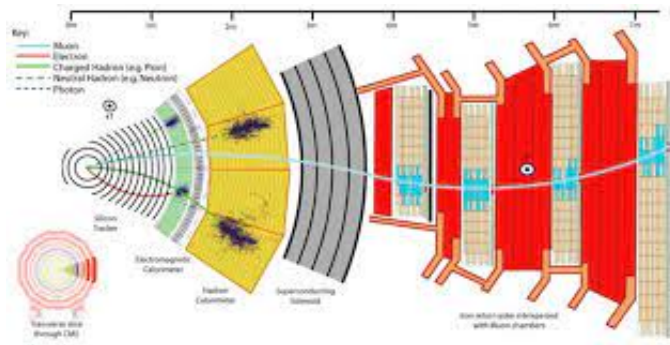
Figure 2.9: Recognition of pattern

Chapter 3

Proton Structure

The proton has a mass of 938.3 MeV [31]. Proton is the lightest and the most stable baryon. The life time of the proton is about 1.6×10^{34} years corresponding to the decay channel, $p \to e^+ + \pi^o$ and life time of 7.7×10^{33} for p $\to \mu^+ + \pi^o$. Proton is composed of three valance quarks (uud). Quantum number for proton is $I(J^P) = \frac{1}{2}(\frac{1}{2}^+)$, where I is the isospin, J is the total angular momentum and p is the parity. The mass of the up quark is $2.2 \pm^{+0.5}_{-0.3}$ and that of down quark is $4.7 \pm^{+0.5}_{-0.3}$. So if we sum up their masses, its is less than the mass of the proton so therefore the proton's structure must be more complex.

3.1   Deep Inelastic Scattering (DIS)

It is the process in which with the help of electron or muons the structure of hadrons is probed. Using the DIS structure of proton was studied, in fixed target experiment. The cross sections of Neutral current(NC) and Charged current(CC) processes were measured for a wide range of final states at HERA $e^{\pm}$ p-collider. In Fig. 3.1, Feynmen diagrams of NC and CC are presented. A set of variables can be used to characterise their kinematics. These variables include,
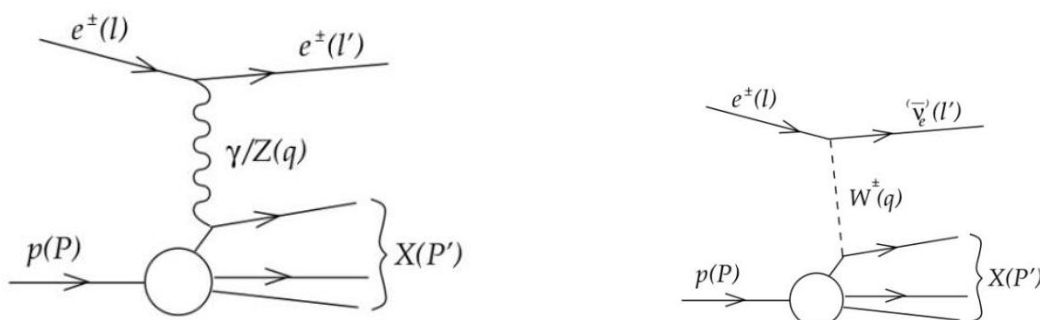
Figure 3.1: In $e^{\pm}$ p collisions, diagrams of NC (left) and CC (right) processes are shown

$$Q^2 = l - l' \qquad \text{Boson virtuality} \tag{3.1}$$

$$W^2 = (P + q)^2 \qquad V(\gamma/Z^o, W^{\pm})\text{-}p \text{ center of mass energy} \tag{3.2}$$

$$s = (l + P)^2 \qquad e^{\pm} p \text{ center of mass energy} \tag{3.3}$$

$$y = \frac{P.q}{P.l} \qquad \text{inelasticity} \tag{3.4}$$

$$x = \frac{Q^2}{2P.q} \qquad \text{Bjorken } x \tag{3.5}$$

While s is established by the experimental apparatus, the remaining variable must be calculated from out going particle observation. The virtuality Q^2 of the process reflects its resolution capabilities, with higher Q^2 indicating that the proton structure may be resolved to a greater extent. The momentum transmitted from the scattering lepton to the hadronic system in the proton rest frame is represented by the inelasticity y, and the proton momentum fraction participating in the reaction is represented by x.

In deep elastic scattering the differential cross-section can be represented by the equations,

$$\frac{d^2\sigma^{NC}}{dxdQ^2} = \frac{2\pi\alpha_{EM}^2}{Q^4 x}[Y_+ F_2^{NC}(x, Q^2) - y^2 F_L^{NC}(x, Q^2) \mp Y_- F_3^{NC}(x, Q^2)] \tag{3.6}$$

$$\frac{d^2\sigma^{CC}}{dxdQ^2} = \frac{G_F^2 M_W^4}{4x\pi(Q^2 + M_W^2)}[Y_+ F_2^{CC}(x, Q^2) - y^2 F_L^{CC}(x, Q^2) \mp Y_- F_3^{CC}(x, Q^2)] \tag{3.7}$$

These differential cross sections depend on the structural functions i.e F_L, F_2 and F_3 and these functions depend on the value of x and Q. In the Equations 3.6 and 3.7, α_{EM} is coupling constant of electromagnetic interaction, $Y_{\pm} = 1 \pm (1 - y)^2$ and G_F is Fermi constant given as,

$$G_F = \frac{\pi\alpha_{EM}}{\sqrt{2}sin^2\theta_W^2 m_W} \tag{3.8}$$

3.2 Parton Distribution Functions(PDF)

The quark parton model (QPM), which asserted that the proton is made up of charged, point like particles that do not interact with one other, was the prevalent hypothesis until QCD was completely established. In 1964 Gell–Mann and Zweig[35] suggested the concept of valence quark, independently explaining the different flavours of hadrons.

The structure function of proton R_2 in quark parton model is given by,

$$R_2 = \sum e_i^2[xq_i(x) + x\bar{q}(x)] \tag{3.9}$$

In Equation 3.9, e represents parton electric charge and 'i' in the subscript represents its flavour, q_i is the probability of parton to have x fraction of the momentum of the proton. In 1960, DIS experiment at SLAC[37] measured the structural function (R_2) and It was found that it was independent of the Bjorken scaling[10](x), for x

approximately to be $\frac{1}{3}$. Later, it was discovered that only around half (50% [25]) of the proton's entire momentum could be explained. As a result, another form of parton was required to explain the missing P_T, one that does not interact weakly or electromagnetically. At PETRA and DESY[13] collider, gluon was discovered whose properties were matching with the required parton. Furthermore, studies at the HERA and CERN SPS colliders have shown that the structure functions are Q^2 dependent (scaling violation), which is connected to the quark-gluon and gluon-gluon interactions, as well as proton's gluon content[40].

The probability of finding partons (quarks and gluons) in a hadron as a function of the fraction x of the proton's momentum carried by the parton is given by parton distribution functions. The PDF is the intrinsic property of hadrons and is process independent The momentum fraction carried by gluons increases as Q^2 increases. In the perturbative QCD domain, where the value of $\alpha_s(Q^2)$ is substantially lower than one, QCD predicts how parton distribution evolves with Q^2 energy scale, and these predictions are regulated by the QCD evolution equation DGLAP. Leading-Order (LO), i.e, first order in α_s (Q^2), Next-to-Leading-Order NLO, and Next-to-Next Leading-Order NNLO are distinct degrees of approximations for DGLAP equation, related to the power of $\alpha_s(Q^2)$ in the perturbative domain.

They can't be calculated from fundamental principles, instead, they must be computed using QCD fits to measured σ(cross section) using the factorization idea. The Collinear Factorization Theorem[12, 23] may be used to compute the cross section for a process in pp-collisions at a scale where α_s takes on small values.

$$\sigma_{pp \to X} = \sum_{a,b} \int_0^1 dx_a dx_b \int f_a^{h_1}(x_a, \mu_f) f_b^{h_2}(x_b, \mu_f) d\sigma_{xy \to z}(\mu_f, \mu_r) \tag{3.10}$$

$$\sigma_{pp \to X} = \sum_{a,b} \int_0^1 dx_a dx_b \int d\Phi_n f_a^{h_1}(x_a, \mu_f) f_b^{h_2}(x_b, \mu_f) \frac{1}{2\hat{s}} |Mxy \to z|^2 (\Phi, \mu_r, \mu_f)$$

$$\tag{3.11}$$

The fraction of momentum carried by the a and b parton is represent as x. whereas $f_{i/j}(x_{a,b}, \mu_f^2)$ refers to the PDFs of the partons involved in the production. The partonic cross section of the process $x + y \to$z is represented by $\sigma_{xy \to z}(\mu_f, \mu_r)$. The flux of the particles is given as $\frac{1}{2\hat{s}}$ which is equal to $\frac{1}{x_a x_b s}$ where s in the equation is CoM energy and integrated over the phase space of final state particles.

Factorization needs the formation of a new scale, the known as factorization scale μ_f, which is required to deal with infrared divergences that arise as a result of this method. When final state quarks release soft gluons or a high momentum gluon emits collinearly with a low momentum quark, infrared divergences occur. As a result, factorization may also be defined as the division of a collision's hard and soft regimes. The μ_f is often made equal to the μ_r, which is normally selected near the energy involved in the hard scattering process. This relates to the virtuality Q in Deep Inelastic Scattering experiments. It is commonly set to the mass of the heaviest particle or the transverse mass in the process that include the creation of heavy particles.

Fitting PDFs was done by a number of different organisations. The collaborations CTEQ[38], MSTW[36], ABKM[2] and NNPDF[6], some result of which are presented in Fig:3.2, incorporate all available data to fit their models. The PDF method and fitting are dependent on a number of assumptions and model uncertainties. There are a number of multipurpose event generators available, that cover
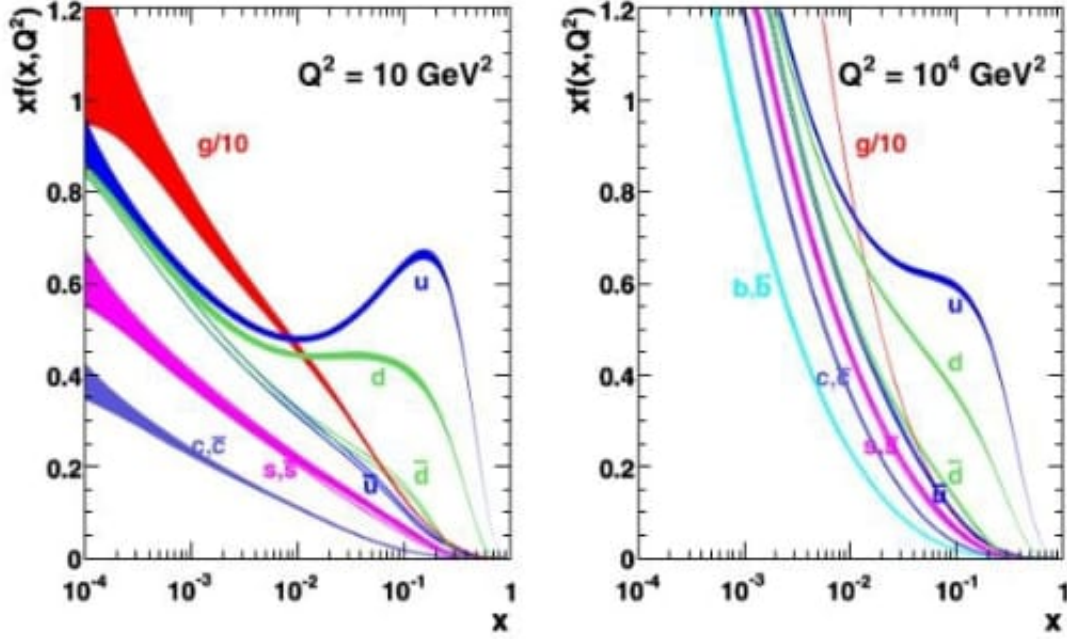
Figure 3.2: MSTW 2008 NLO PDFs at $Q^2 = 10 GeV^2$ and $Q^2 = 10^4 GeV^2$[36]

all theoretical features of proton-proton collisions. These event generators make use of various theoretical models, including the shower model for the initial MPI model and the final MPI model[11], final decay model and hadronisation.There are different event generator such as MADGRAPH[4],POWHEG[39], , HERWIG[24] , SHERPA[29] and PYTHIA[44] which cover all the aspects of new physics and standard model.

3.3 The Proton's Strange Quark Content

Among the light quarks, the s quark distribution has the least restricted Parton distribution function(PDF). PDF uncertainties, particularly the strange quark distribution, are still a significant source of experiment uncertainty like the determination of W boson mass at hadron colliders [34]. The charm creation analysis in CC(charged current) deep-inelastic (anti)neutrino- nuclei scattering contributed significantly to the results restricting the s-quark distribution. The CCFR[9], NuTeV[30] and NOMAD[41] collaborations estimated the cross section of oppositely charged dimuon generation in (anti-)neutrino-nucleon DIS studies. The muon with the higher transverse momentum is thought to come from neutrino scattering, whereas the oppositely charged muon is thought to be a charmed particle($D^*, D^{\pm}, \Lambda_c$) decay product. The CHORUS team also measured the cross section of inclusive charm creation from neutrino(v) and antineutrino($\bar{v}$) charged-current(CC) in nuclear emulsions. By measuring the flight duration and momentum of the hadrons and determining the charmed(C) particle production fractions, it was feasible to disentangle the contributions from distinct charmed particles in this experiment. CHORUS' cross sections are complimentary to the aforementioned tests since they are independent of the branching ratio B(c). Because the contribution of d-quarks to charm creation is Cabibbo suppressed, all v-scattering measurement have a sensitivity to strange quark composition of nucleon sea. The nuclear adjustments of the target must be

taken into account in PDFs produced from DIS experiments, which introduces new source of uncertainty. Using the ratio of charm decaying to two muons to complete CC production cross section, which is supplied by both NOMANDand CHORUS, the nuclear adjusmets in the derived PDFs are essentially cancelled out. To measure the strange quark composition of the proton, the data from all experiments conducted is employed in various QCD fits. The uncertainty in the s quark distribution derived is a factor of 2 smaller than for calculations utilising only the CCFR data due to the substantially higher statistics of the NOMAD observations. Using the ABM12 PDF set as a baseline, that already contains the CCFR and NuTeV data, the influence of the NOMAD as well as CHORUS results on the strange quark distribution was studied. The NOMAD as well as CHORUS datasets were separately as well as in combined form added to the fit, and it was discovered that merely utilising the NOMAD data pulls the strange quark distribution down, whereas including the CHORUS data seems to have the opposite result. Utilizing both datasets at the same time produces strange quark distribution which is in good agreement with the base of using only the CCFR and NuTeV data, as both datasets correct for the distribution's pulls. Only the ABMP16 PDF sets incorporate the most recent NOMAD data and hence represent the most exact strange quark distribution among the presently accessible PDF sets. The CCFR and NuTeV data are only included in the CT14nlo PDF collection, but the CHORUS measurements are included in the MMHT14nlo set. The CHORUS and NuTeV data, as well as the CMS collaboration's 7 TeV determination of W + c, are used in the NNPDF3.1nlo set. The strange quark distribution as well as strangeness suppression of the global PDF sets MMHT14nlo, ABMP16nlo, CT14nlo, and NNPDF3.1nlo at the scale of $m_W^2 = \mu_f^2$ are shown in Figure 3.3 and are in good agreement. Figure 3.3 also shows distributions as from ATLASepWZ16nnlo study, which do not coincide with the global PDFs, indicating an unsuppressed strange quark distribution.

The inclusive generation of electroweak bosons (Drell–Yan processes) at hadron colliders like Tevatron and the LHC imposes constraints for all sorts of light quarks and hence is indirectly sensitive to the strange quark distribution in the proton. Strange quark contributions to the total cross sections of Z^o and W are received via processes such as $\bar{u} + s \rightarrow W^-$, $s = \bar{s} \rightarrow Z^o$ and $u + \bar{s} \rightarrow W^+$. Figure 3.4 depicts the contributions of several quark-quark hard scattering mechanisms in Z^o and W creation in hadron collisions. In algorithms like DYNNLO or FEWZ, the differential cross sections of W and Z^o production may be computed with high accuracy, and theoretical predictions can be made with NNLO precision.

Early on, it was suggested that producing a W boson accompanied with a single charm quark(c) would be a good way to analyse distribution of strange quark(s) at hadron colliders. Because $W + c$ is dominated by the hard scattering of both a strange quark(s) and a gluon at leading order $s + g \rightarrow W^+ + \bar{c}$ and $\bar{s} + g \rightarrow W^- + c$, this process investigates the proton's strange quark content. Figure 3.5 shows the two Feynman diagrams contribute to the cross section at leading order Contributions from the down(d) quarks are predicted as well, but at a considerably lower rate than in v-scattering studies. In all diagrams in this section we can also swap strange quark with down(d)-quark, and a small asymmetry between the $W^- + c$ and $W^+ + \bar{c}$ cross sections is predicted owing to the existence of a down(d)-valence quark with in the proton.
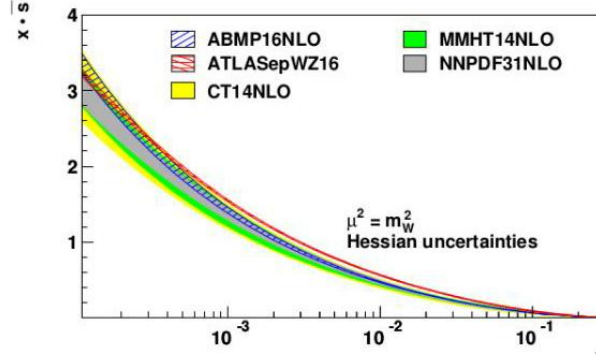
(a) Distribution of strange quark
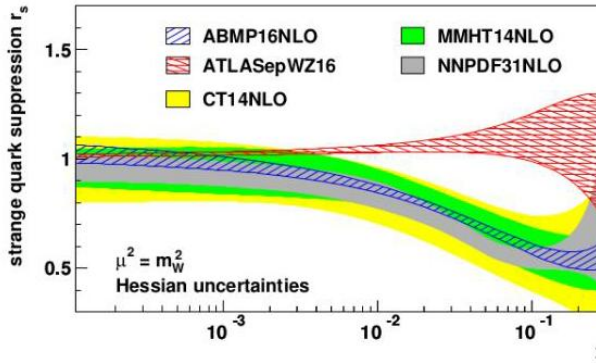
(b) Strange suppression

Figure 3.3: The strange quarks distribution and strangeness suppression as a function of x for different PDF sets produced at the scale $m_W^2 = \mu_f^2$.

3.4   Theoretical Predictions

3.4.1   Matrix Element Calculations

The factorization theorem is used to calculate the parton level σ of a process of concern (W vector boson and Charm quark), which requires calculating the matrix components $M_{ab \to n}$ contributing at defined orders of pQCD. The PDF set utilised in the simulation define the chance of two partons colliding and their momentum in the initial hard scattering. At this moment, the computation of LO(Leading Order) matrix components is highly automated, and it has been incorporated in a number of event generators, such as MADGRAPH[4].

Next to Leading Order(NLO) or even Next to next leading order (NNLO) generators are favoured due to the enormous scale dependency of LO calculations, albeit the divergences coming from real and virtual corrections make calculations beyond Leading order exceedingly difficult. The so-called phase space slicing method [28] [27] and the infrared(IR) subtraction method are the two basic ways devised to deal with this issue, with the latter being the favoured tool in many current event generators.

MADGRAPH5_aMC@NLO [3] is one of the NLO event generators that can compute tree level and one loop amplitudes for arbitrary processes with LO and NLO precision using the FKS subtraction approach.
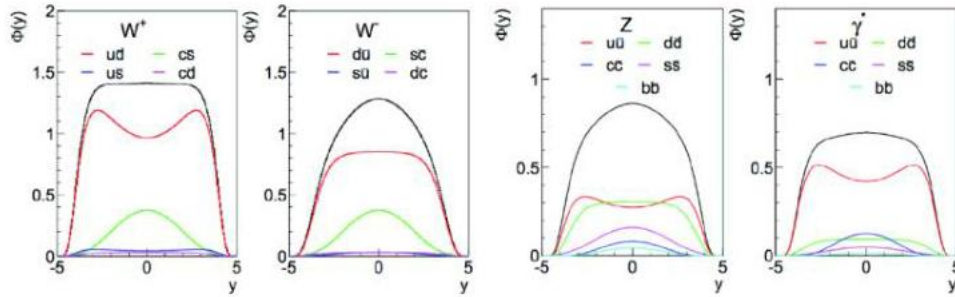
Figure 3.4: Leading order $q - q$ processes contributing to $W^{\pm}$(lines of different colour)and Z^o/γ(nlack line) cross-section as a function of rapadity of boson
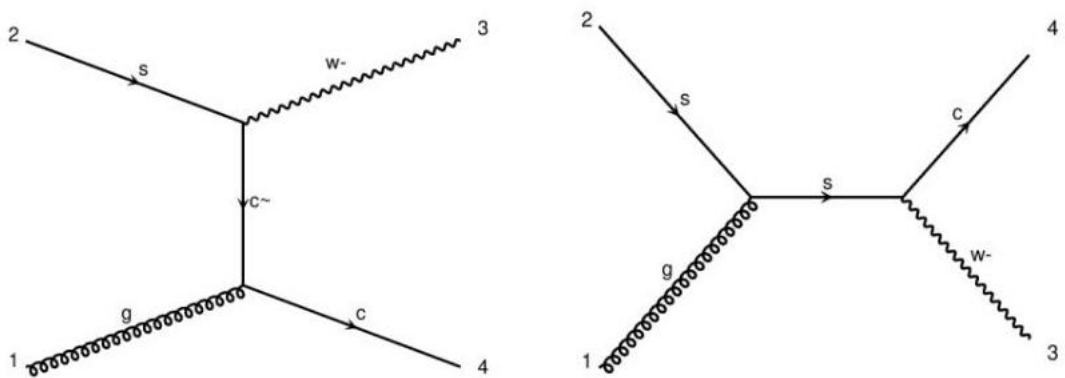
Figure 3.5: $W + c$ production Feynman diagrams at the LHC at Leading order(LO) in pQCD.These diagrams are drawn by Madgraph5.

Furthermore, higher degree adjustments of a particular process can be included in the produced events in the form of extra actual emissions being taken into account in the computations. POWHEG is another popular NLO event generator that uses the FKS subtraction formalism to calculate heavy flavour creations in hadron collisions with NLO precision. Both generators are commonly used as the initial point for complete event simulations since they may be linked to other programmes for parton shower and hadronization, and they provide appropriate matching and merging processes in such circumstances.

3.4.2 Parton Shower

Radiative corrections to LO(Leading Order) or NLO(Next to Leading Order) computations are frequently approximated using a parton shower approach as higher levels of matrix element calculations become increasingly complex and computationally demanding. Additional radiations of types $q \rightarrow q\gamma$, $q \rightarrow qg$, $g \rightarrow q\bar{q}$,$g \rightarrow g\bar{g}$ and $\gamma \rightarrow l\bar{l}$, $l \rightarrow \gamma$, are simulated there by calculating the chance of an emission occurring between two evolution scales μ_1 and μ_2, with $\mu_2 ¡ \mu_1$. The development of a parton shower is regarded global, and is therefore unaffected by the showered partons' creation process ($e^{\pm}p$, e^+e^- etc.).

In PYTHIA [43] and HERWIG [5], two frequently used parton showers (PS) are provided, and they may be linked up with other generators such as POWHEG or MADGRAPH for the initial matrix element computations. PYTHIA employs a P_T-ordered (PS), with the evolution scale matching to the radiated parton's P_T μ = p_T, whereas HERWIG employs an angular ordered scheme with $\mu \approx \Theta^2 E^2$. In the latter example, E stands for the radiated parton's energy and Θ is the angle between the two partons.

3.4.3 Merging and Matching in MC

It is not possible to combine Matrix Element (ME) calculations with a parton shower by using a PS algorithm on the final state partons of Matrix Element calculations separately. This results in double counting of contributions, which involves additional hard scattering emissions. A ME calculation with $n+1$ partons with in final state, and also a calculation with n final state partons, where hard radiation comes from the parton shower, can produce these. When ME computations and PS are utilised independently, Figure 3.6 depicts probable circumstances that lead to duplicate counting. Due to the radiative adjustments already incorporated in NLO calculations, these concerns are overcome by using matching or merging processes, however the methodologies need distinct approaches for Leading Order(LO) and Next to Leading Order(NLO) calculations.

3.5 Even Selection of W and Charm Quark

The leptonic decay of $W^{\pm}$ bosons into a muon and a neutrino ($W^{\pm} \rightarrow \mu\bar{v}_\mu$) and a charm quark(C) hadronizing to a $D^*(2010^{\pm})$ meson are used to explore the associated production of $W + c$. The charm quark is is confirmed by reconstructing $D^*(2010)^{\pm}$ meson in lowest energy state having a mass of 2010.26 MeV. This charmed meson has a decay width of $\Gamma = 83.4\pm1.8$ keV. The quark content of $\bar{c}d$ for
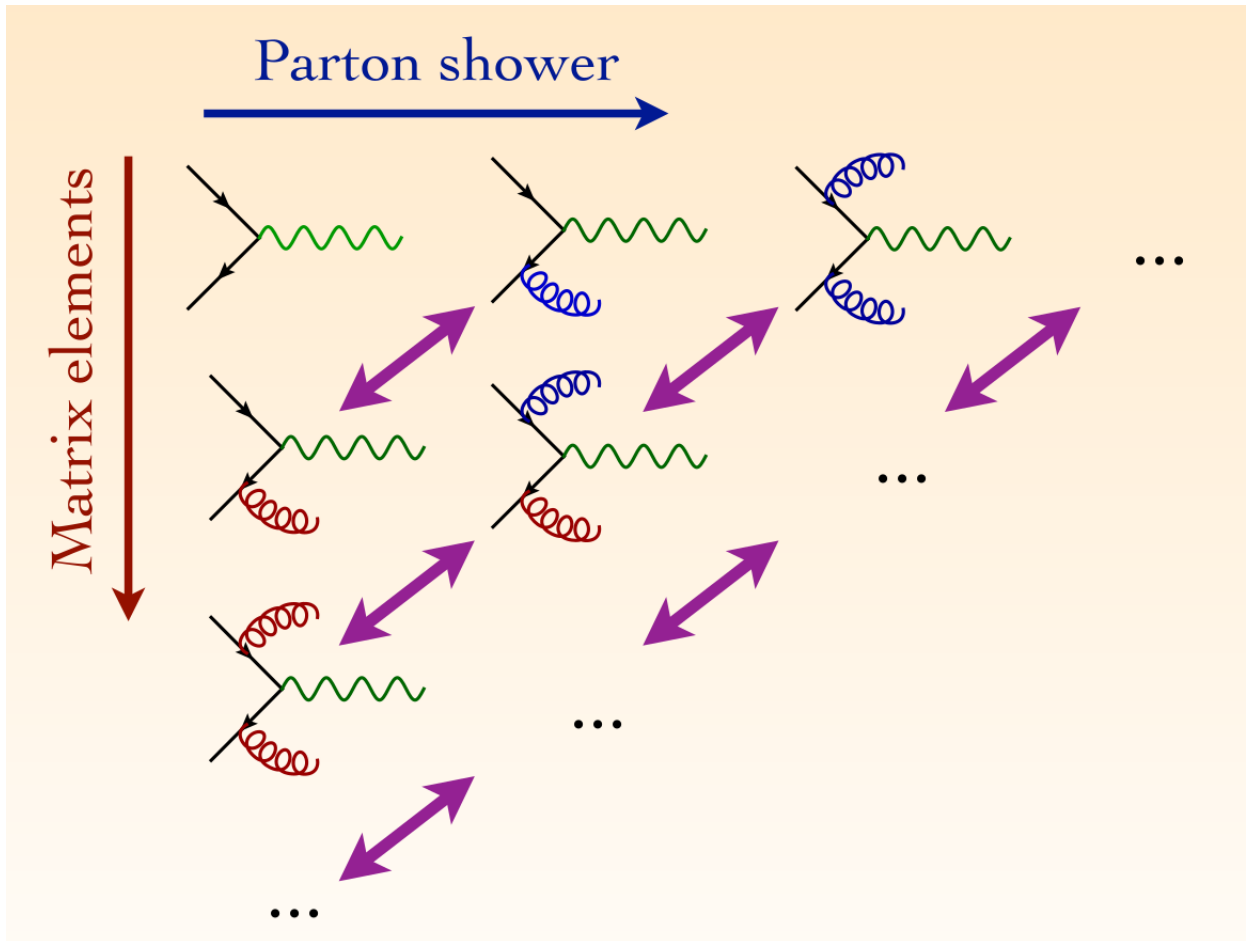
Figure 3.6: In the combined use of ME calculations and PS algorithms, there is double counting.Red are the contribution from ME and the blue show the contribution from PS.

a $D^*(2010)^+$ and $\bar{d}c$ for a $D^*(2010)^-$. $D^*(2010)^{\pm}$ is spin one meson. It decay into charged pion and $D^o(D^*(2010)^{\pm} \rightarrow D^o\pi^{\pm})$ with do decaying to opposite charged pion and kaon, which is the cleanest signature of the event.

3.5.1 Selection of W Boson

The existence of a high p_T isolated muon and p_T^{miss}(missing transverse momentum), suggesting the presence of a neutrino, is used to identify events including a $W^{\pm}$ boson decay. The Muon candidates must have p_T greater than 26 GeV. A separation requirement is also imposed to prevent contamination from muons included in jets.

$$I = [\sum^{CH} p_T + max(0.1, \sum^{NH} p_T + sum^{EM} p_T - sum^{PU} p_T)]/p_T^{\mu} \leq 0.15 \qquad (3.12)$$

Inside a cone of radius $R \leq 0.4$, it traverses the p_T sum of particle-flow (PF) candidates for neutral hadrons (NH), charged hadrons (CH) and photons (EM), and charged particles from pileup (PU). In order to inhibit background from Drell–Yan processes, events where more than one muon candidate meets all of the following requirements are eliminated. A condition on the M_T(transverse mass), which is given as product of p_T^{μ} and p_T^{miss}, ensures the availability of a neutrino for an event.

$$M_T \equiv \sqrt{2p_T^{\mu}.p_T^{miss}(1 - cos(\phi_{\mu} - \phi_{p_T^{miss}}))} \qquad (3.13)$$

The $M_T > 50 GeV$ is necessary in this study, resulting in a considerable suppression of muons via hadron decays.

3.6 Measurement of the $W + $ charm Cross Section

The requirements of the muon's transverse momentum(p_T) and pseudorapidity, as well as the p_T of charm quark, determine the kinematic domain of the fiducial W and charm quark measurement. It correspond to $|\eta| < 2.4$, $p_T^{\mu} > 26 GeV$ and $p_T^C > 5 GeV$

$W + c$ production's fiducial cross section is calculated as follows:

$$\sigma(W + c) = \frac{N_{sel}S}{L_{int}B(c \rightarrow D^*; D^* \rightarrow \pi_{slow}^{\pm}; D^o \rightarrow K^{\pm}\pi^{\pm})C} \qquad (3.14)$$

N_{sel} is the number of events selected after subtraction of SS(same sign) from OS(opposite sign)(OS-SS). S is the signal ratio. L_{int} denotes the integrated luminosity. B is the branching ratio and the correction factor C is accouted for the efficiency and acceptance of the detector. The measurement of cross section of $W + $ charm is determined inclusively.

3.6.1 Systematic Uncertainties

It is possible to investigate the impact of systematic uncertainties on measured cross sections, by changing the efficiency and assumptions in each of their respective uncertainties.

The resultant change in the cross section relative to the central value are consider as a contributor to the measurement's systematic uncertainty. The total uncertainty accounts for the largest shift in either direction.

PDF set	$p_T^\ell > 25\,\text{GeV}$		$p_T^\ell > 35\,\text{GeV}$	
	$\sigma(W+c)$ [pb]	$\Delta_{\text{PDF}}[\%]$	$\sigma(W+c)$ [pb]	$\Delta_{\text{PDF}}[\%]$
MSTW08	100.7	$^{+1.8}_{-2.2}$	78.7	$^{+1.8}_{-2.2}$
CT10	109.9	$^{+7.0}_{-5.8}$	87.3	$^{+7.1}_{-5.9}$
NNPDF2.3	99.4	± 4.2	78.9	± 4.2
NNPDF2.3$_{\text{coll}}$	129.9	± 11.6	102.7	± 11.5
CMS	107.7 ± 3.3 (stat.) ± 6.9 (syst.)		84.1 ± 2.0 (stat.) ± 4.9 (syst.)	

Figure 3.7: Prediction for cross section of W+charm from MCFM at NLO. Theoretical predictions for two distinct thresholds in the lepton p_T are obtained using MCFM. The last row show the experimental results.

3.7 Measured Cross section of W and charm quark at different CoM energy

The production cross section of W and charm quark is measured at LHC in CMS at different CoM energies, i.e 7 TeV, 8 TeV and 13 TeV with different uncertainties ($\pm stat, \pm syst. \pm lumi$).With an increase in center-of-mass energy, the measured value of cross section increases. The comparison between predicted and measured cross section can be seen in Tables 3.1 3.2 3.3and Fig. 3.9 3.10 3.8 3.11 3.7
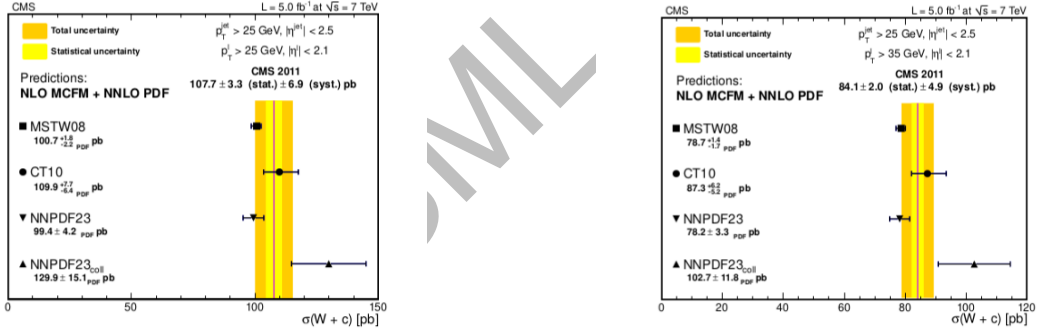
Figure 3.8: Comparison of the average of the experimental data with the theoretical predictions for $(W + c)$ calculated with MCFM using other sets of PDFs.

The associated production of a W^+ boson with a $\bar{c}$ and a W^- boson with a c quark is measured in terms of cross section ratios at 7 TeV as,

$$\frac{\sigma(pp \to W^+ + \bar{c} + X)}{\sigma(pp \to W^- + c + X)}(p_t^\mu > 25 GeV) = 0.954 \pm 0.025(stat.) \pm 0.004(syst.).$$

$$\frac{\sigma(pp \to W^+ + \bar{c} + X)}{\sigma(pp \to W^- + c + X)}(p_t^\mu > 35 GeV) = 0.938 \pm 0.019(stat.) \pm 0.006(syst.).$$
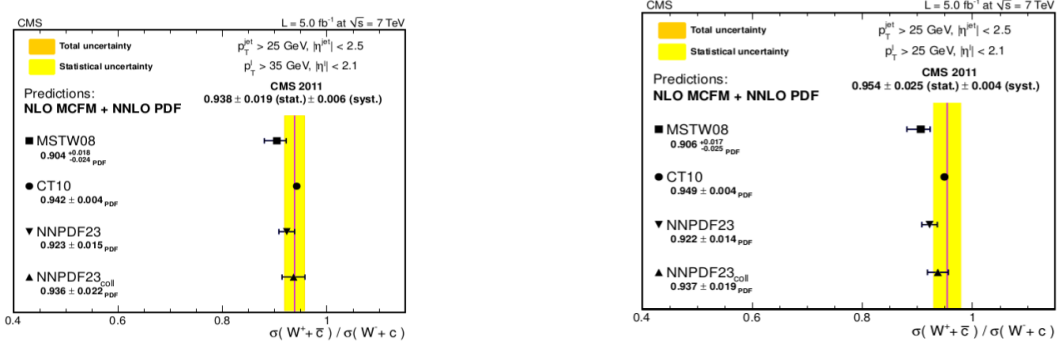
Figure 3.9: Comparison of the average of the experimental data with the theoretical predictions for $(\frac{W^++\bar{c}}{W^-+c})$ calculated with MCFM and other sets of PDFs. The predictions for a transverse momentum threshold of the lepton, $p_T^l > 25$ GeV for W-boson decay are shown in the right plot and the left plot presents the predictions for $p_T^l > 35$ GeV. The uncertainity associated with the scale variation is $\pm 1\%$
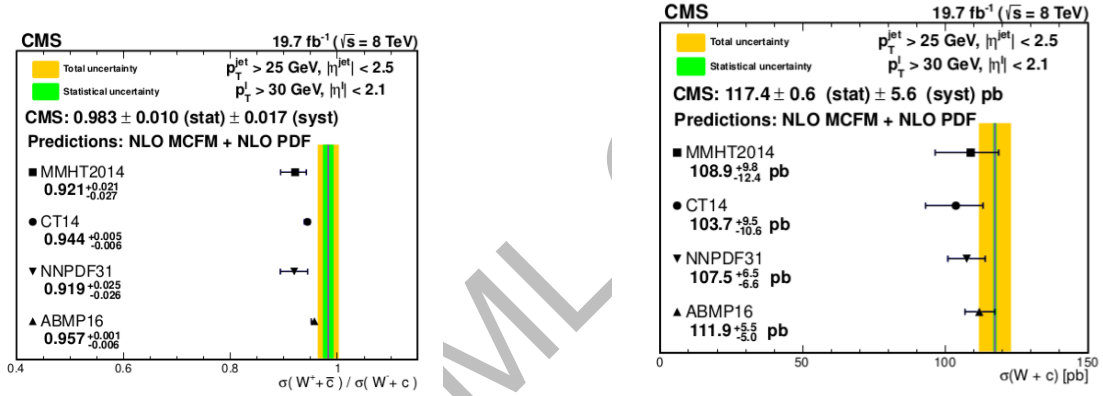
Figure 3.10: Comparison of the theoritical prediction for $\sigma(W + c)$(left) and $\frac{\sigma(W^++\bar{c})}{\sigma(W^-+c)}$(right) calculated with MCFM using different PDFs with the experimental measurement at 8 TeV

3.8 Methods of Error Estimation

A major source of uncertainity in the prediction of the cross section is incomplete understanding of the proton PDFs. The PDF uncertainties may be calculated by subtracting the difference between the central PDF and the Eigenvectors or error vectors of the corresponding PDF set from the sum in quadrature. The uncertainty determination is dependent on the provided PDF set; for example, uncertainties for the Monte Carlo set (NNPDF) differ from those for the Hessian PDF set, but are the same for all other sets.

3.8.0.1 Hessian Uncertainities

The mean and error sets are provided for Hessian PDF sets. The number of free parameters is equal to the number of eigenvectors. As a result, the error-vectors in PDFs are doubled. Each error set corresponds to shifting each independent orthonormal Hessian eigenvector in the positive or negative direction by the stated

PDF set	$\sigma(W+c)[pb]$	$\delta_{PDF}[\%]$	$\delta_{scales}[\%]$	$\delta_{\alpha_s}[\%]$	Total uncert.[pb]
MMHT2014	108.9	$^{6.0}_{-9.1}$	$^{4.4}_{-4.6}$	±5	$^{+9.8}_{-12.4}$
CT14	103.7	$^{7.6}_{-8.7}$	$^{4.5}_{-4.6}$	±2.2	$^{+9.5}_{-10.6}$
NNPDF3.1	107.5	±3.5	$^{4.4}_{-4.5}$	±2.2	$^{+6.5}_{-6.6}$
ABMP16	111.9	±0.9	$^{4.8}_{-4.4}$	-	$^{+5.5}_{-5.6}$
CMS		$117.4\pm0.6(\text{stat.})\pm5.4(\text{syst.})[pb]$			

Table 3.1: Theoretical predictions from MCFM at NLO for $\sigma(W+c)$. The central result of the prediction is given for each PDF set, together with the relative uncertainty as determined by the PDF set, as well as the uncertainties associated with scale variations and the value of α_s. At 8TeV.

PDF set	$R_c^{\pm}$	$\delta_{PDF}[\%]$	$\delta_{scales}[\%]$	$\delta_{\alpha_s}[\%]$	Total uncert.[pb]
MMHT2014	0.921	$^{+2.20}_{-2.8}$	$^{0.3}_{-0.2}$	±0	$^{+0.021}_{-0.027}$
CT14	0.944	$^{+0.4}_{-0.6}$	$^{+0.4}_{-0.2}$	±0.1	$^{+0.005}_{-0.006}$
NNPDF3.1	0.9195	±2.6	$^{0.1}_{-0.6}$	±0.8	$^{+0.025}_{-0.026}$
ABMP16	0.957	±0.1	$^{+0.0}_{-0.7}$	-	$^{+0.001}_{-0.00}$
CMS		$0.983\pm0.010(\text{stat.})\pm0.016(\text{syst.})[pb]$			

Table 3.2: Theoretical predictions from MCFM at NLO for $R_c^{\pm}$. The central result of the prediction is given for each PDF set, together with the relative uncertainty as determined by the PDF set, as well as the uncertainties associated with scale variations and the value of α_s. At 8TeV. The last row shows the experimental result.

confidence level (one sigma or 90% C.L). Consider a variable V with central value equal to V_o. Whereas V_i^+ and V_i^- is there corresponding variations in error vector, in negative and positive direction.

$$\Delta\mathbf{V}^-_{max} = \sqrt{\Sigma_{i=1}^N[max(V_o - V_i^+, V_o - V_i^-), 0]^2} \tag{3.15}$$

$$\Delta\mathbf{V}^+_{max} = \sqrt{\Sigma_{i=1}^N[max(V_i^+ - V_o, V_i^- - V_o), 0]^2} \tag{3.16}$$

The contributions of PDF error that lead to a rise in the observable V are added in quadrature given by $\Delta\mathbf{V}^+$, and the PDF error contributions that lead to a drop in the observable V are added in quadrature to give $\Delta\mathbf{V}^-$. The orthonormal basis of the eigenvectors justifies the addition in quadrature. The sum is taken over all the error eigen vectors(N). For symmetric cases, the PDFs uncertainties are calculated as,

$$\Delta\mathbf{V} = \frac{1}{2}\sqrt{\Sigma_{i=1}^N[V_i^+ - V_i^-]^2} \tag{3.17}$$

In most of the cases the symmetric and asymmetric uncertainties calculation gives the same value. The cases in which these values do not agree show how much χ^2(log like hood function) distribution deviates from the quadratic form.

3.8.0.2 Uncertainty Estimation by MC Replica Method

A Parton Distribution function(PDFs) set with replicas is provided for the NNPDF Monte Carlo set. The mean value for any observable Y (for example, cross section)

PDF set	$\sigma(W+c)[pb]$	$\Delta_{PDF}[\%]$	$\Delta_{\mu}[\%]$	$\sigma(W^{+}+\bar{c})/\sigma(W^{-}+c)$
MMHT14nlo	1057.1	$^{+6.50}_{-8.0}$	$^{+3.2}_{-2.2}$	$.960^{+0.023}_{-0.033}$
CT14nlo	992	$^{+7.2}_{-8.4}$	$^{+3.1}_{-2.1}$	$.970^{+0.005}_{-0.007}$
NNPDF3.1nlo	1030.2	± 5.3	$^{3.2}_{-2.2}$	$0.965^{+0.043}_{-0.043}$
ABMP16nlo	1077.9	± 2.1	$^{+3.4}_{-2.4}$	$0.975^{+0.001}_{-0.00}$
NNPDF3.0nlo	959.5	± 5.4	$^{2.8}_{-1.9}$	$0.962^{+0.034}_{-0.034}$
ATLASepWZ16nnlo	1235.1	$^{+1.4}_{-1.6}$	$^{3.7}_{-2.8}$	$0.976^{+0.001}_{-0.001}$

Table 3.3: With MCFM, the NLO predictions for $\sigma(W+c)$ were obtained. The uncertainties account for scale variations and PDF. At 13 TeV
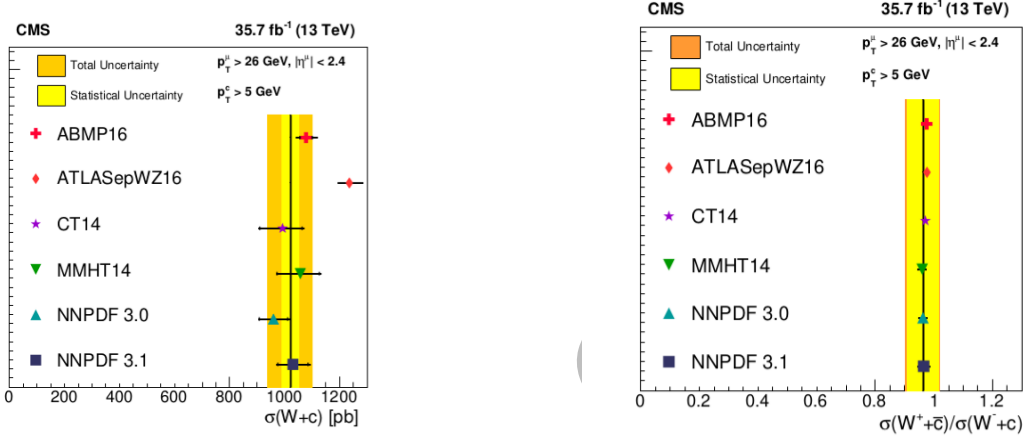
Figure 3.11: At 13 TeV, the cross section ratio $(W^{+}+c)/W^{-}+c$ and the inclusive fiducial cross section $\sigma(W+c)$

that is dependent on PDF sets is calculated using standard relation.

$$< Y(q) >= \frac{1}{N_{rep}} Y^{N_{rep}}_{i=1} Y(q^{i}) \tag{3.18}$$

where N is the Monte Carlo(MC) PDF set's number of replicas According to the standard relation, the related uncertainty in the observable is determined using,

$$\sigma_{Y} = [\frac{N_{rep}}{N_{rep}-1} < Y(q)^{2} > - < Y(q) >^{2}]^{\frac{1}{2}} \tag{3.19}$$

$$\sigma_{Y} = [\frac{N_{rep}}{N_{rep}-1} \Sigma^{N_{rep}}_{i=1} (Y(q^{i}) - < Y(q) >)^{2}]^{\frac{1}{2}} \tag{3.20}$$

3.8.1 Theoretical Uncertainties

The relationship between PDF and measurable quantities is improved when theoretical uncertainties are determined. Experimental uncertainty estimation is much more complicated than theoretical uncertainty determination, with just a few uncertainties to be studied in detail.

First source of theoretical uncertainty is the determination of strong interaction between quarks. The value of α_{s}, the heavy quark weights m_{c} (charmquarks) and m_{b} (bottomquarks), and the variation of the factorisation μ_{F} and renormalisation

μ_R scales are sources of theoretical uncertainty in quantum chromodynamics(QCD). Each PDF group explores the uncertainty caused by the choice of the α_s value in depth. Some PDF groups, like NNPDF3.1, Cteq14, and HERA, have looked at the uncertainty caused by the choice of heavy quark weights (charm and bottom). NNPDF3.1 investigates the uncertainties caused by differences in μ_F and μ_R scales.

3.8.1.1 Uncertainty in the value of α_s

As a result, we turn to any theoretical uncertainty that has been thoroughly investigated thus far, namely the uncertainty on α_S. Because α_s is significantly connected with PDFs, particularly the gluon distribution, the value chosen for α_s is important. As seen in Fig.3.12, various PDF groups used varied values of α_s. Fitting PDFs is
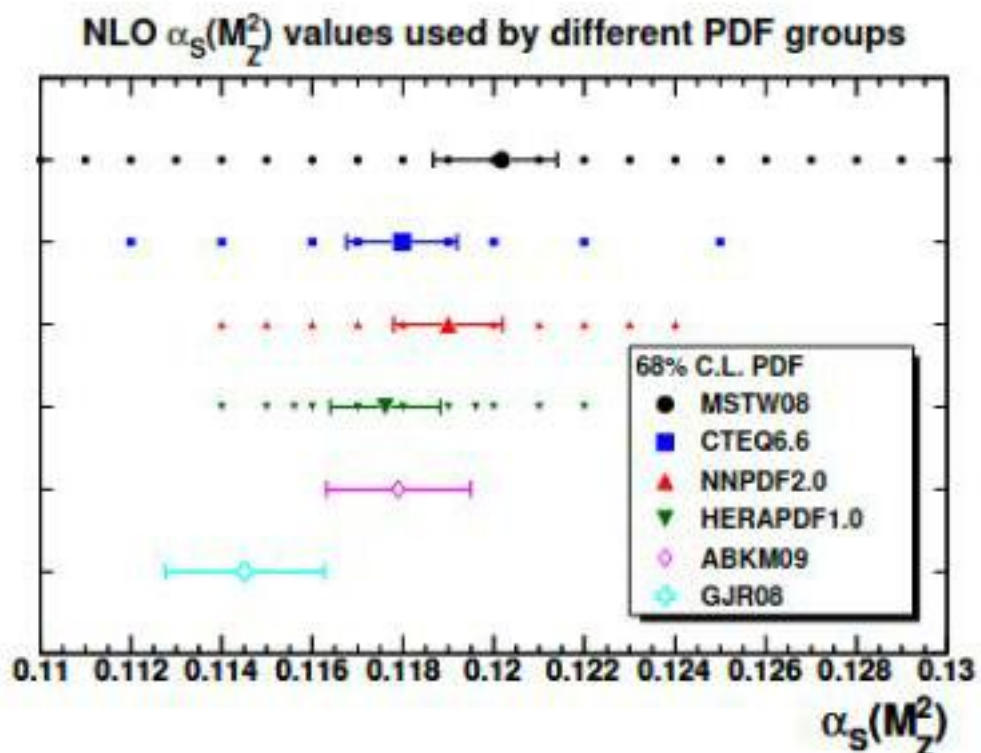
Figure 3.12: Fits for which α_S values are available. Each group's default values and uncertainties are also displayed. G. Watt's plot[45]

done for a variety of α_s values. Despite the fact that a PDF set corresponding to some reference α_s value is provided, the user is free to select any of the provided sets. HERAPDF(0.1176), CTEQ(0.118), NNPDF0.119), and MSTW(0.120) have used this approach.

3.8.1.2 PDF+ α_s uncertainties

Even if PDF uncertainty and $\alpha_s m_Z^2$ uncertainty are associated, the total one-σ combined PDF+α_s uncertainty including in this correlation can be found simply without approximation by computing the one-σ PDF uncertainty with α_s fixed at its central value and the one-σ α_s uncertainty with the PDFs fixed at their central

value, and adding the results.

$$\Delta\sigma = \sqrt{\Delta\sigma_{pdf}^2 + \Delta\sigma_{\alpha_s}^2} \tag{3.21}$$

Different types of approaches are used by different groups for the calculation of PDF+α_s uncertainty.

3.8.1.2.1 CTEQ Combined PDF and α_s uncertainties The uncertainty associated with α_s can be evaluated by computing any given observable with $\alpha_{m_Z^o}$ $= 0.118\ \delta^{(68)}$ in the partonic cross-section and with the PDF sets which have been extracted with these values of α_s. CTEQ takes $\alpha_s = 0.118\pm\delta^{(68)}$ as an external input parameter as well as provides the CTEQ6.6alphas (or the CT10alpha) series, which contains four sets extracted using $\alpha = 0.120, 0.119, 0.117, 0.116$.

$$\Delta_-^{\alpha_s} = F(\alpha_s^o - \delta^{(68))}\alpha_s) - F(\alpha_s^o) \tag{3.22}$$

$$\Delta_+^{\alpha_s} = F(\alpha_s^o + \delta^{(68))}\alpha_s) - F(\alpha_s^o)$$

CTEQ showed no significant deviations from quadratic approximation in the investigations in Ref., therefore the technique presented below will be correct for the cross sections studied here. So the combined PDF+α uncertainty for the CTEQ is given by,

$$\Delta_-^{PDF+\alpha_s} = \sqrt{(\Delta_-^{\alpha_s})^2 + ((\Delta F_{PDF}^{\alpha_s^o})_-)^2} \tag{3.23}$$

$$\Delta_+^{PDF+\alpha_s} = \sqrt{(\Delta_+^{\alpha_s})^2 + ((\Delta F_{PDF}^{\alpha_s^o})_+)^2}$$

where Δ^{α_s} is a α_s uncertainity in cross section $\Delta F_{PDF}^{\alpha_s^o})$ is PDF uncertainity and $Delta_-^{PDF+\alpha_s}$ is combined PDF+α_s uncertainity.

Chapter 4

Results and Discussions

4.1   Work summary

The measurement of the inclusive and differential production cross section of the W boson and charm(c) quark are compared to theoretical predictions calculated with MADGRAPH at NLO(Next to Leading Order). The mass of charm(c) is set to $m_c =$1.5 GeV. The strong coupling constant $\alpha_s(M_Z)$ is set to the value used in the evaluation of the particular Parton Distribution Function and the factorization and renormalization scales are set to $\mu_F=\mu_R =m_Z$. The PDF uncertainties are calculated using each PDF group's prescriptions, which include α_s variations. The predicted values of inclusive cross sections at different CoM energies and the PDF are caluated. These are evaluated by changing μ_F and μ_R by a factor of 2 (up and down) at the same time.

4.2   HERAPDF20 and NNPDF31 Parton Distribution Functions

A detailed understanding of PDFs was significant for the discovery of Higgs boson at the LHC, and it also gives useful insight into the search for new physics at the LHC. The HERAPDF20 is released at LO(Leading Order), NLO(Next to Leading Order) and NNLO(Next to Next Leading Order) accuracy.

Parton Distribution Functions at different values of $\mu_F = Q^2$ for LO and NLO are plotted in the following plots of Fig 4.1 and 4.2.
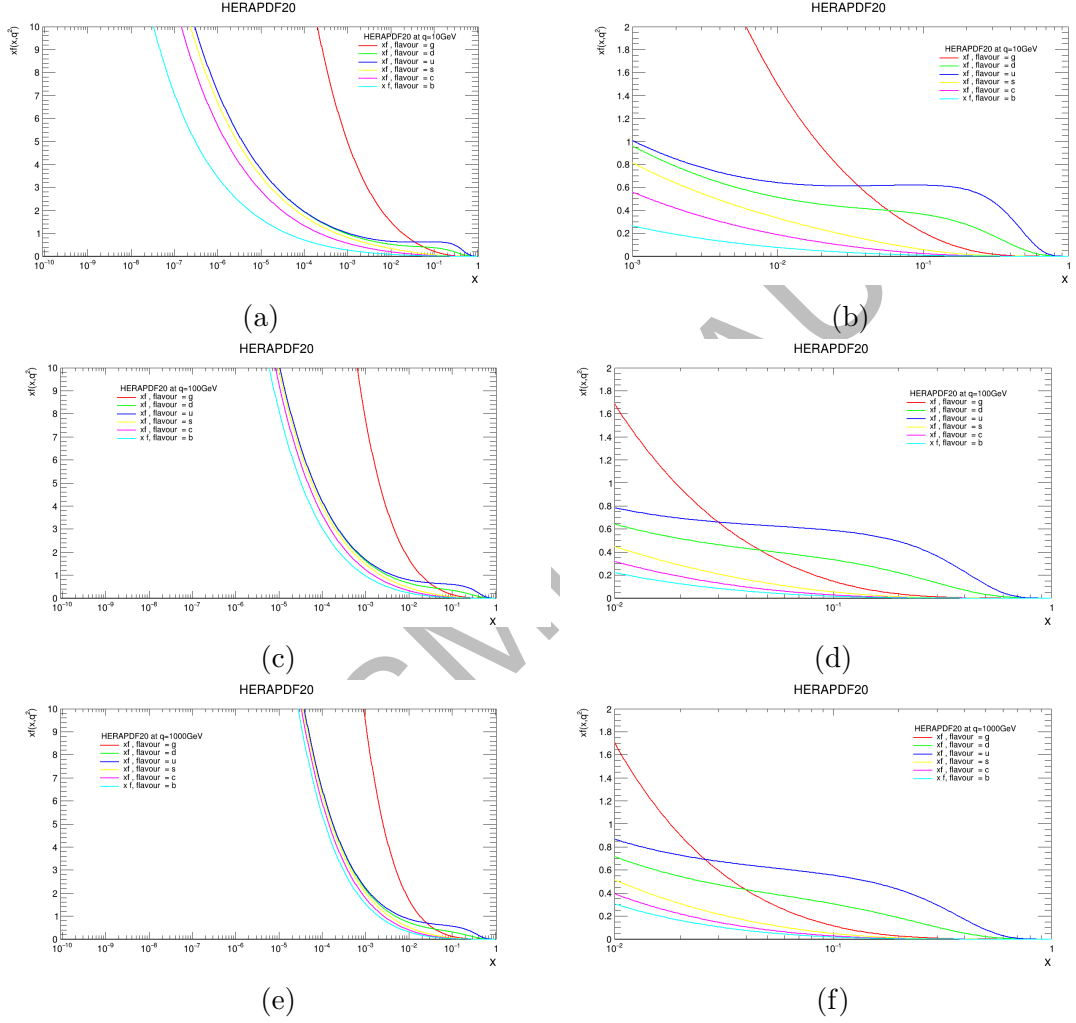
Figure 4.1: The HERAPDF20-LO PDFs for down(d), up(u), strange(s), charm(c), bottom(b) quarks and gluon(g). (a) and (b) at $Q^2 = 10$ GeV, (c) and (d) at $Q^2 = 100$ GeV and (e) and (f) at $Q^2 = 1000$ GeV.
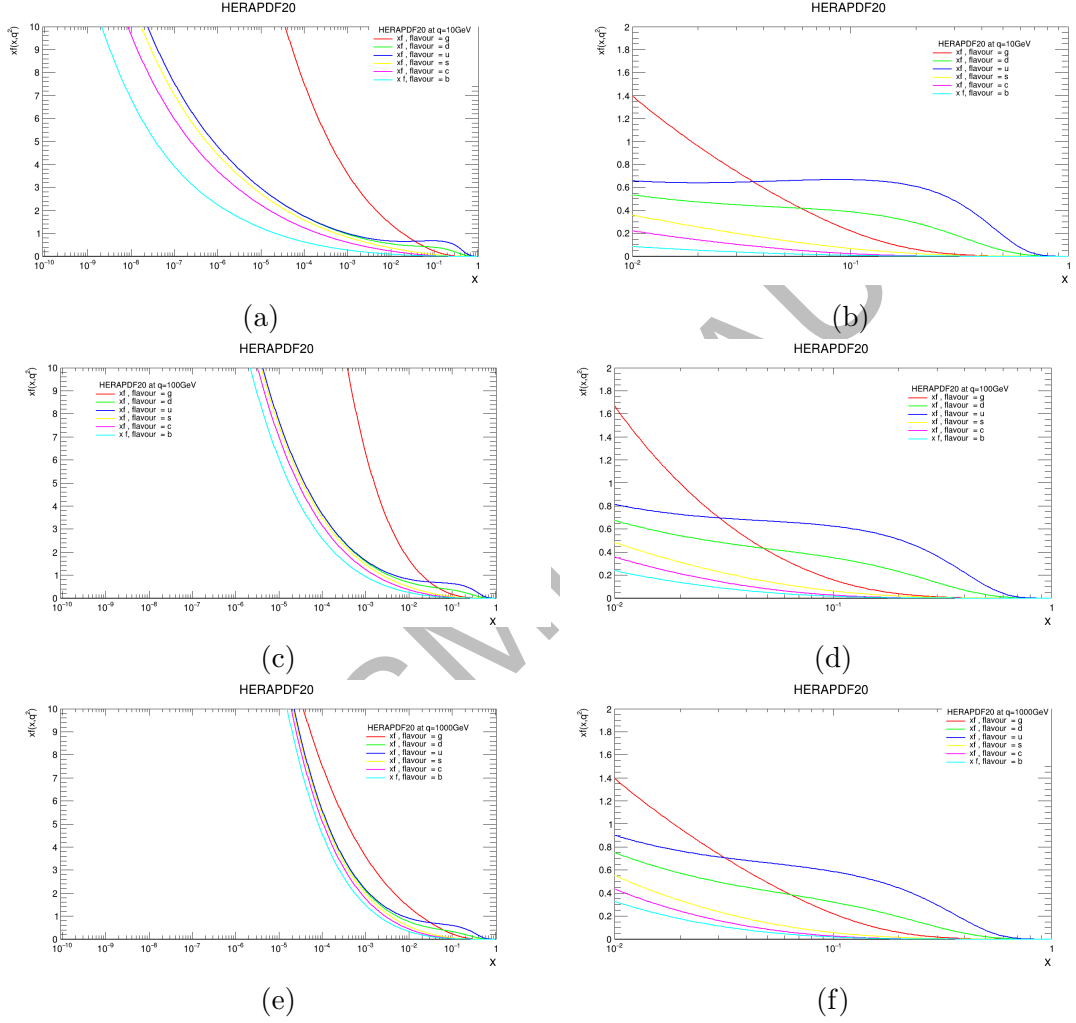
Figure 4.2: The HERAPDF20-NLO PDFs for down(d), up(u), strange(s), charm(c), bottom(b) quarks and gluon(g). (a) and (b) at $Q^2 = 10$ GeV, (c) and (d) at $Q^2 = 100$ GeV and (e) and (f) at $Q^2 = 1000$ GeV.

4.3 Results

The cross section is also measured by CMS at 7 TeV, 8 TeV and 13 TeV in proton proton collisions.

The theoretical calculation for W and charm(c) production cross section times $BR(W \rightarrow lv)$ is done at 13 TeV, 13.6 TeV and 14 TeV CoM and the comparison with measured results obtained at 7 TeV and 8 TeV are also made. The theoretical predictions are made using NNPDF3.1 and HERAPDF20.

4.3.1 7 TeV

Table 4.1 shows the measured cross section of W and charm(c). The correlation between the change in QCD scale and variation in predictions is also determined with the ratio of W^+ and anti-charm($\bar{c}$) and W^- and charm(c) at 7 TeV. The uncertainties in the measured values are due to statistical, systematic and luminosity errors.

Channel	Measured Cross section	Predicted Cross section uncert.[pb]
$W + c$	107.7±3.30(stat.)±6.9(syst.)[pb956]	$109.9 \pm 6.0 (\%PDF)(CT10)$
$\frac{(W^+ + \bar{c})}{(W^- + c)}$	0.954±0.025(stat.)±0.004(syst.)[pb]	$0.942 \pm .004 (\%PDF)(CT10)$

Table 4.1: The measured values of total cross section of W and charm quark and their ratio $R^{\pm}$ at CMS at 7 TeV along with the predicted values [15].

4.3.2 8 TeV

Table 4.2 shows the measured cross section of W and charm(c) and ratio of W^+ and anti-charm($\bar{c}$) and W^- and charm(c). The uncertainties in the measured values are due to statistical, systematic and luminosity errors.

Channel	Measured Cross section	Predicted Cross section uncert.[pb]
$W + c$	117.4±0.60(stat.)±5.4(syst.)[pb]	107.5 ± 6.5
$\frac{(W^+ + \bar{c})}{(W^- + c)}$	0.983±0.010(stat.)±0.016(syst.)[pb]	$0.919 \pm .025$

Table 4.2: The measured values of total cross section of W and charm quark and their ratio $R^{\pm}$ at CMS at 8 TeV along with the predicted cross section at 8 TeV[20].

4.4 13 TeV

Tables 4.3 and 4.4 show the measured cross section of W + charm(c) and predictions at 13 TeV with different Parton Distribution Functions.

PDF set	$\sigma(W + c)[pb]$
CT14nlo	$1056.319 \pm 11.58 \pm 11.92 \pm 12$
NNPDF3.1nlo	$1073.026^{\pm}3.66 \pm 5 \pm 5.14$
ABMP16nlo	$1096.29^{\pm}2 \pm 5.69 \pm 5.83$
CT10nlo	$1092^{\pm}11.91 \pm 11.93 \pm 12.25$
HERAPDF20	$1077.1 \pm 2 \pm 3.9 \pm 4.04$
MMHT	$1157 \pm 10.03 \pm 12.14 \pm 1158$
Measured Value(CMS)	$1026 \pm 31(stat.) \pm 72(syst.)$

Table 4.3: Using MADGRAPH, the NLO predictions for $\sigma(W+c)$. The uncertainties account for PDF, α_s+ PDF and α_s+PDF+statistical, at 13 TeV [21]

PDF set	$\frac{\sigma(W^++\bar{c})}{\sigma(W^-+c)}[pb]$
CT14nlo	$0.96 \pm .22 \pm .264 \pm .267$
NNPDF3.1nlo	$0.9711^{\pm}0.074 \pm 0.101 \pm 0.103$
ABMP16nlo	$0.965^{\pm}0.037 \pm 0.124 \pm 0.17$
CT10nlo	$0.982^{\pm}.231 \pm .232 \pm .235$
HERAPDF20	$0.9775 \pm 0.041 \pm 0.071 \pm 0.077$
Measured Value(CMS)	$0.909 \pm .05(stat.) \pm .020(syst.)$

Table 4.4: Using MADGRAPH, the NLO predictions for $\frac{\sigma(W^++\bar{c})}{\sigma(W^-+c)}$. The uncertainties account for PDF, α_s+ PDF and α_s+PDF+statistical, at 13 TeV

4.4.1 13.6 TeV

Tables 4.5 and 4.6 show the predicted cross section of $W+c$ and ratio of $W^+ + \bar{c}$ and $W^- + c$ at 13.6 TeV using different PDFs.

PDF set	$(W + c)[pb]$
CT14nlo	$1095.14 \pm 11.62 \pm 12.52 \pm 12.60$
NNPDF3.1nlo	$1171.37^{\pm}3.61 \pm 4.97 \pm 5.11$
ABMP16nlo	$1191.33^{\pm}2 \pm 3.13 \pm 3.32$
CT10nlo	$1152^{\pm}11.78 \pm 12.12 \pm 12.18$
HERAPDF20	$1208.41 \pm 1.98 \pm 4.87 \pm 5.02$
Measured Value(CMS)	Cross section to be measured..

Table 4.5: Using MADGRAPH, the NLO predictions for $\sigma(W + c)$ at 13.6 TeV.

PDF set	$\frac{\sigma(W^+ + \bar{c})}{\sigma(W^- + c)}[pb]$
CT14nlo	$0.92 \pm .14 \pm .153 \pm .158$
NNPDF3.1nlo	$0.911^{\pm}0.07 \pm 0.094 \pm 0.097$
ABMP16nlo	$0.96^{\pm}0.039 \pm 0.109 \pm 0.112$
CT10nlo	$0.956^{\pm}.228 \pm .234 \pm .236$
HERAPDF20	$0.9836 \pm 0.041 \pm 0.090 \pm 0.093$
Measured Value(CMS)	Cross section to be measure..

Table 4.6: Using MADGRAPH, the NLO predictions for $\frac{\sigma(W^+ + \bar{c})}{\sigma(W^- + c)}$ at 13.6 TeV.

4.4.2 14 TeV

Tables 4.7 and 4.8 show the predicted cross section of $W + c$ and ratio of $W^+\bar{c}$ and $W^- + c$ at 14 TeV using different PDFs.

PDF set	$(W + c)[pb]$
CT14nlo	$1140.67 \pm 11.38 \pm 11.79 \pm 11.84$
NNPDF3.1nlo	$1212.69^{\pm}3.56 \pm 4.9 \pm 5.09$
ABMP16nlo	$1293.101^{\pm}1.97 \pm 4.92 \pm 4.93$
CT10nlo	$1266.98^{\pm}11.64 \pm 11.92 \pm 11.96$
HERAPDF20	$1260.17 \pm 1.90 \pm 5.34 \pm 5.43$
Measured Value(CMS)	Cross section to be measured..

Table 4.7: Using MADGRAPH, the NLO predictions for $\sigma(W + c)$ at 14 TeV.

PDF set	$\frac{\sigma(W^++\bar{c})}{\sigma(W^-+c)}[pb]$
CT14nlo	$0.993\pm.23 \pm .237 \pm .241$
NNPDF3.1nlo	$0.985^{\pm}0.075 \pm 0.101 \pm 0.105$
ABMP16nlo	$0.991^{\pm}0.04 \pm 0.1235 \pm 0.1238$
CT10nlo	$0.957^{\pm}.227 \pm .234 \pm .236$
HERAPDF20	$0.956\pm0.038 \pm 0.088 \pm 0.091$
Measured Value(CMS)	Cross section to be measure..

Table 4.8: Using MADGRAPH, the NLO predictions for $\frac{\sigma(W^++\bar{c})}{\sigma(W^-+c)}$ at 14 TeV.

4.5 Theoretical Prediction and Uncertainties in cross section of W and charm and the ratio of $\sigma(W^+ + \bar{c})$ and $\sigma(W^- + c)$.

The predicted increase in measurement of cross section of W + charm, $W^+ + \bar{c}$ and $W^- + c$ with the center of mass energy can be seen in Fig. 4.3 The cross section at 13.6 TeV and 14 TeV are yet to measured. In Fig.4.4 shows the measured value of cross section at 13 TeV and the predicted values for different PDFs along with their uncertainties. The error are determined with both Monte-carlo replicas and Hessian error eigen vector method. The correlation between the change in QCD scale and the variation in predictions are also determined. Results at 13 TeV, 13.6 TeV and 14 TeV are in Fig.4.5, 4.6 and 4.7
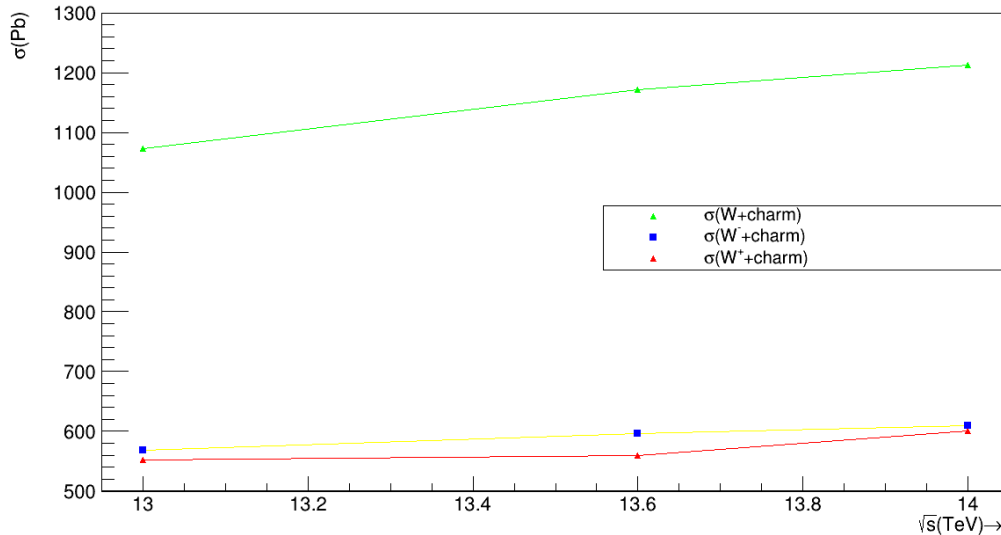
(a)

Figure 4.3: The predicted increase in the cross section of $W + c$, $W^- + c$ and $W^+ + \bar{c}$ with increase in CoM energy at NLO and at 13 TeV value of cross section is measured at NLO.

(a)

(b)
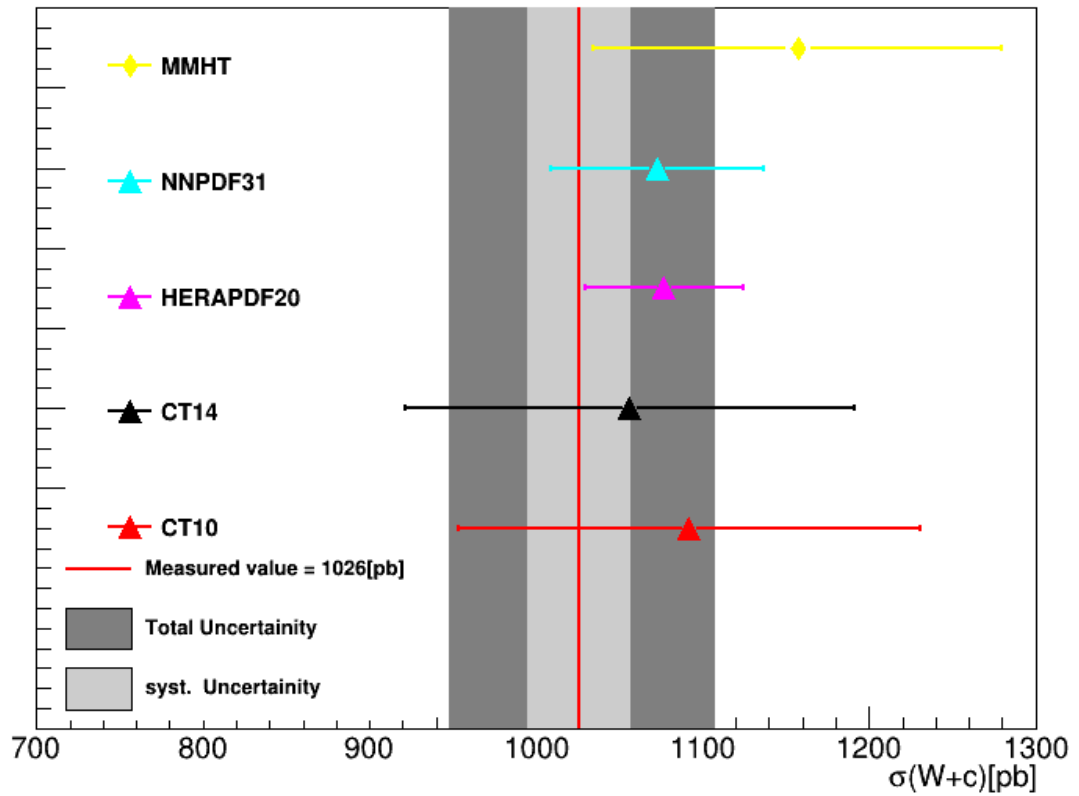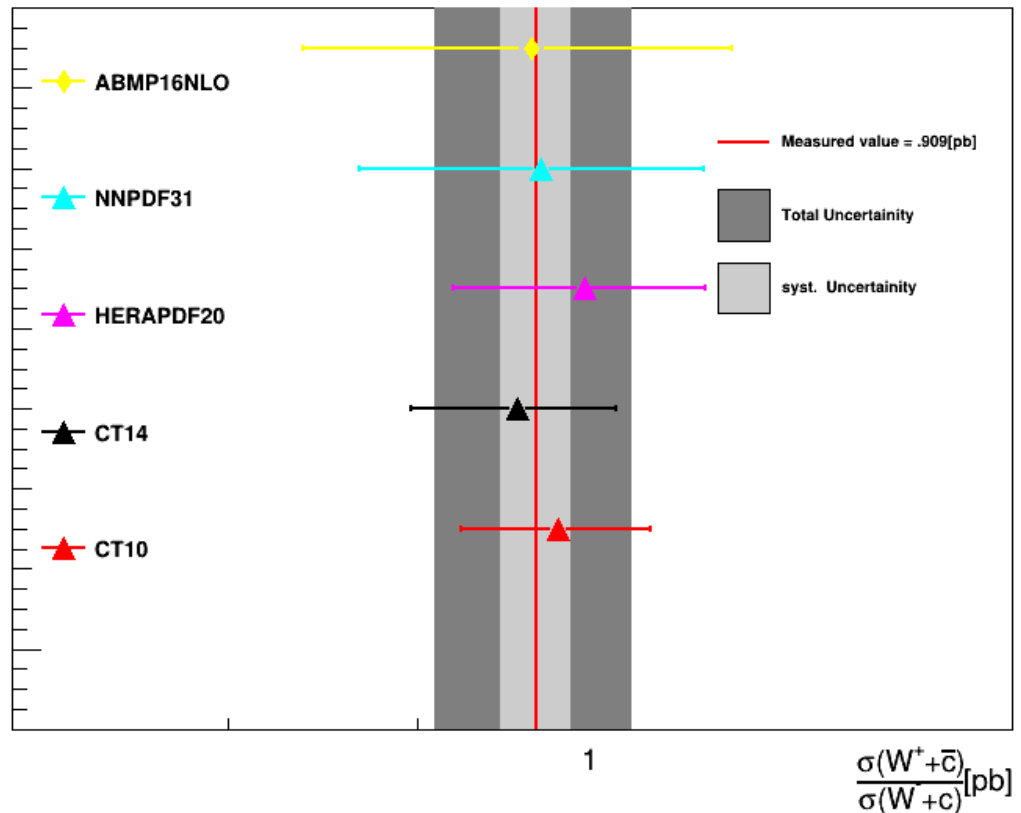
Figure 4.4: The plot (a) shows inclusive fiducial cross section of $(W+c)$ and (b) shows cross section ratio $\frac{\sigma(W^++c)}{\sigma(W^-+c)}$ at 13 TeV. The vertical red line shows mean measured value, while inner dark green band shows statistical uncertainty and outer green

σ at 13 TeV using NNPDF31 :305000

(a)

σ at 13 TeV using HERA :61100

(b)

(c)

(d)
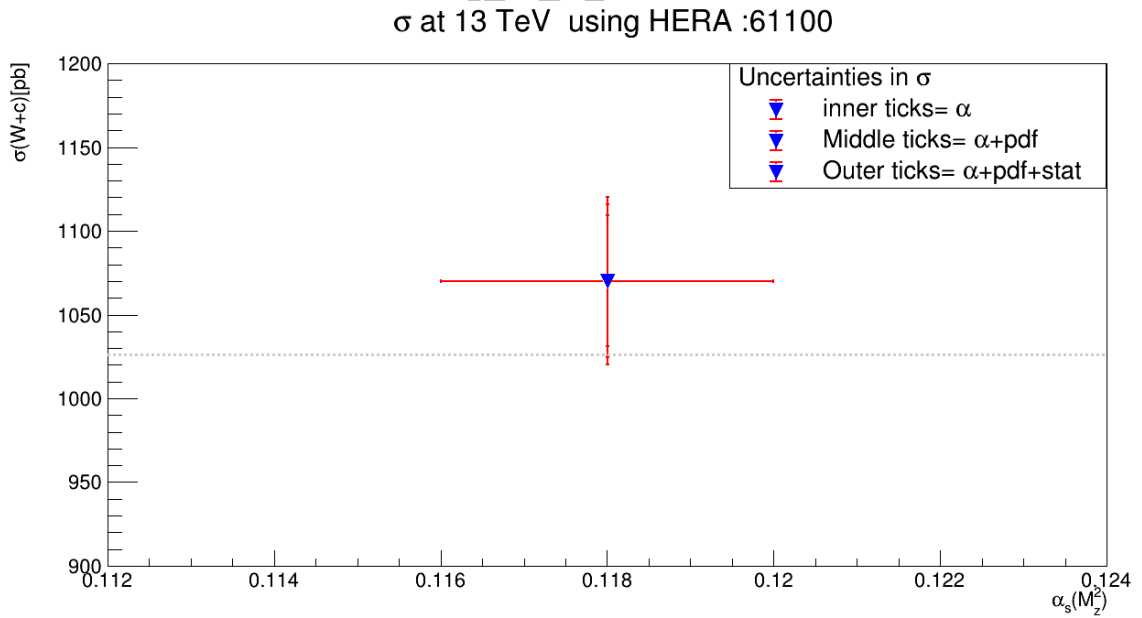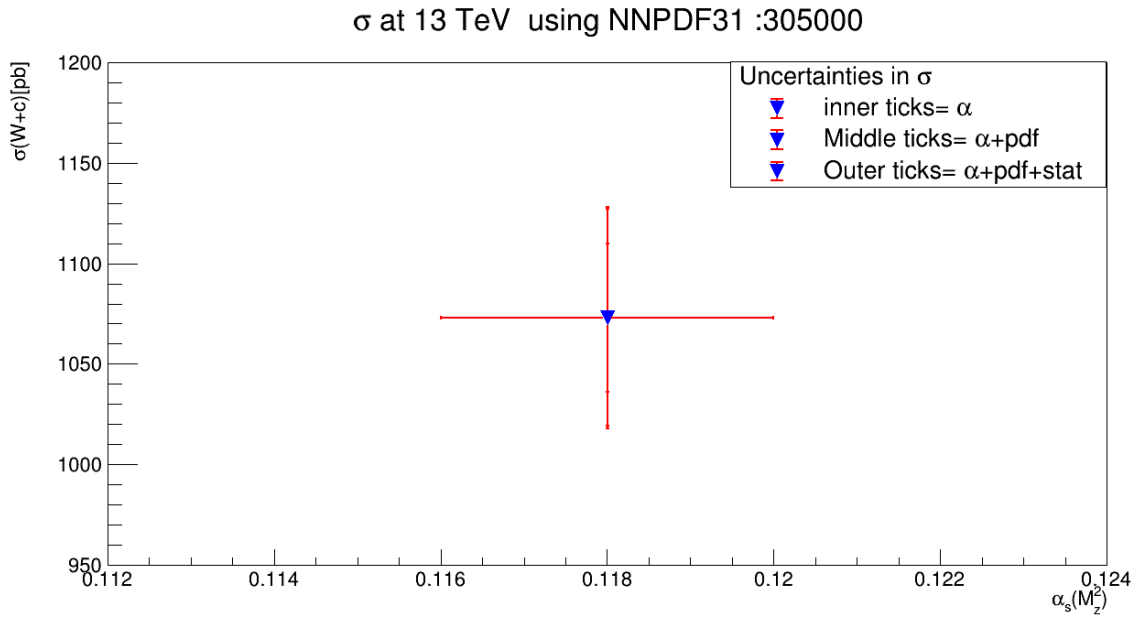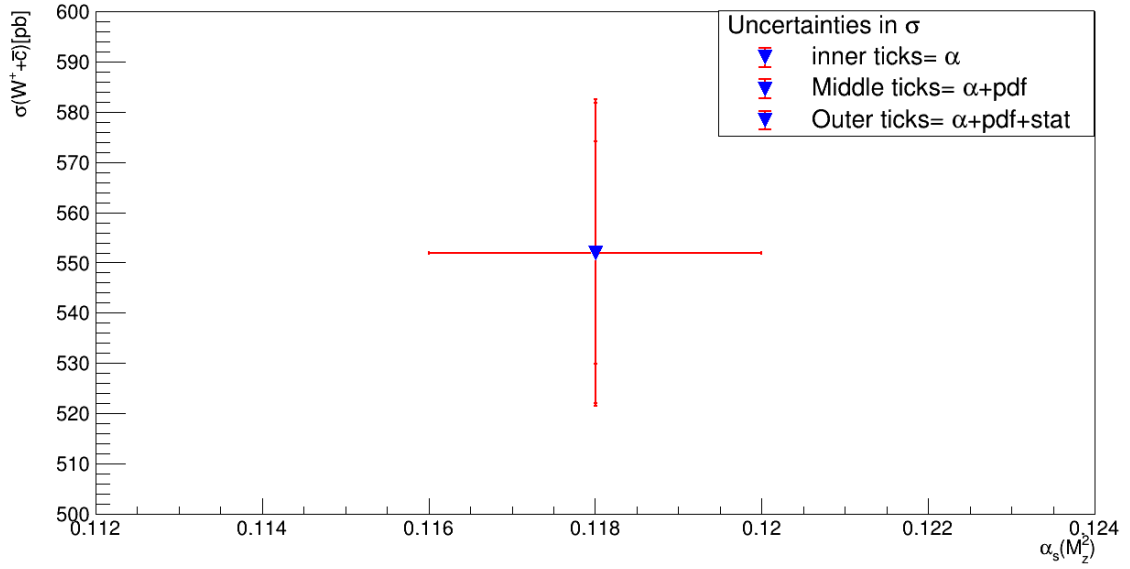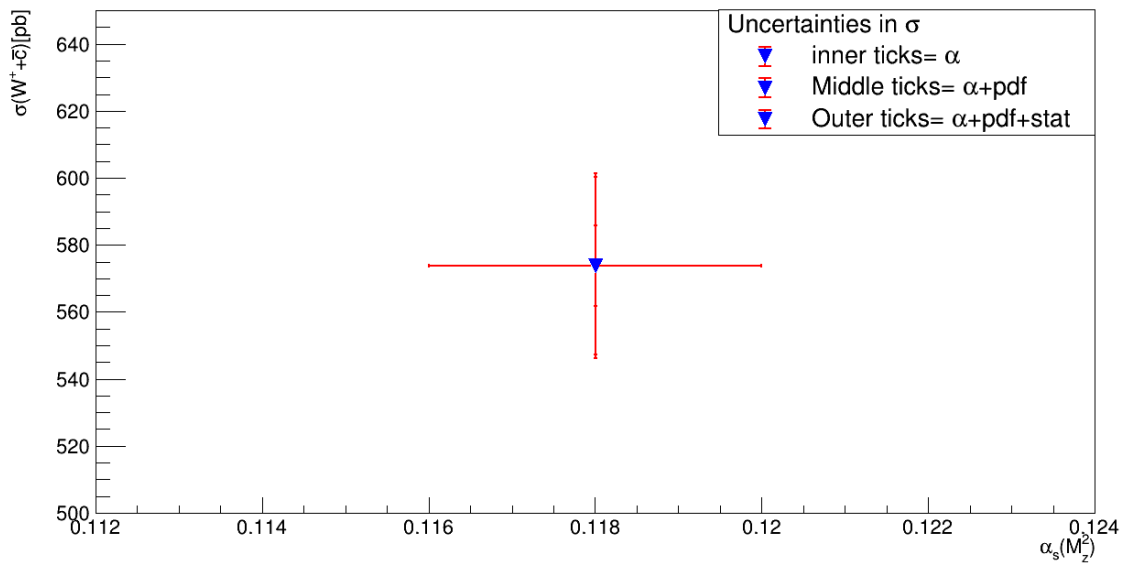
σ at 13 TeV using NNPDF31 :305000

(e)
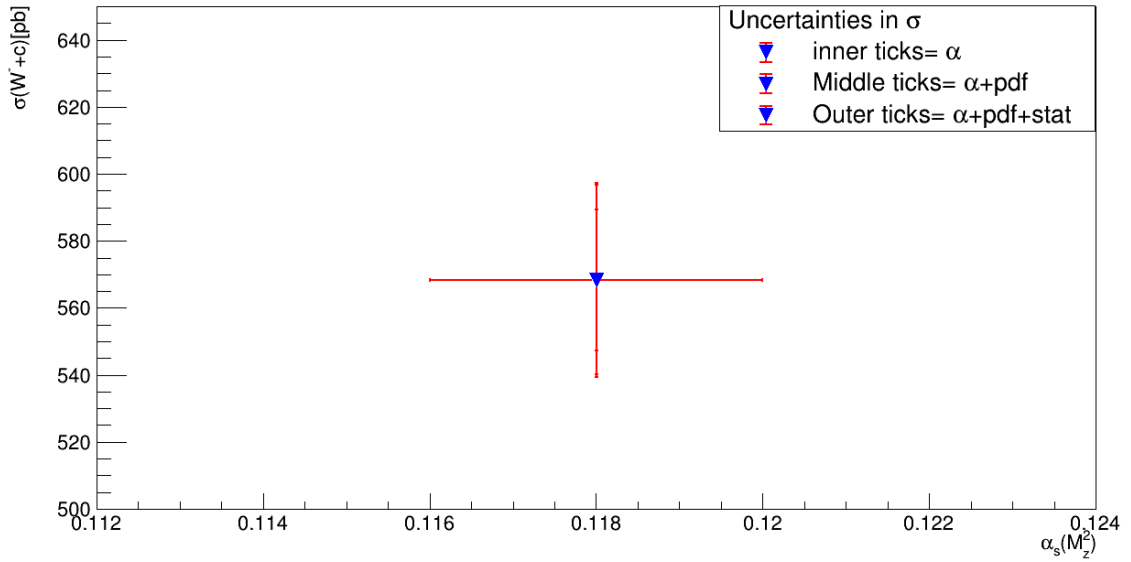
σ at 13 TeV using HERA :61100

(f)

(g)

(h)
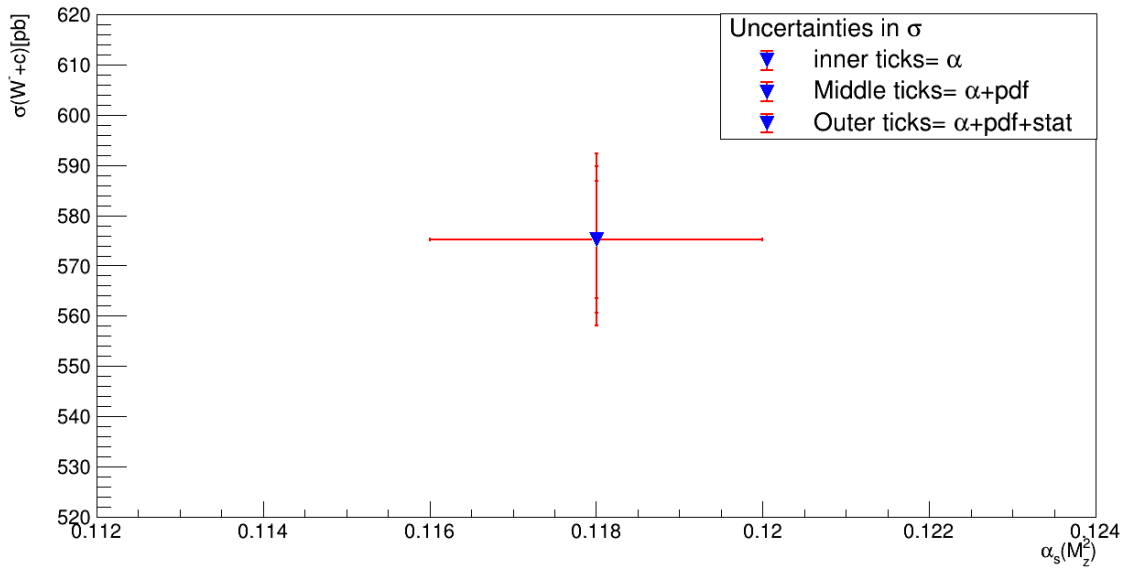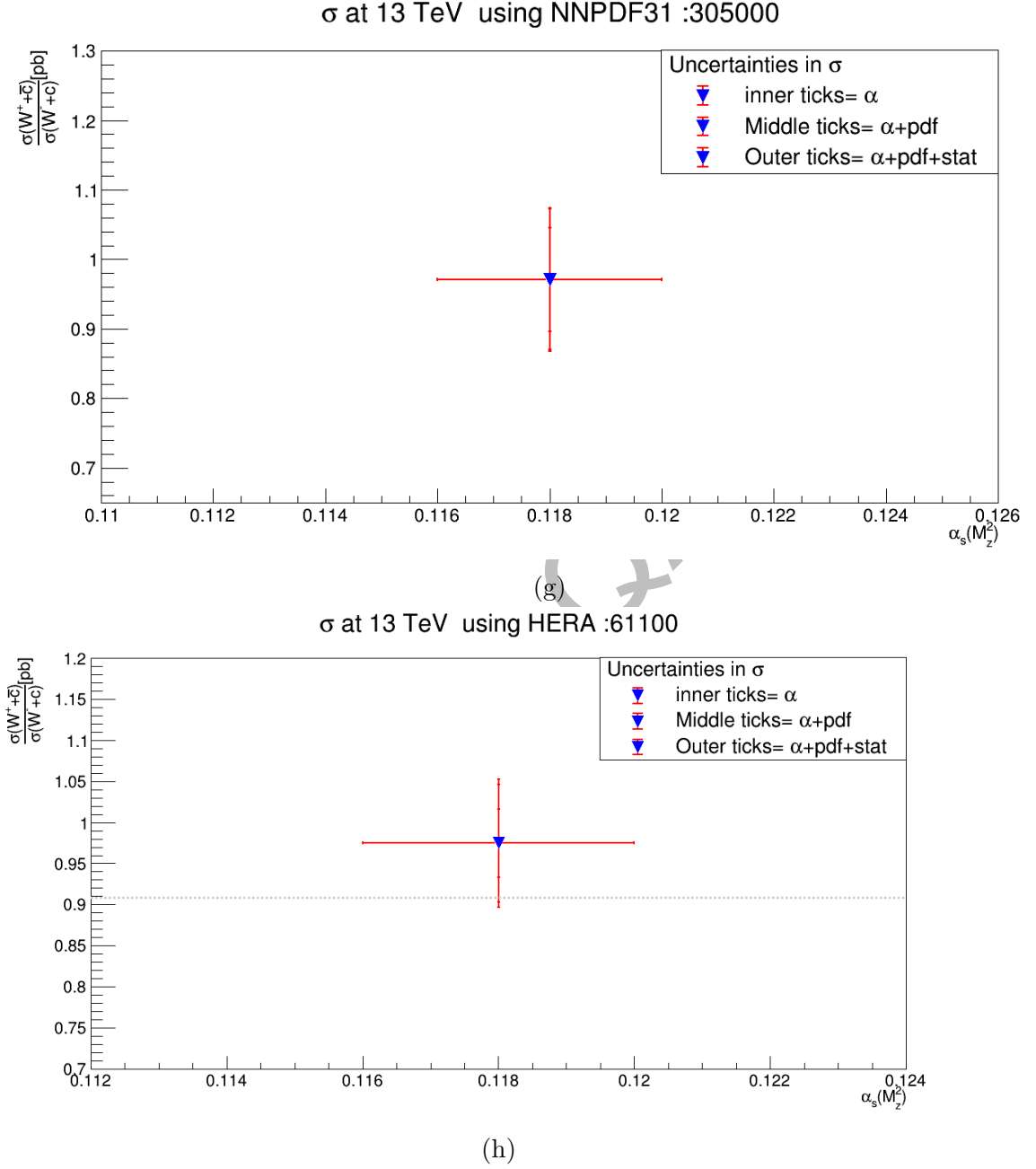
Figure 4.5: Plots (a) and (b) show predicted cross section and uncertainties in the cross section of $W + c$, (c) and (d) show predicted cross section and uncertainties in the cross section of $W^+ + \bar{c}$, (e) and (f) show predicted cross section and uncertainties in the cross section of $W^- + c$ while (g) and (h) show predicted cross section and uncertainties in the cross section of $\frac{W^+ + \bar{c}}{W^- + c}$ by using NNPDF31 and HERAPDF at 13 TeV .

(a)

(b)

(c)

(d)

(e)

(f)

(g)

(h)
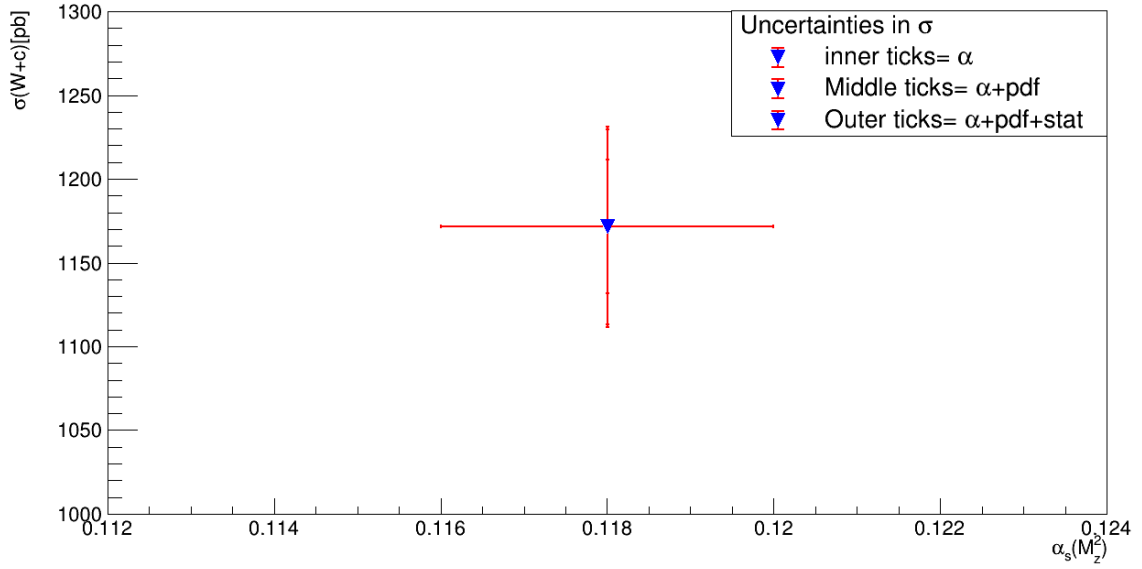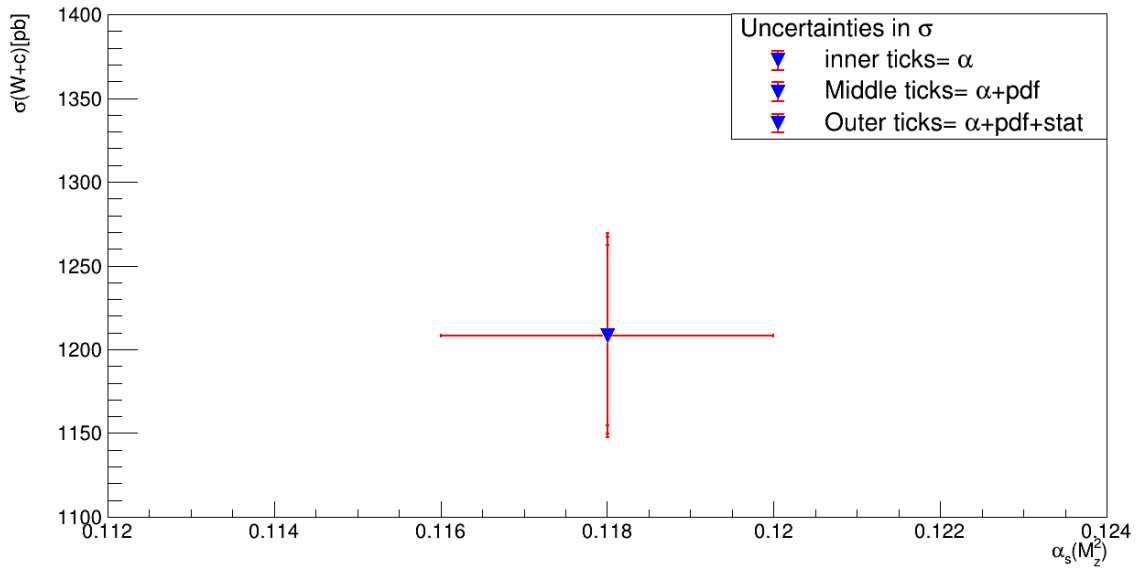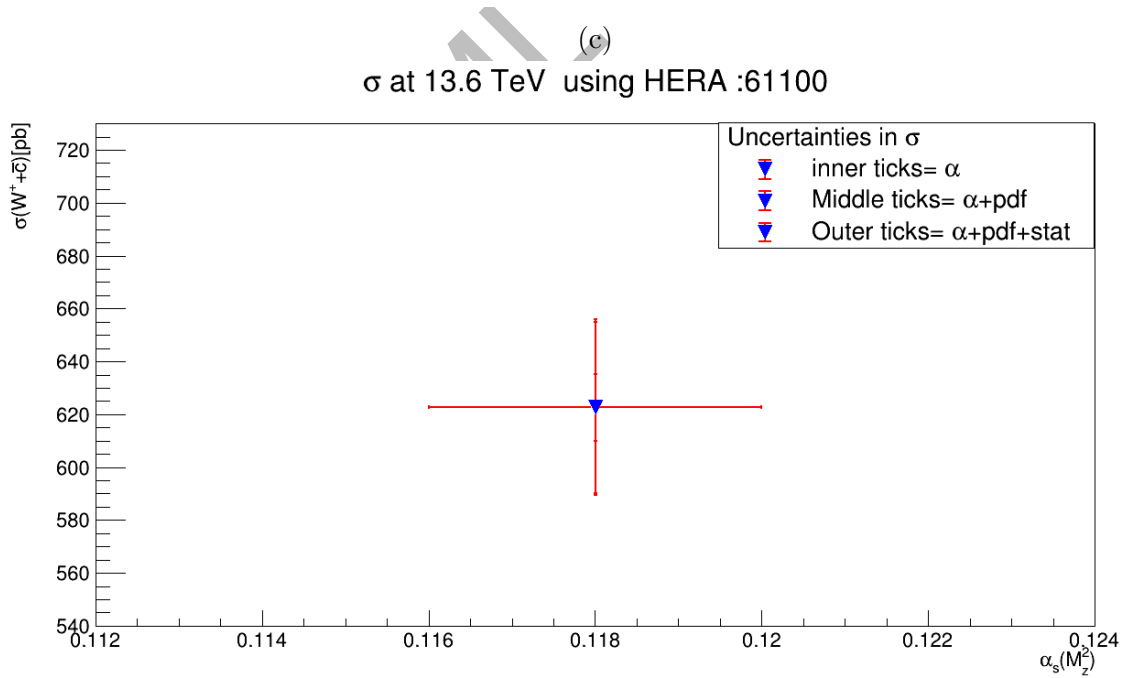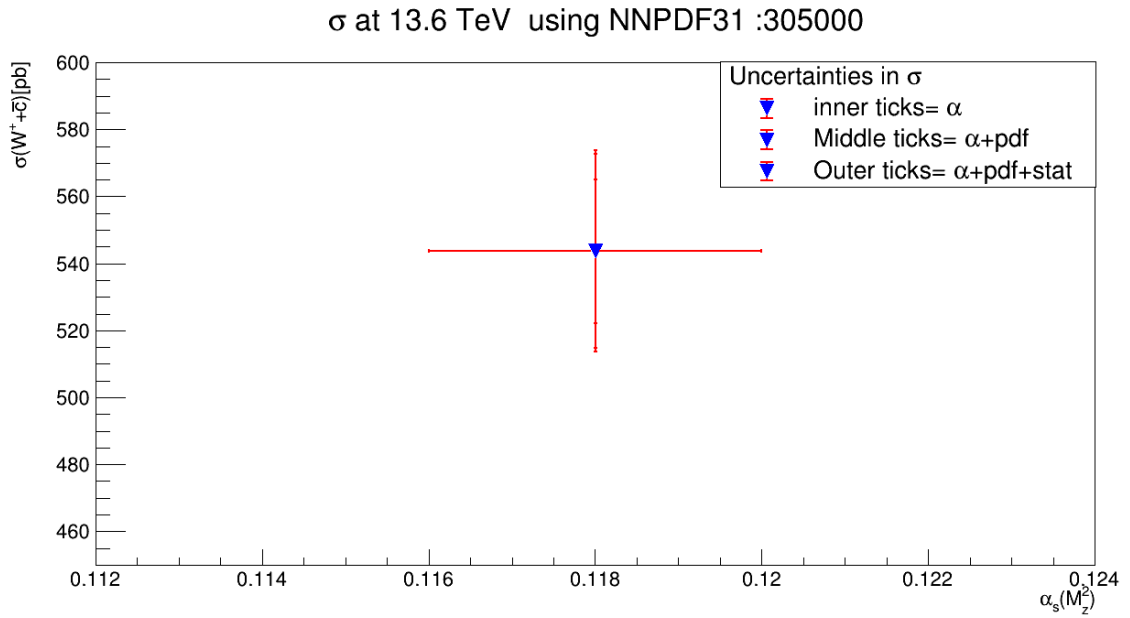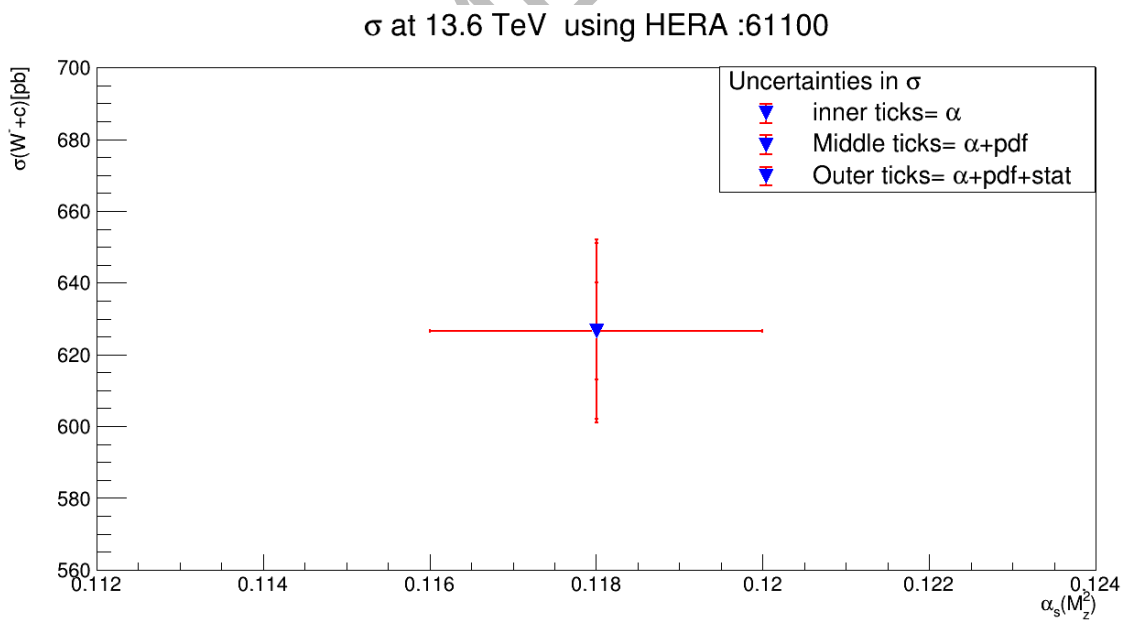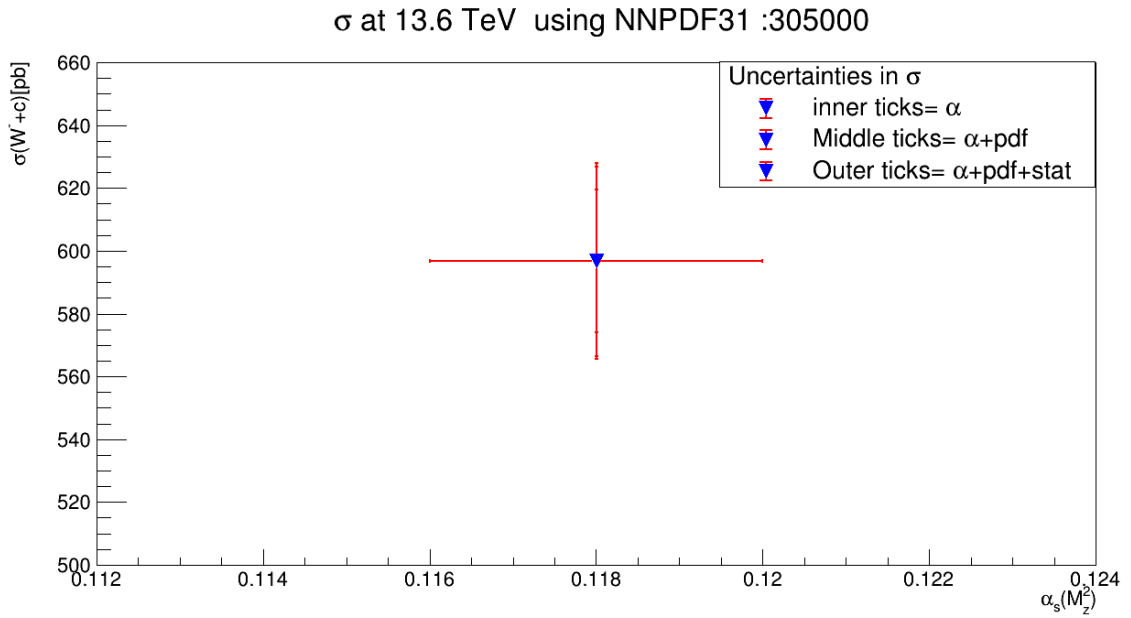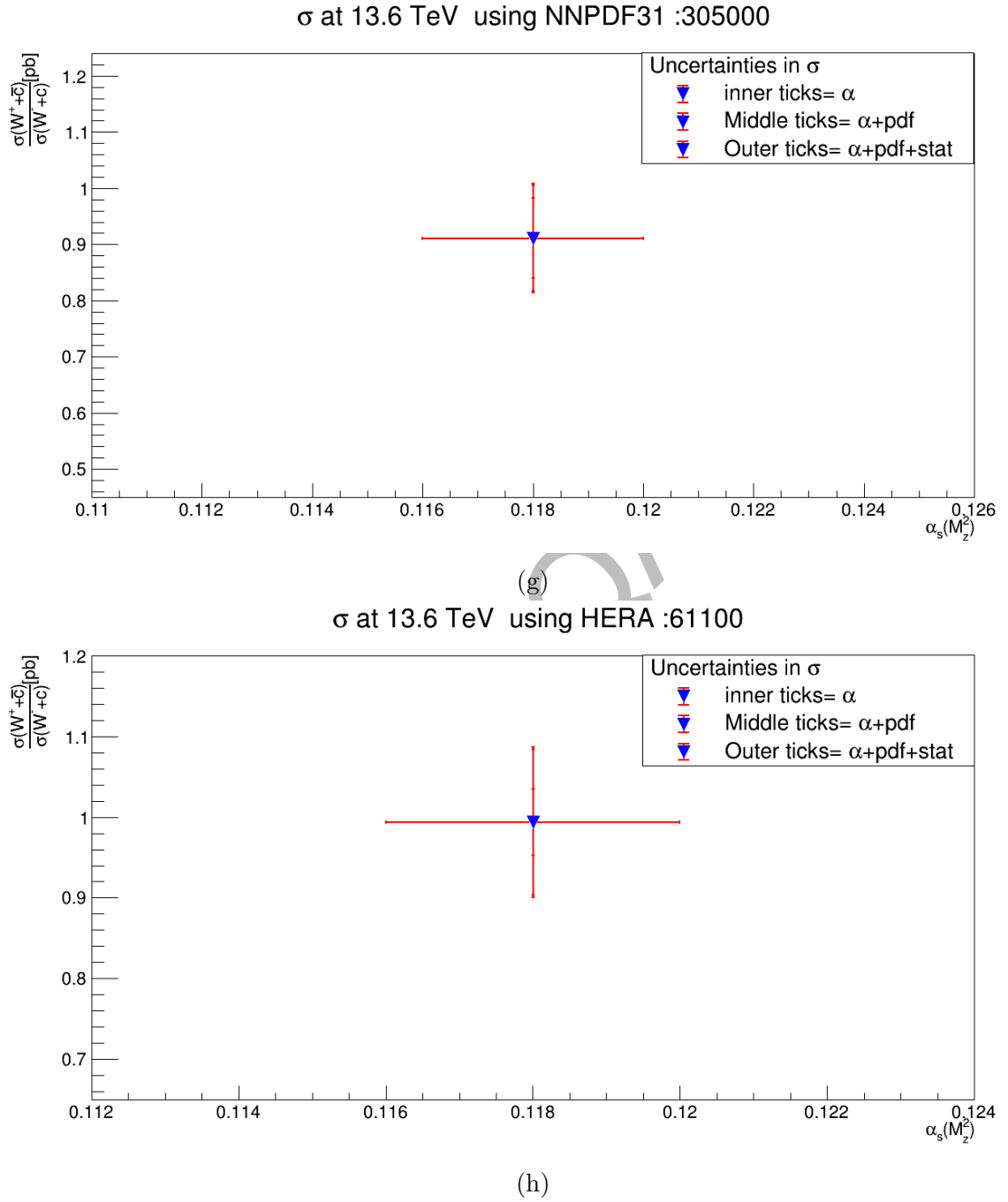
Figure 4.6: Plots (a) and (b) show predicted cross section and uncertainties in the cross section of $W + c$, (c) and (d) show predicted cross section and uncertainties in the cross section of $W^+ + \bar{c}$, (e) and (f) show predicted cross section and uncertainties in the cross section of $W^- + c$ while (g) and (h) show predicted cross section and uncertainties in the cross section of $\frac{W^+ + \bar{c}}{W^- + c}$ by using NNPDF31 and HERAPDF at 13.6 TeV.

σ at 14 TeV using NNPDF31 :305000

(a)

σ at 14 TeV using HERA :61100

(b)

(c)

(d)

(e)

(f)

σ at 14 TeV using NNPDF31 :305000

(g)

σ at 14 TeV using HERA :61100

(h)
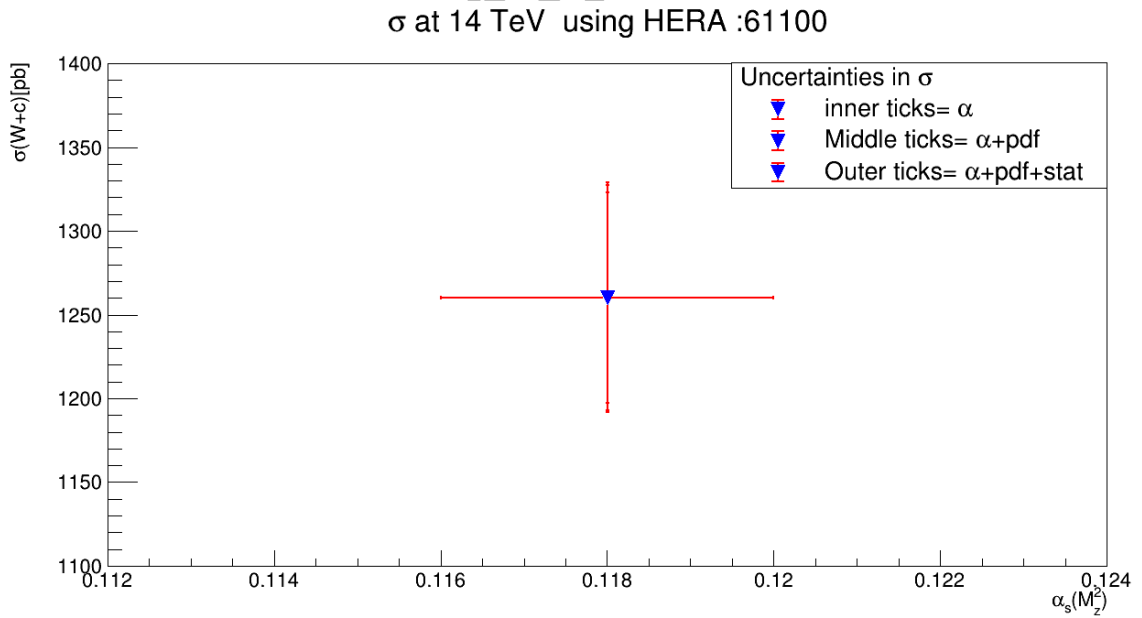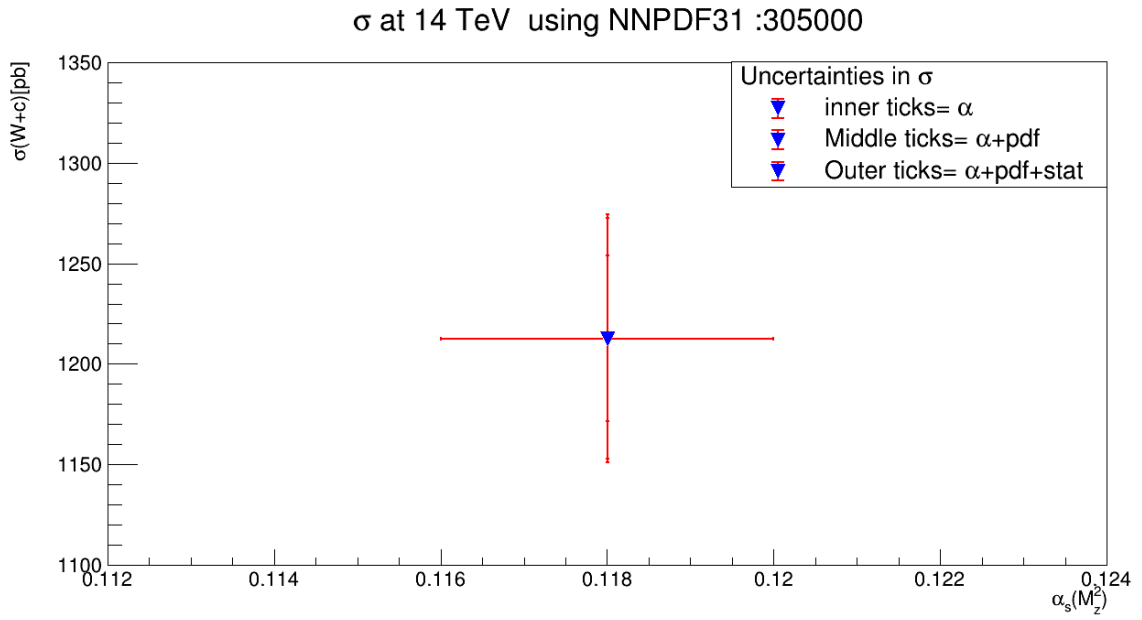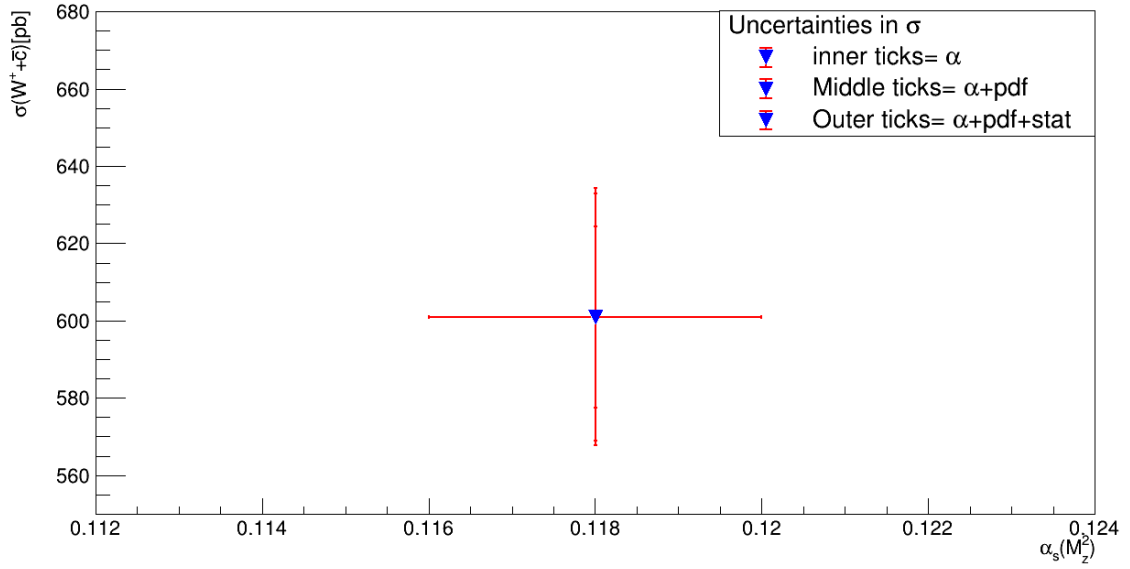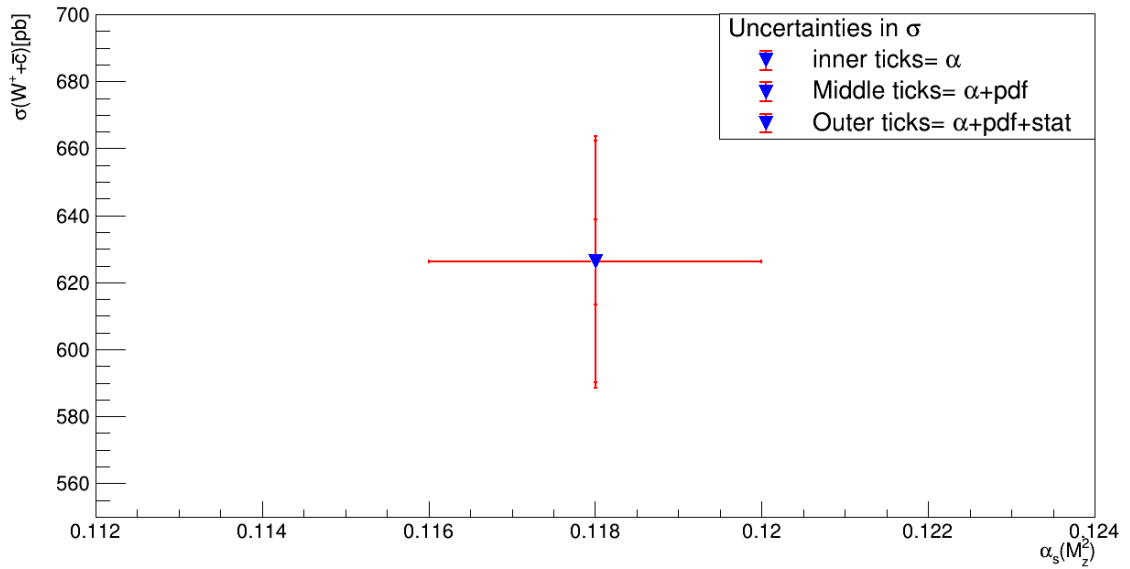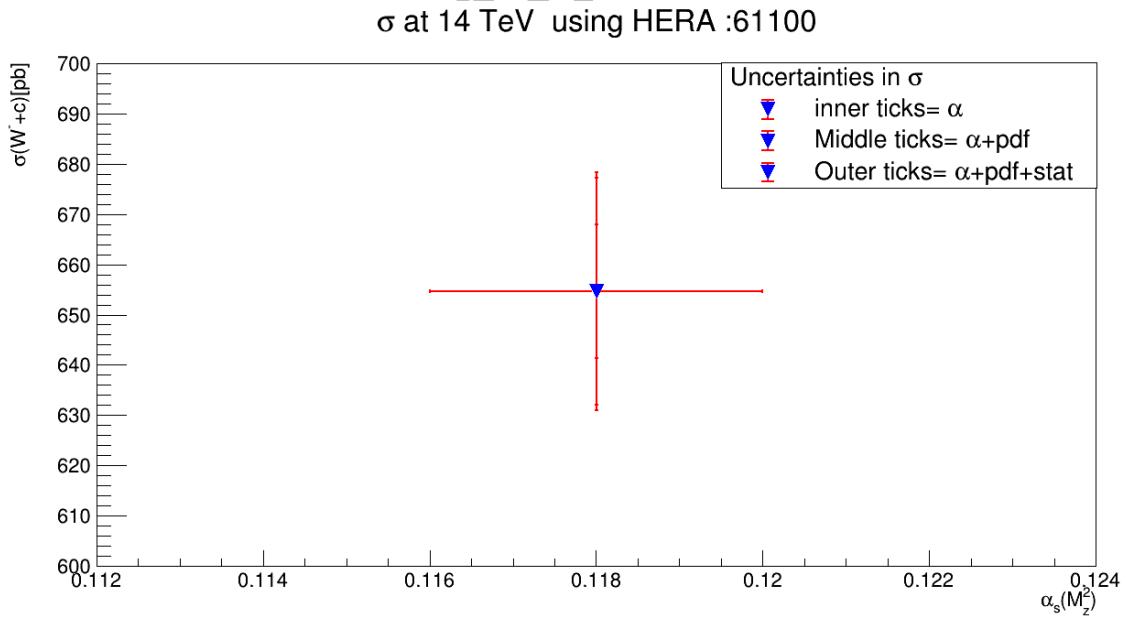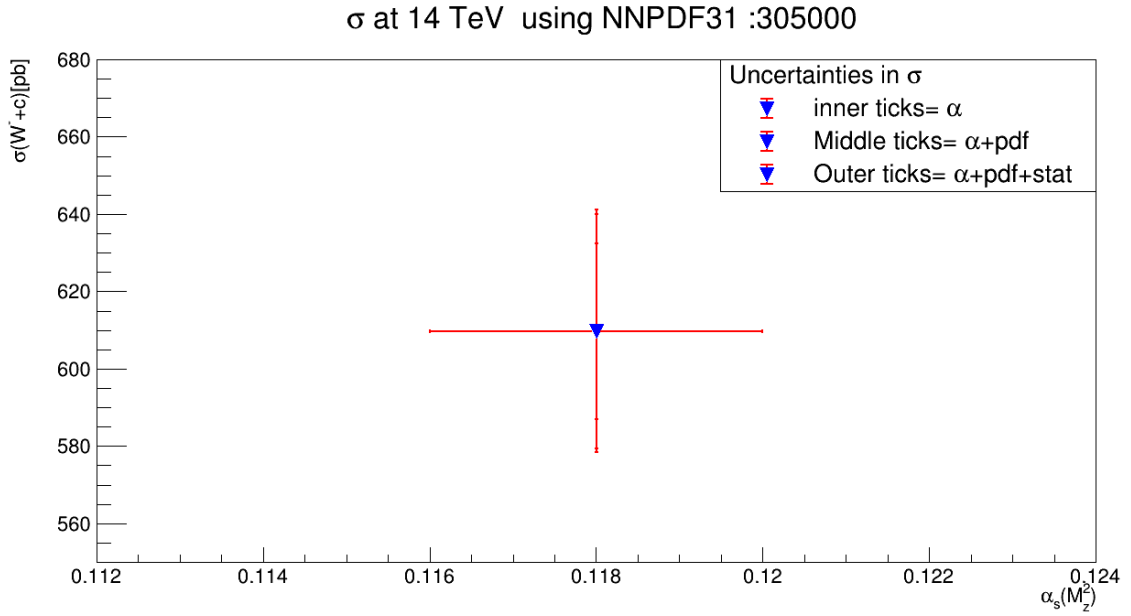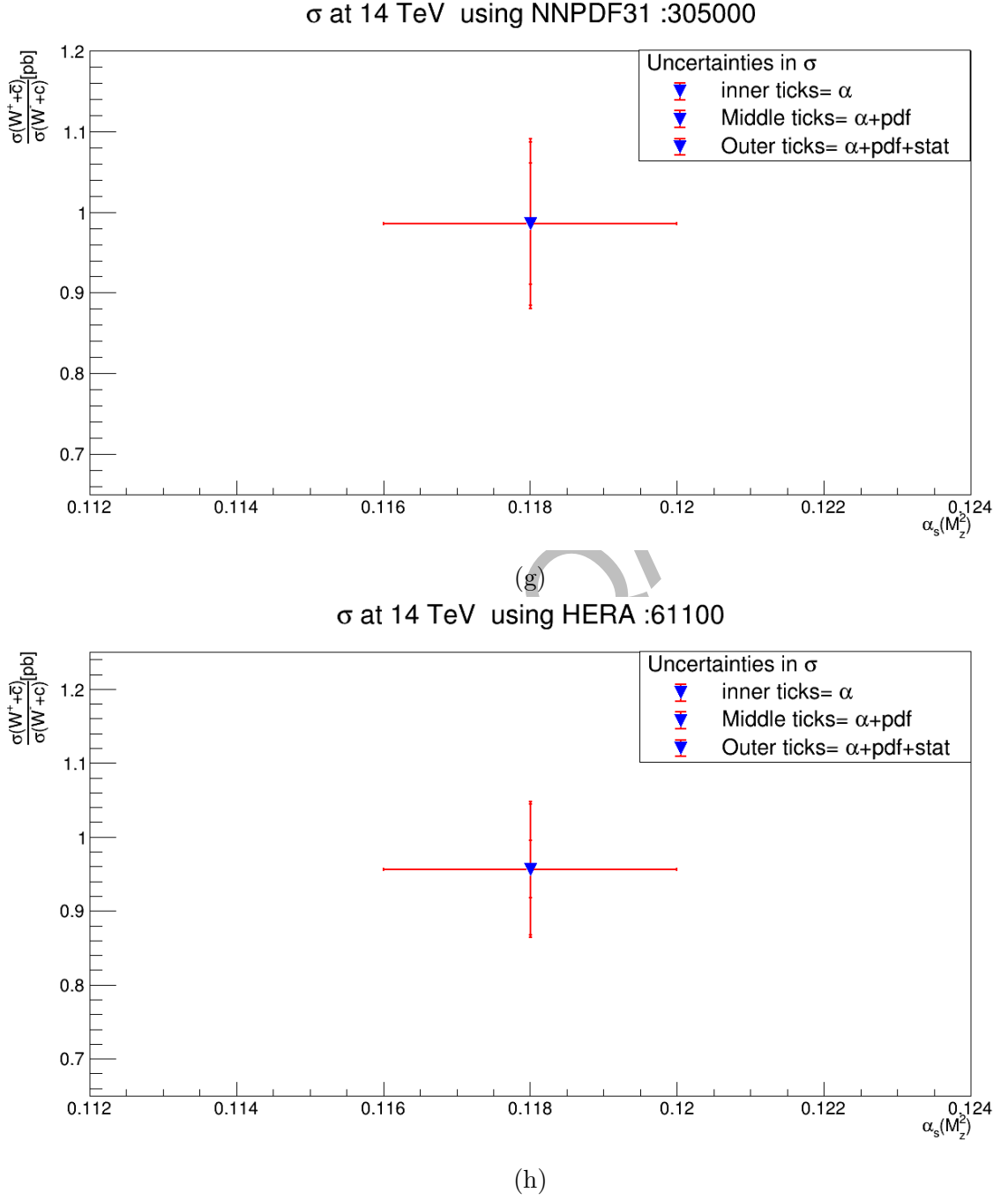
Figure 4.7: Plots (a) and (b) show predicted cross section and uncertainties in the cross section of $W + c$, (c) and (d) show predicted cross section and uncertainties in the cross section of $W^+ + \bar{c}$, (e) and (f) show predicted cross section and uncertainties in the cross section of $W^- + c$ while (g) and (h) show predicted cross section and uncertainties in the ratio of $\frac{\sigma(W^+ + \bar{c})}{\sigma(W^- + c)}$ by using NNPDF31 and HERAPDF at 14 TeV .

4.6 Variation in cross section with QCD scale

The predicted increase in cross section values of $W+c$, $W^+\bar{c}$, $W^- + c$ and $\frac{W^+\bar{c}}{W^-+c}$ boson with the change in value of strong coupling constant α_s at 13 TeV, 13.6 TeV and 14 TeV is shown in Fig.4.8. The variation in the predicted cross section with change of factorization(μ_F) and renormalization scale (μ_R) at 13 TeV, 13.6 TeV and 14 TeV are shown in Fig.4.9, 4.10 and 4.12
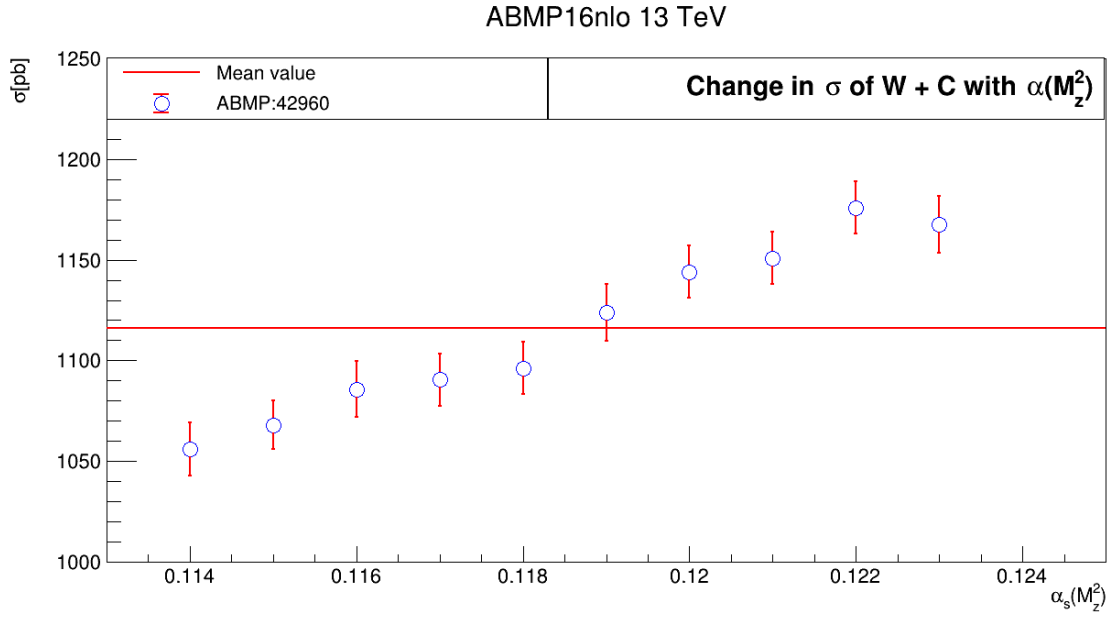
(a)
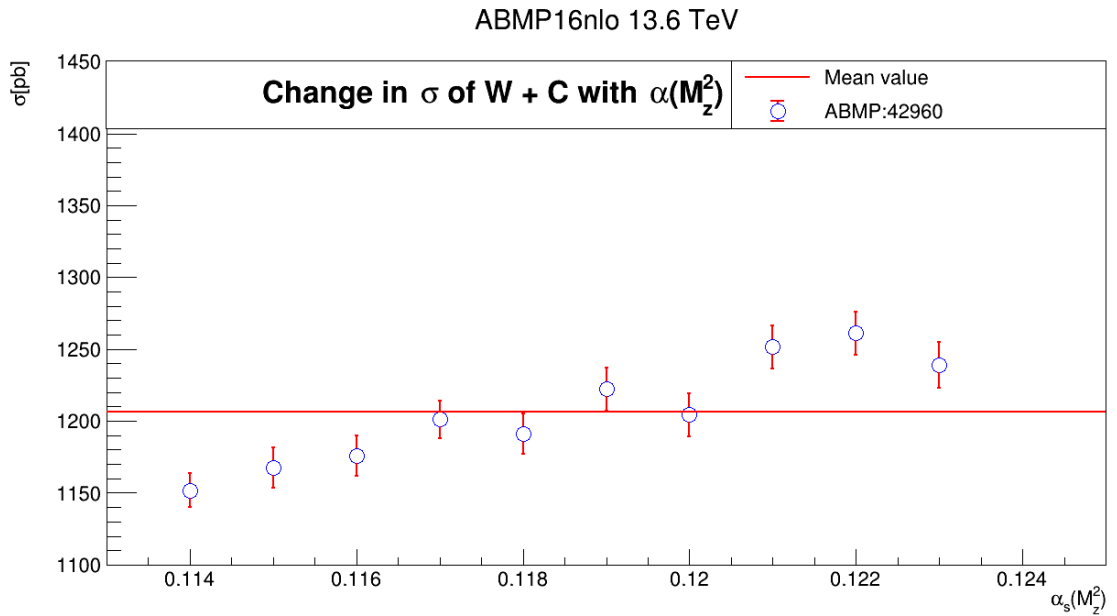
(b)
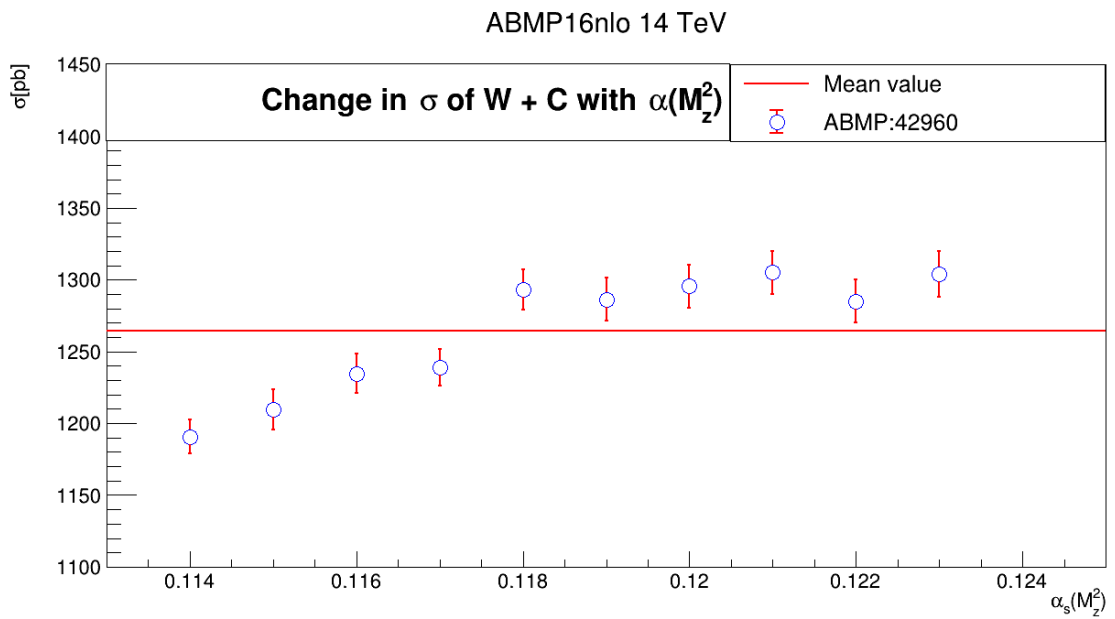
(c)

Figure 4.8: Predicted variation in cross section of W and charm with the choice of $\alpha_s(M_Z^2)$ at CoM energy (a) 13 TeV, (b) 13.6 TeV and (c) 14 TeV.

(a)

(b)

σ at 13 TeV using NNPDF :305000

(c)

σ at 13 TeV using HERAPDF :61100

(d)

σ at 13 TeV using NNPDF :305000

(e)

σ at 13 TeV using HERAPDF :61100

(f)

(g)

(h)
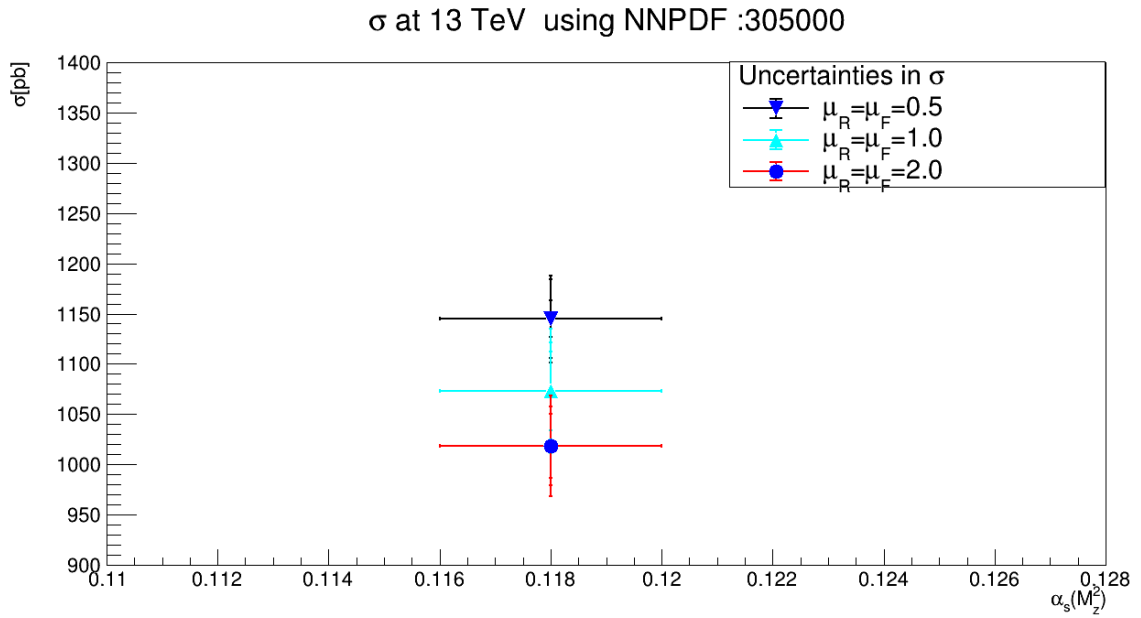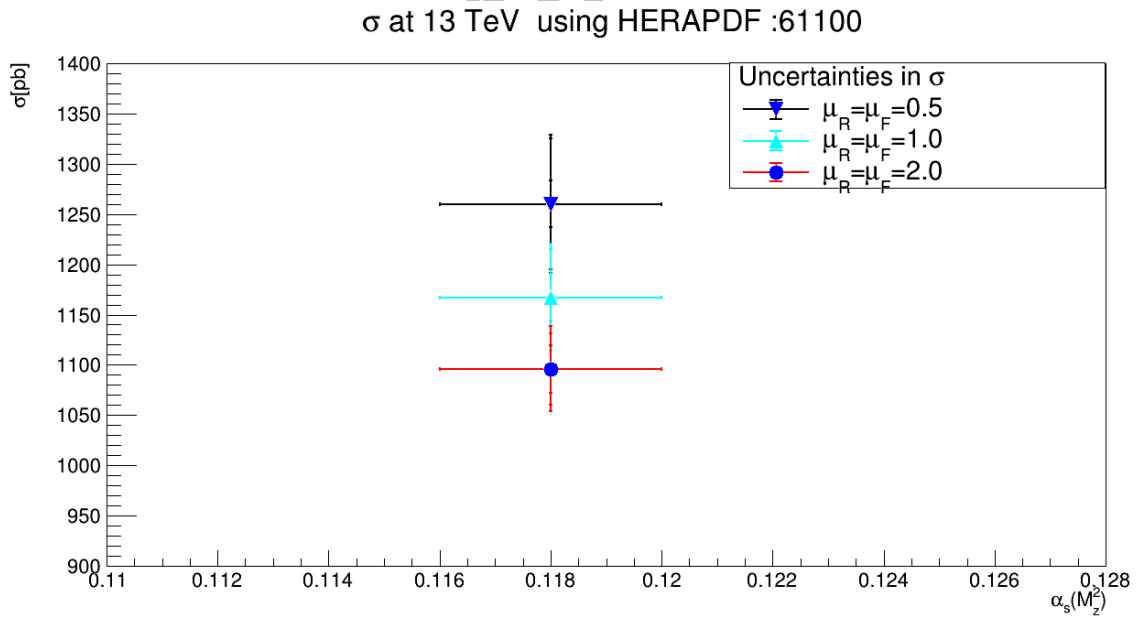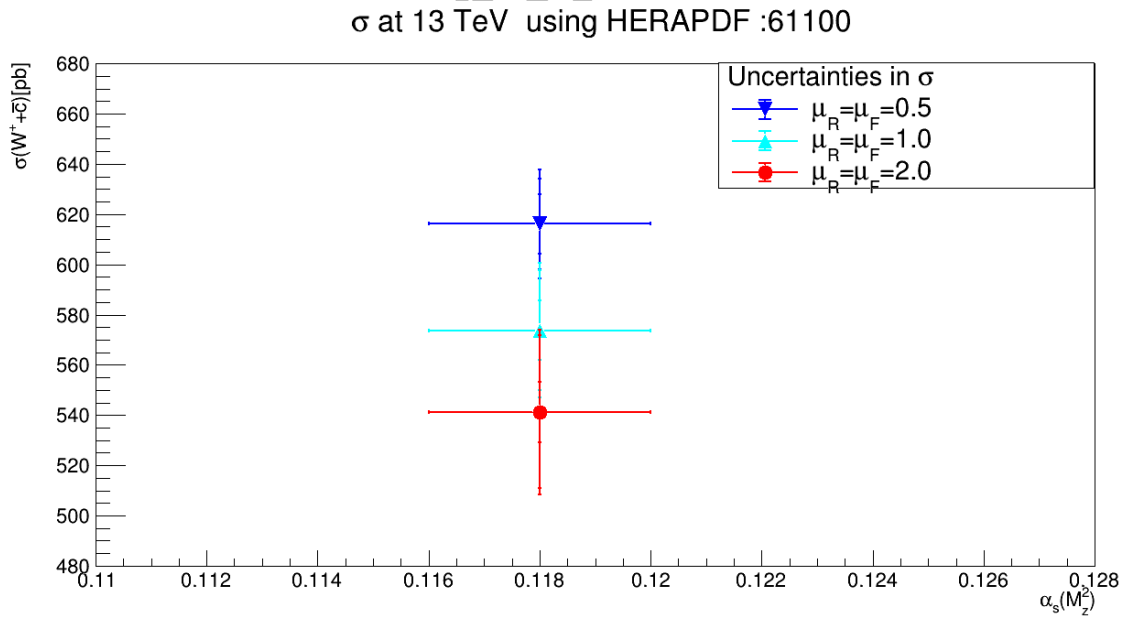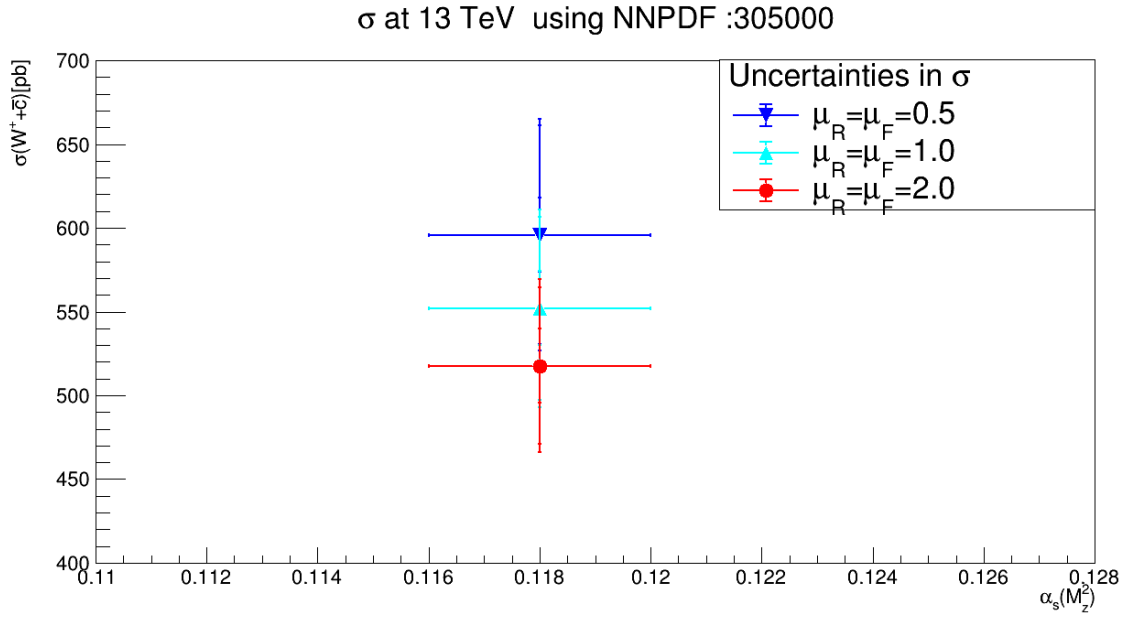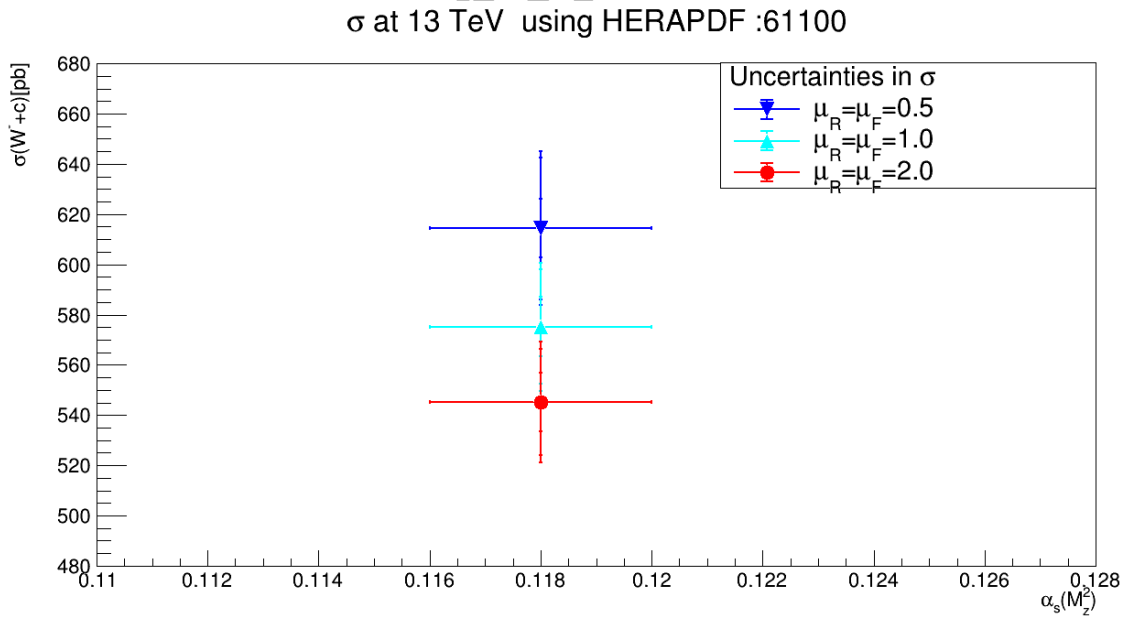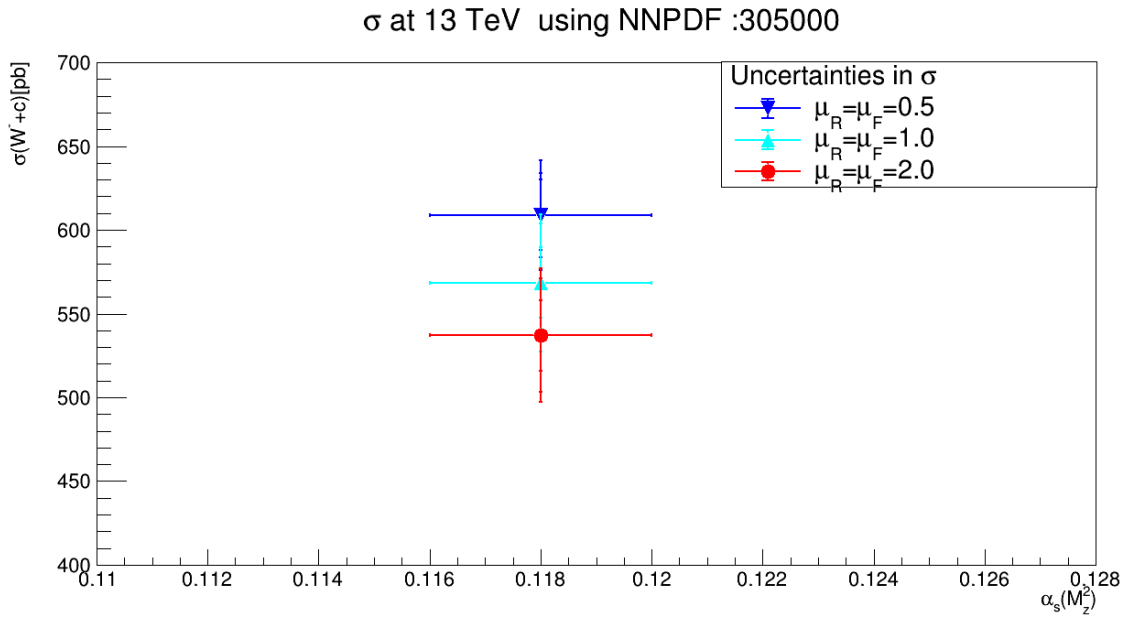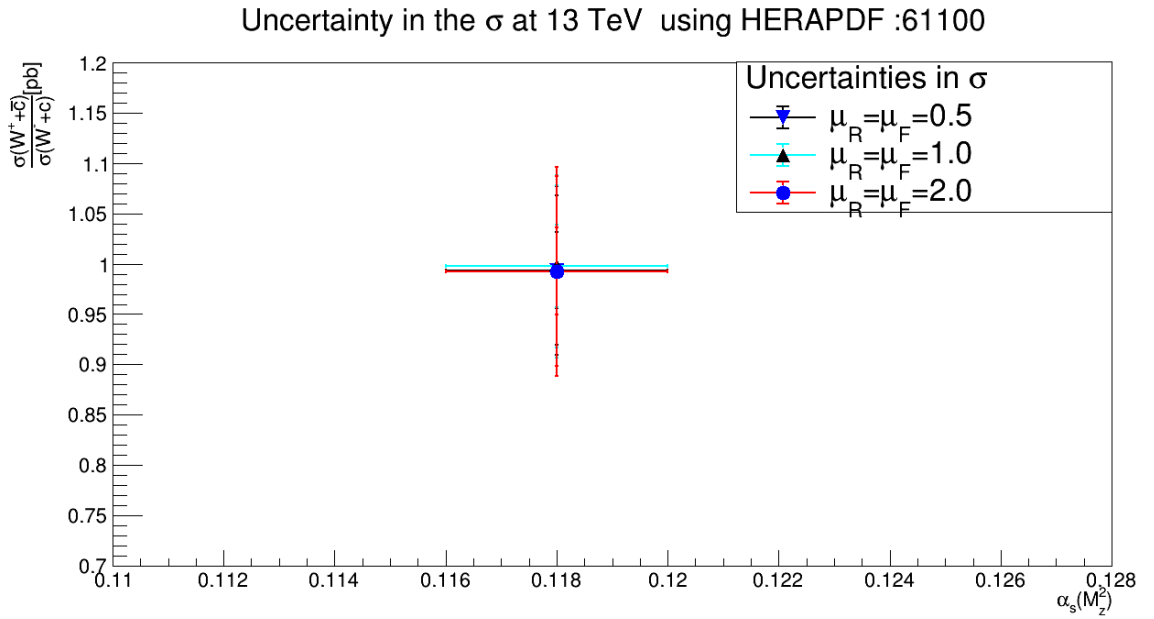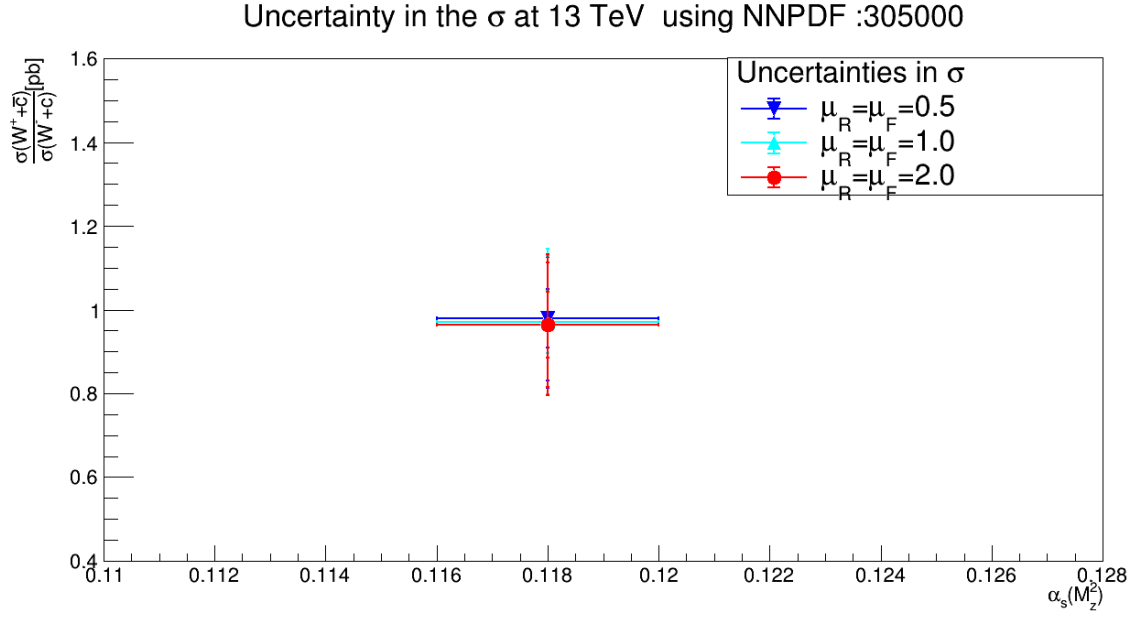
Figure 4.9: Plots (a) and (b) show the predicted change in cross section of $W + c$, (c) and (d) show the predicted change in the cross section of $w^+ + \bar{c}$, (e) and (f) show the predicted change in cross section of $W^- + c$ while (e)and (f) show the predicted change in cross section at different QCD scale (μ_R and μ_F) at 13 TeV. The vertical error bars represent: inner (PDF), middle (α_s), outer (PDF+α_s combined) errors.

(a)

(b)

σ at 13.6 TeV using NNPDF :305000

(c)

σ at 13.6 TeV using HERAPDF :61100

(d)

(e)

(f)

Uncertainty in the σ at 13.6 TeV using NNPDF :305000

(g)

Uncertainty in the σ at 13.6 TeV using HERAPDF :61100

(h)
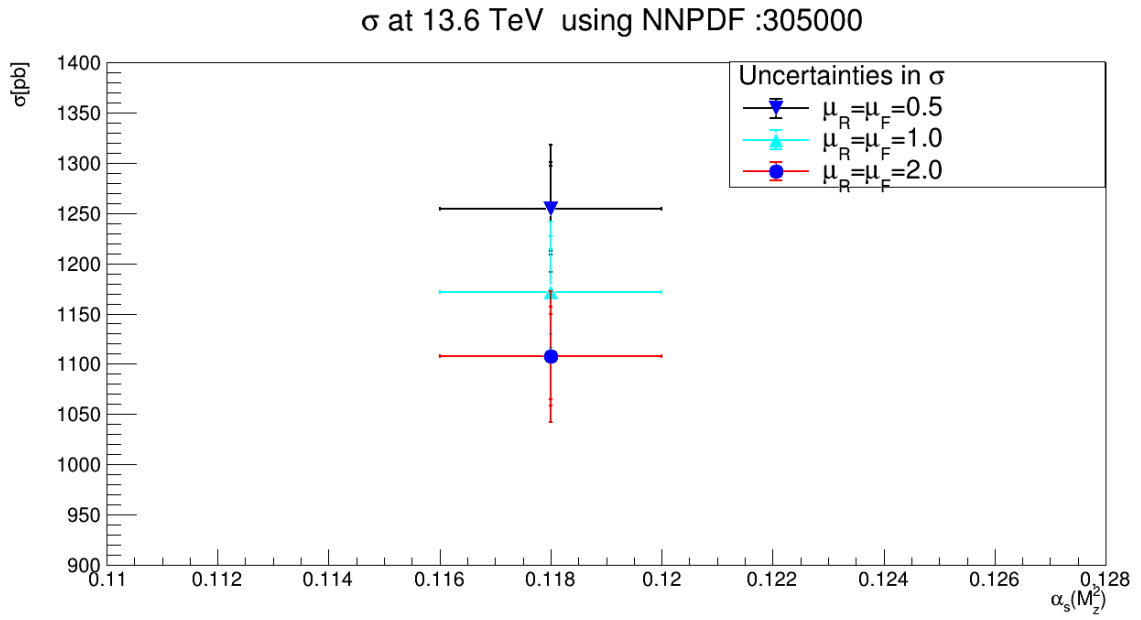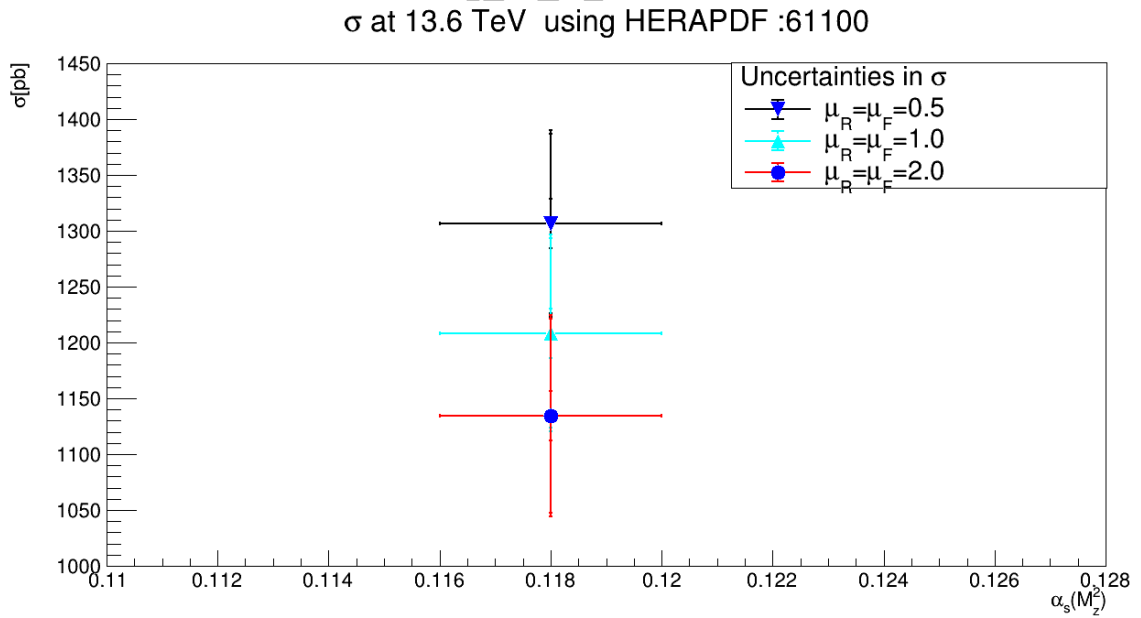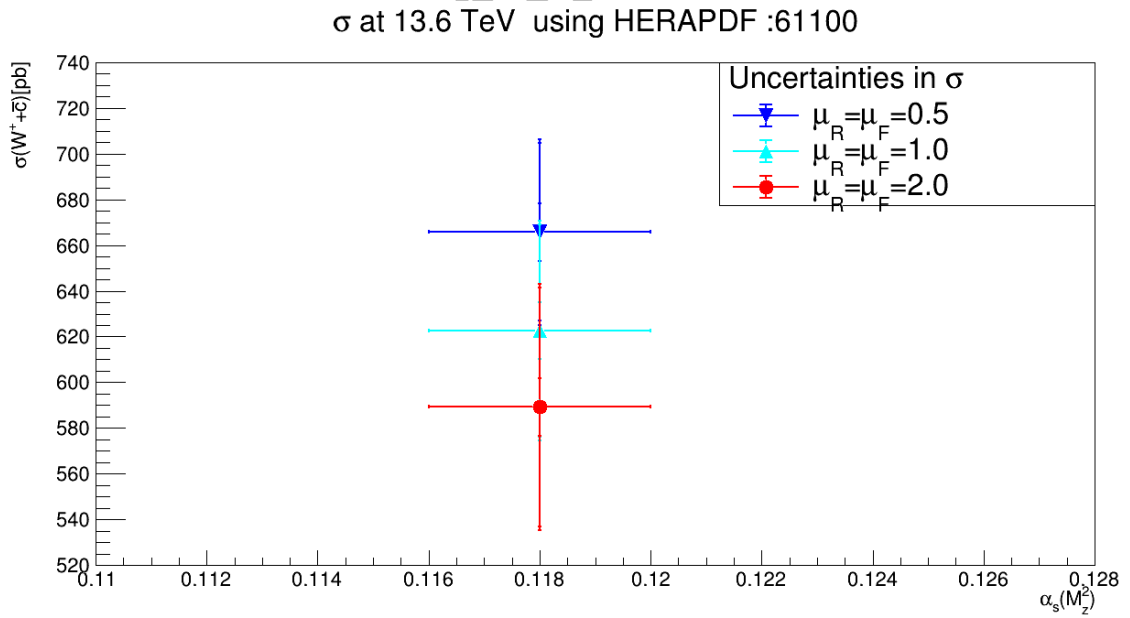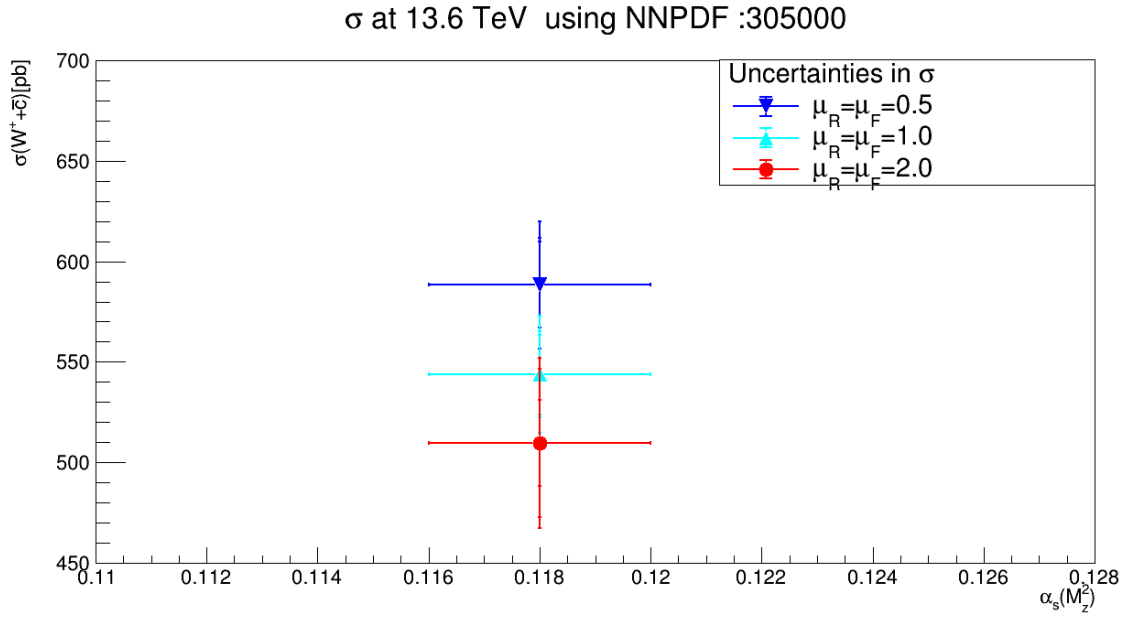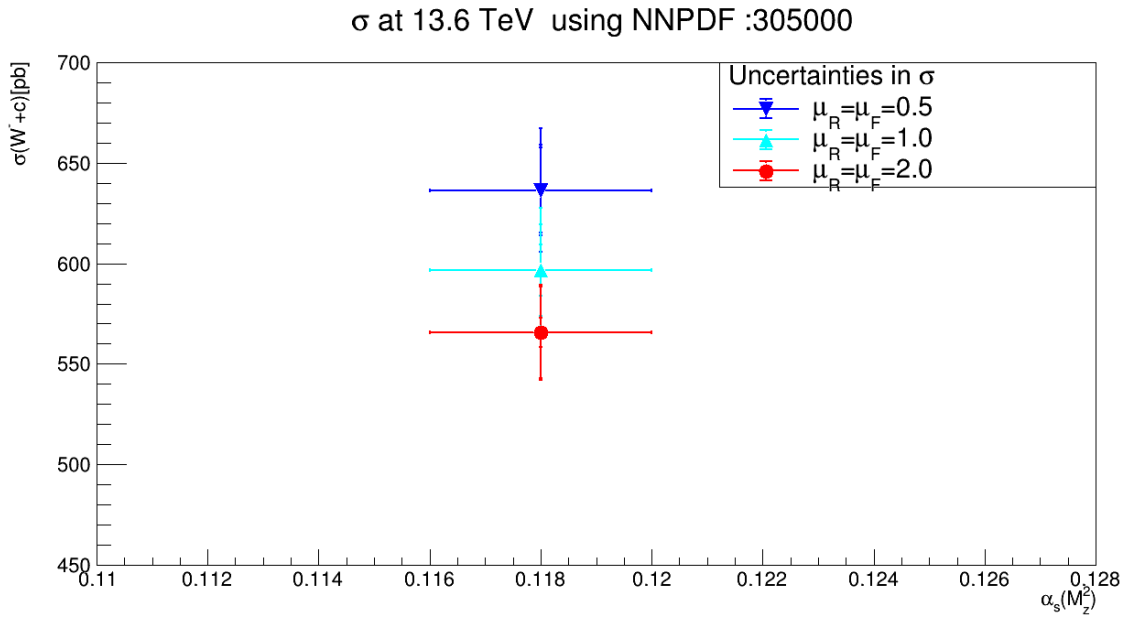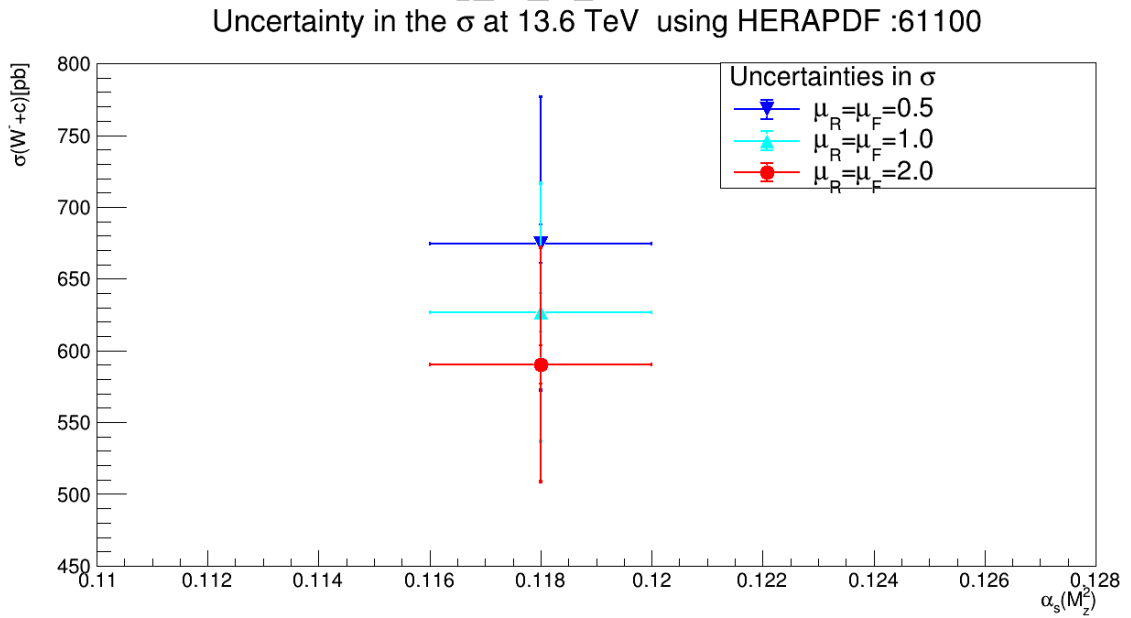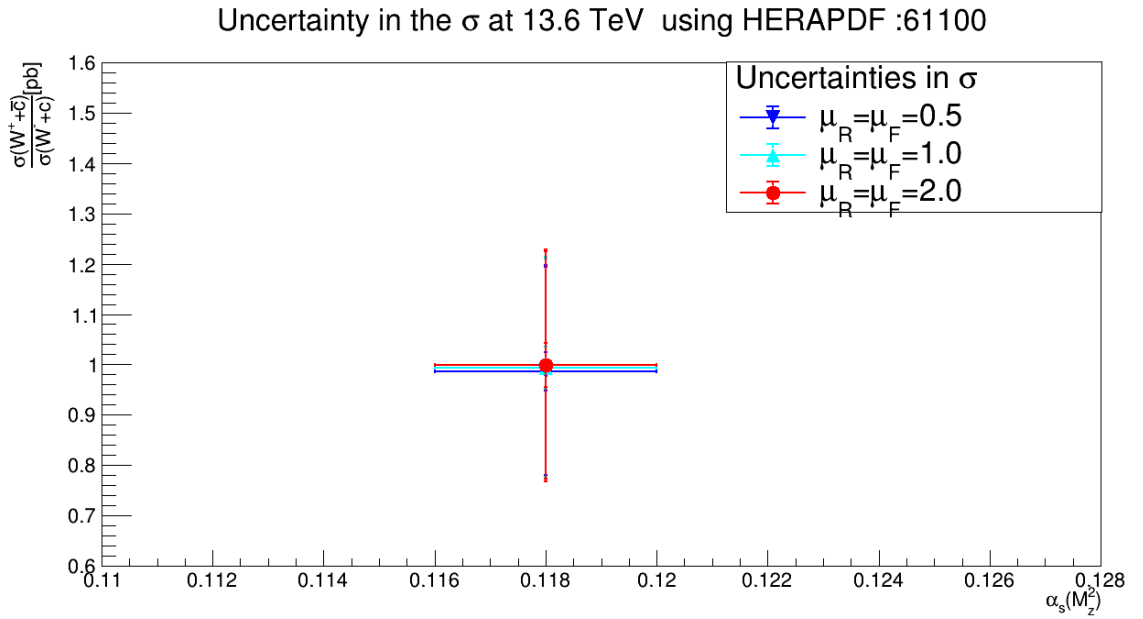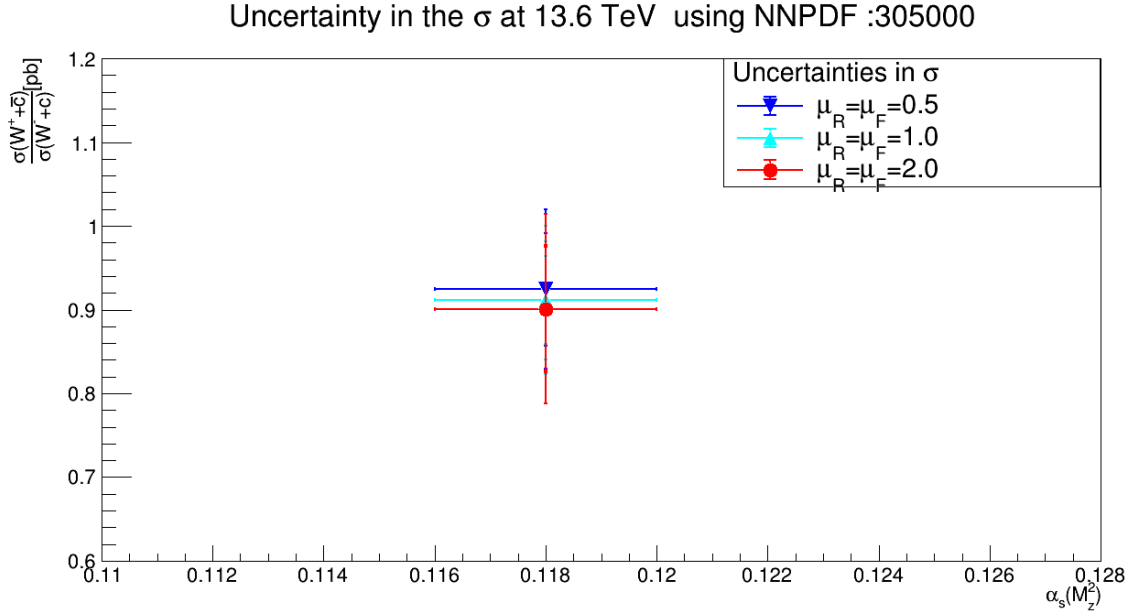
Figure 4.10: Plots (a) and (b) show the predicted change in cross section of $W + c$, (c) and (d) show the predicted change in the cross section of $W^+ + \bar{c}$, (e) and (f) show the predicted change in cross section of $W^- + c$ while (g) and (h) show the predicted change in cross section at different QCD scale (μ_R and μ_F) at 13.6 TeV. The vertical error bars represent: inner (PDF), middle (α_s), outer (PDF+α_s combined) errors.

(a)

(b)

(a)

(b)

(c)

(d)

(e)

(f)
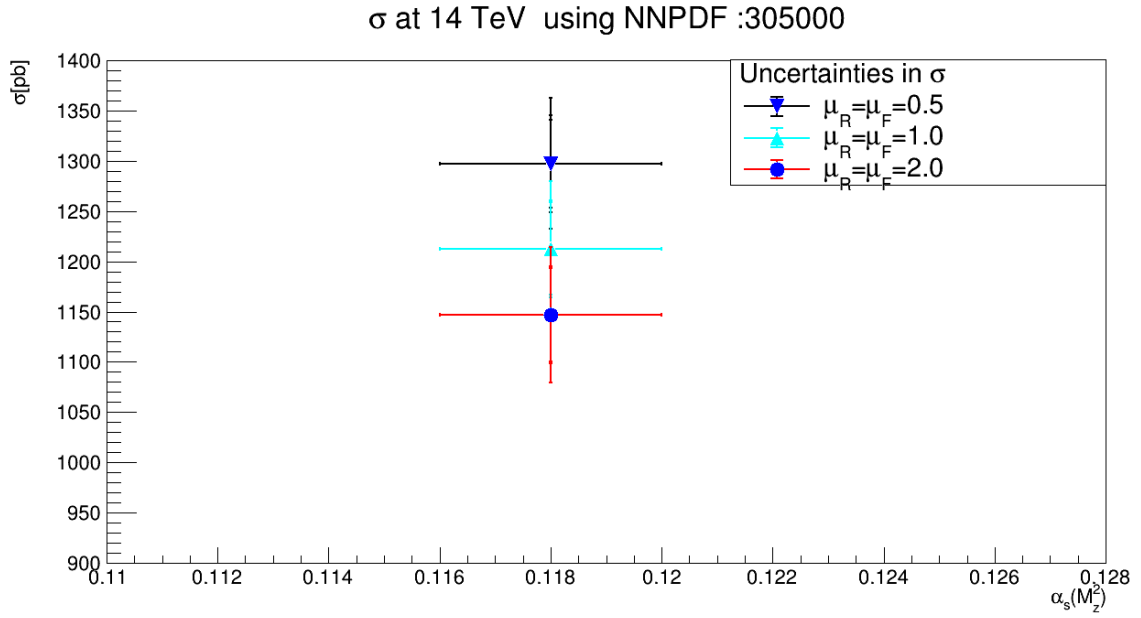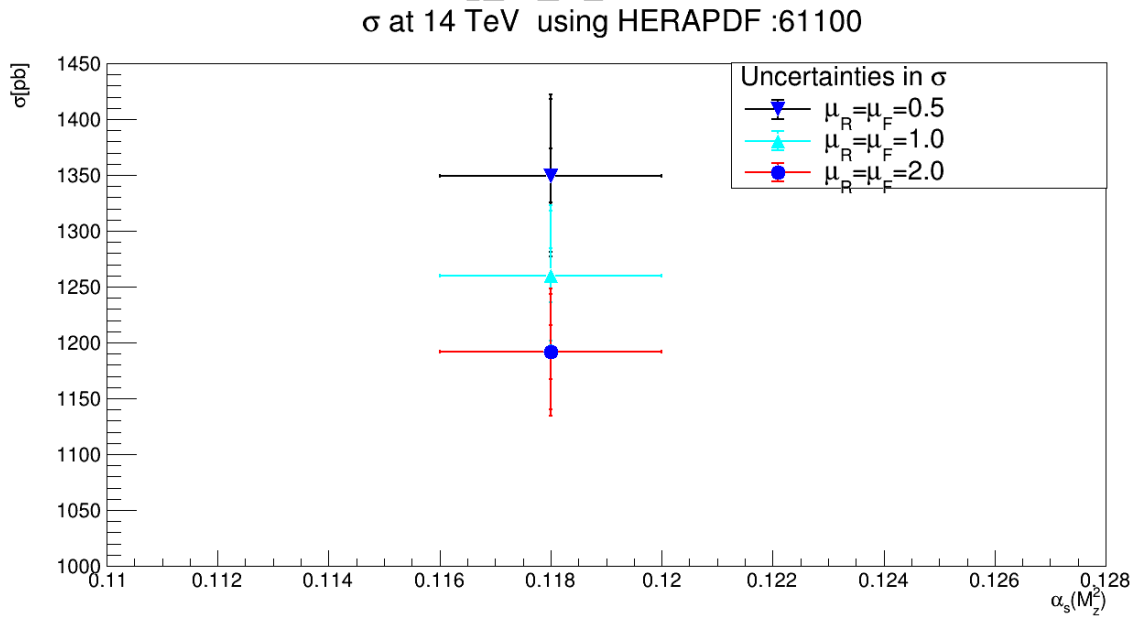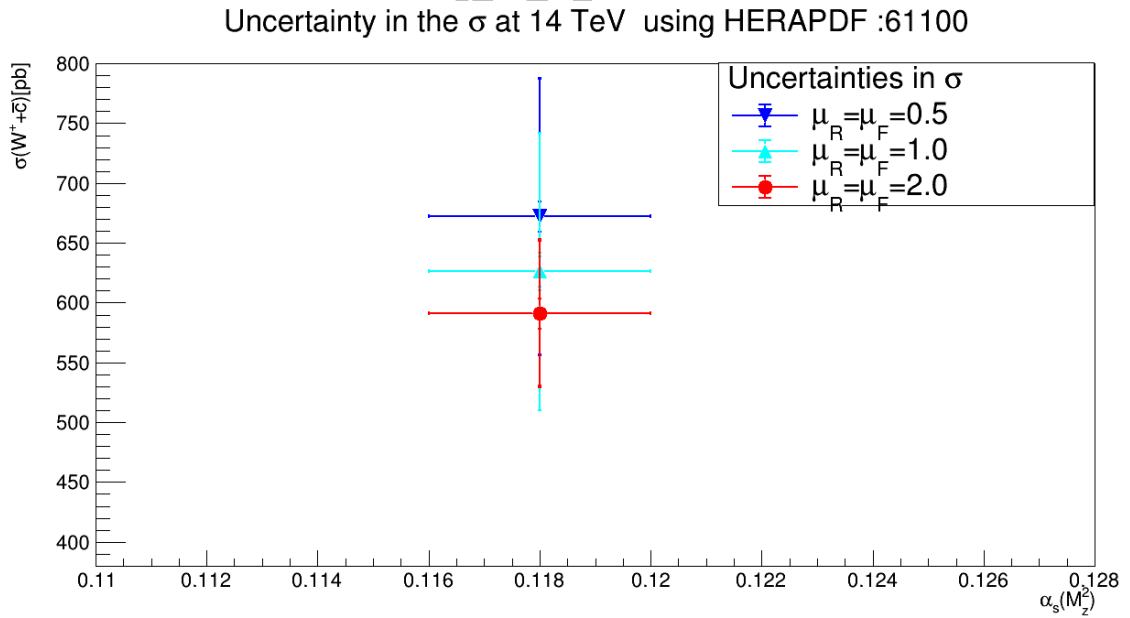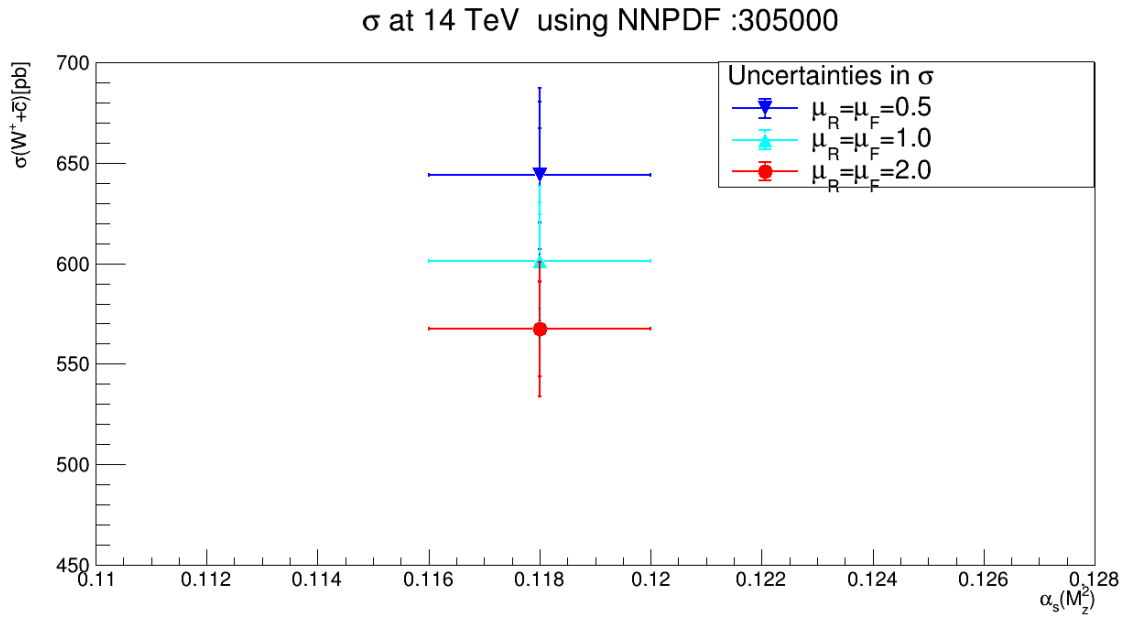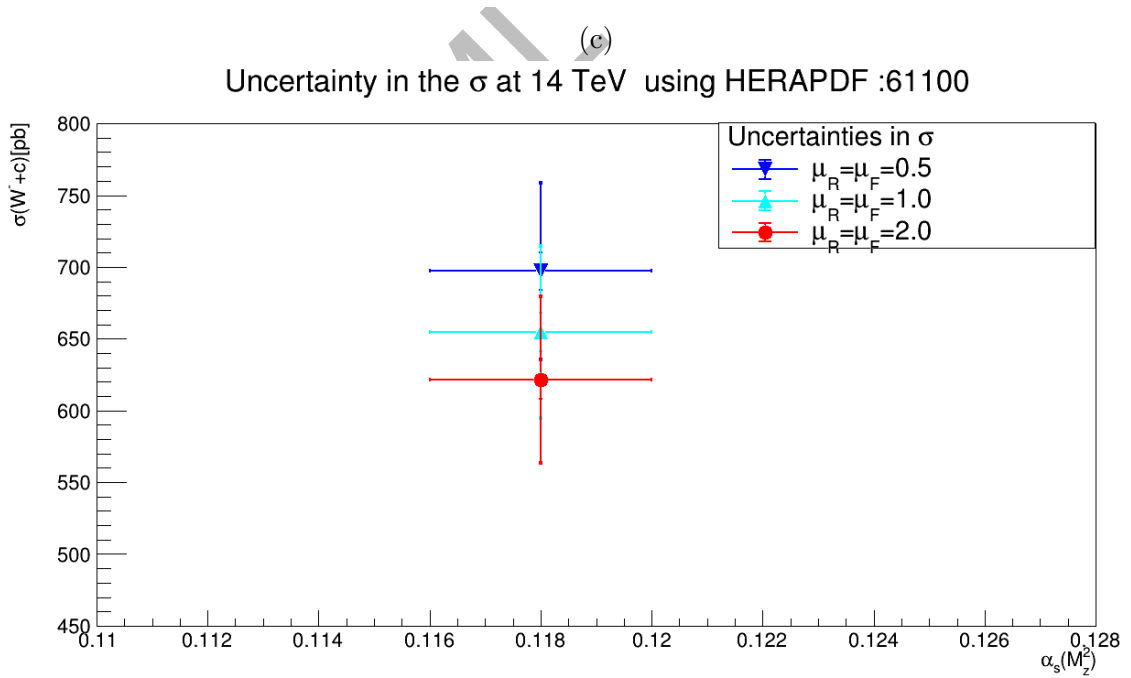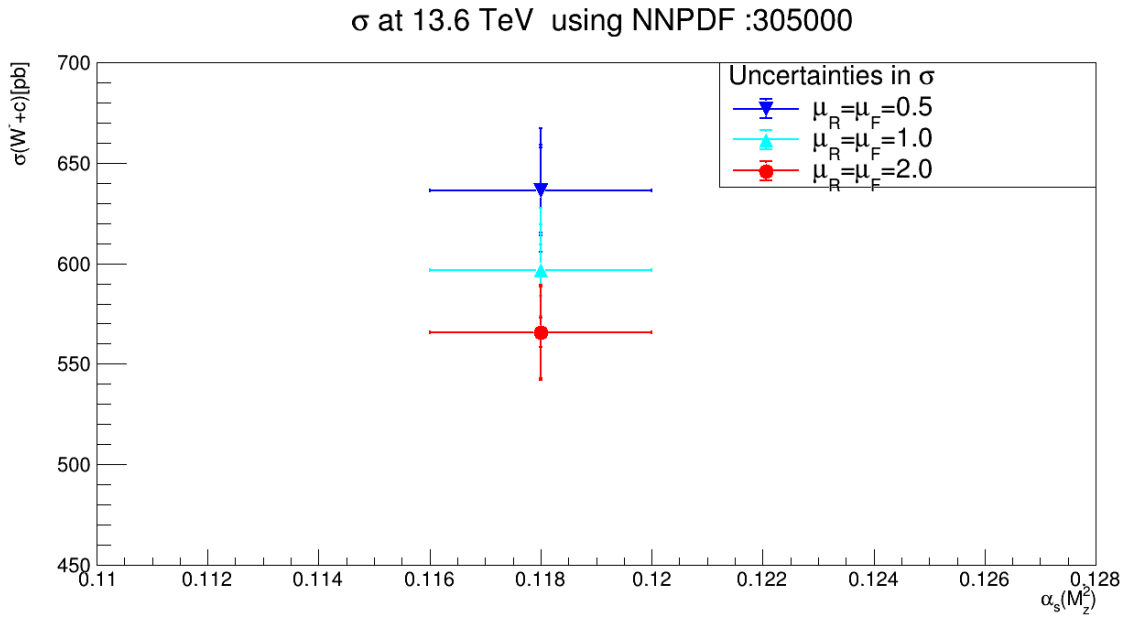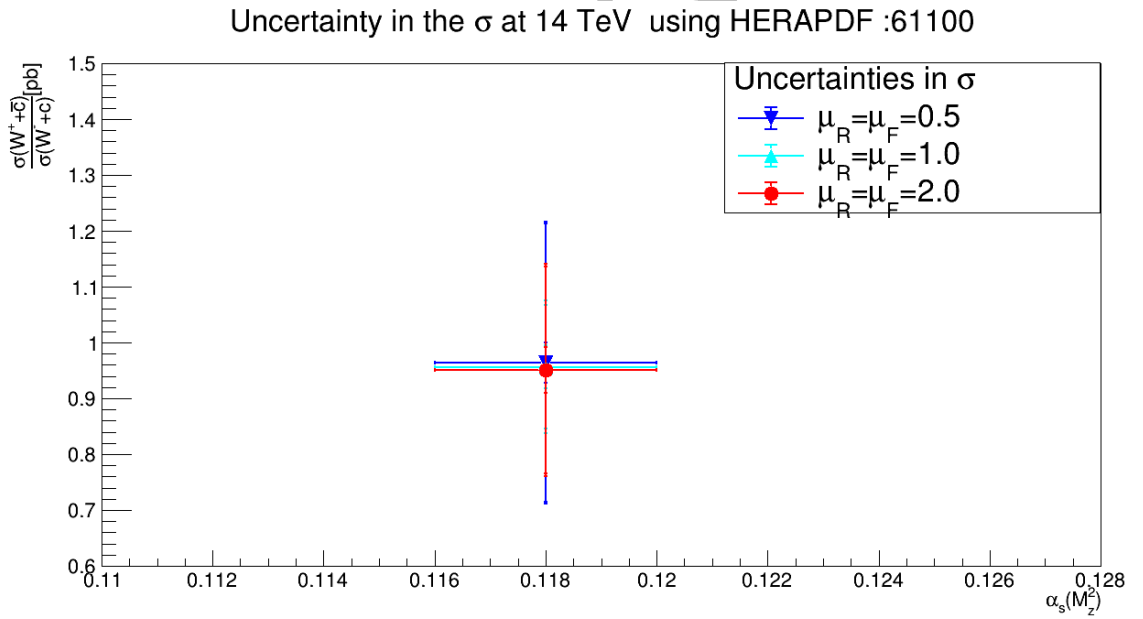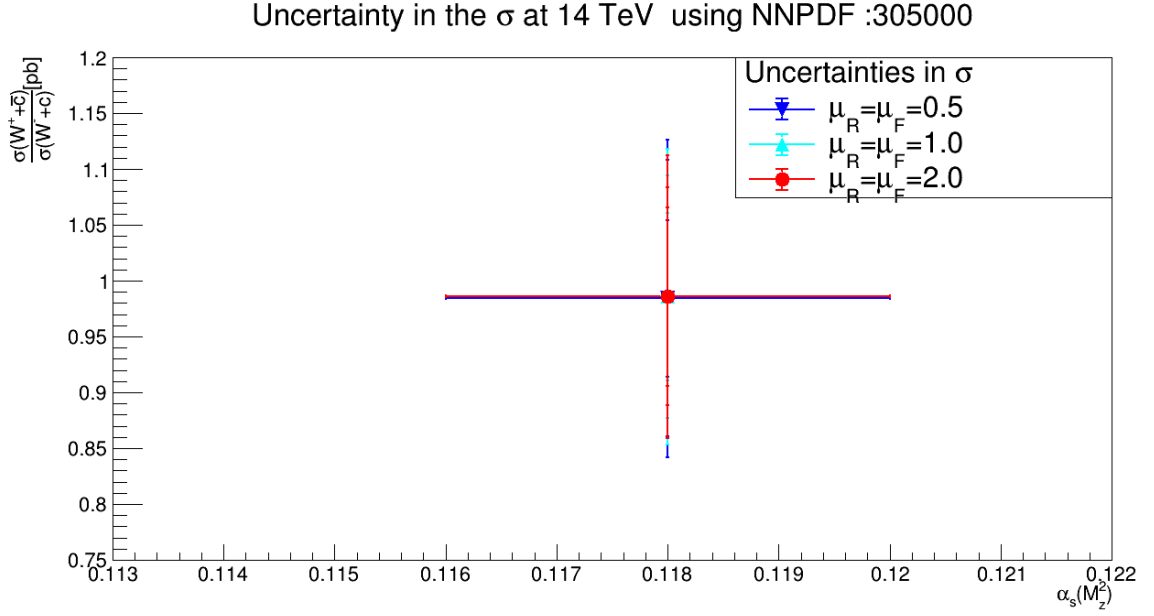
Figure 4.12: Plots (a) and (b) show the predicted change in cross section of $W + c$, (c) and (d) show the predicted change in the cross section of $W^+ + \bar{c}$, (e) and (f) show the predicted change in cross section of $W^- + c$ while plots (g)and (h) show the predicted change in cross section at different QCD scale (μ_R and μ_F) at 14 TeV. The vertical error bars represent: inner (PDF), middle (α_s), outer (PDF+α_s combined) errors.

4.7 Conclusion

The measurement of $W + c$ cross section in proton-proton collisions at LHC gives vital information about the flavour composition of proton quark sea and does agree with neutrino scattering experiments.

The production cross section of W-boson and charm quark is studied in detail in this thesis. The measured results at 7 TeV and 13 TeV are compared with the predicted cross sections calculated for different PDFs. There is high degree of agreement between the observed and the predicted values.

The inclusive and differential measurements are also compared to theoretical predictions obtained using the MADGRAPH in combination with several sets of parton distribution functions at next-to-leading order of QCD. For all calculations using global PDF sets, there is good agreement between the measurements and the theoretical predictions.

We also studied about various uncertainties in the predictions which include PDF, α_s and QCD scale uncertainties.

We also developed theoretical prediction at various QCD scales for $W + c$ production cross section at 13 TeV, 13.6 TeV and 14 TeV. The results of 13.6 TeV and 14 TeV can be compared to the observations when data at these CoM energy values will be available. We expect the calculations to agree with the experimental results as was the case for previous energies.

List of Figures

List of Tables

Bibliography

[1] Kenneth Aamodt, A Abrahantes Quintana, R Achenbach, S Acounis, D Adamová, C Adler, M Aggarwal, F Agnese, G Aglieri Rinella, Z Ahammed, et al. The alice experiment at the cern lhc. *Journal of Instrumentation*, 3(08):S08002, 2008.

[2] S Alekhin, J Blümlein, S Klein, and S Moch. 3-, 4-, and 5-flavor next-to-next-to-leading order parton distribution functions from deep-inelastic-scattering data and at hadron colliders. *Physical Review D*, 81(1):014032, 2010.

[3] Johan Alwall, R Frederix, S Frixione, V Hirschi, Fabio Maltoni, Olivier Mattelaer, H-S Shao, T Stelzer, P Torrielli, and M Zaro. The automated computation of tree-level and next-to-leading order differential cross sections, and their matching to parton shower simulations. *Journal of High Energy Physics*, 2014(7):1–157, 2014.

[4] Johan Alwall, Michel Herquet, Fabio Maltoni, Olivier Mattelaer, and Tim Stelzer. Madgraph 5: going beyond. *Journal of High Energy Physics*, 2011(6):1–40, 2011.

[5] Manuel Bähr, Stefan Gieseke, Martyn A Gigg, David Grellscheid, Keith Hamilton, Oluseyi Latunde-Dada, Simon Plätzer, Peter Richardson, Michael H Seymour, Alexander Sherstnev, et al. Herwig++ physics and manual. *The European Physical Journal C*, 58(4):639–707, 2008.

[6] Richard D. Ball, Valerio Bertone, Luigi Del Debbio, Stefano Forte, Alberto Guffanti, José I. Latorre, Simone Lionetti, Juan Rojo, and Maria Ubiali. Precision nnlo determination of s(mz) using an unbiased global parton set. *Physics Letters B*, 707(1):66–71, 2012.

[7] GL Bayatian, A Korablev, A Soha, O Sharif, M Chertok, W Mitaroff, F Pauss, V Genchev, M Wensveen, V Lemaitre, et al. Cms physics: Technical design report volume 1: Detector performance and software. Technical report, CMS-TDR-008-1, 2006.

[8] GL Bayatian, A Korablev, A Soha, O Sharif, M Chertok, W Mitaroff, F Pauss, V Genchev, M Wensveen, V Lemaitre, et al. Cms physics: Technical design report volume 1: Detector performance and software. Technical report, CMS-TDR-008-1, 2006.

[9] AO Bazarko, CG Arroyo, KT Bachmann, T Bolton, C Foudas, BJ King, WC Lefmann, WC Leung, SR Mishra, E Oltman, et al. Determination of the strange quark content of the nucleon from a next-to-leading-order qcd analysis

of neutrino charm production. *Zeitschrift für Physik C Particles and Fields*, 65(2):189–198, 1995.

[10] James D Bjorken. Asymptotic sum rules at infinite momentum. *Physical Review*, 179(5):1547, 1969.

[11] B. Blok and P. Gunnellini. Dynamical approach to MPI in W+dijet and Z+dijet production within the PYTHIA event generator. *Eur. Phys. J. C*, 76(4):202, 2016.

[12] Geoffrey T Bodwin. Factorization of the drell-yan cross section in perturbation theory. *Physical Review D*, 31(10):2616, 1985.

[13] R Brandelik, W Braunschweig, K Gather, V Kadansky, K Lübelsmeyer, P Mättig, H-U Martyn, G Peise, J Rimkus, HG Sander, et al. Evidence for planar events in e+ e- annihilation at high energies. *Physics Letters B*, 86(2):243–249, 1979.

[14] L Camilleri, D Cundy, P Darriulat, J Ellis, John Field, H Fischer, E Gabathuler, MK Gaillard, H Hoffmann, K Johnson, et al. Physics with very high energy e+ e-colliding beams. Technical report, European Organization for Nuclear Research, 1976.

[15] Sergey Chatrchyan, Vardan Khachatryan, A Sirunyan, V Chiochia, Ben Kilminster, and P Robmann. Measurement of associated w + charm production in pp collisions at sqrt(s) = 7 tev. 01 2014.

[16] ATLAS Collaboration, G Aad, E Abat, J Abdallah, AA Abdelalim, A Abdesselam, O Abdinov, BA Abi, M Abolins, H Abramowicz, et al. The atlas experiment at the cern large hadron collider, 2008.

[17] CMS Collaboration, S Chatrchyan, G Hmayakyan, V Khachatryan, AM Sirunyan, W Adam, T Bauer, T Bergauer, H Bergauer, M Dragicevic, et al. The cms experiment at the cern lhc, 2008.

[18] CMS Collaboration, C Collaboration, et al. The cms hadron calorimeter project: Technical design report, technical design report cms. *CERN, Geneva*, 1997.

[19] Cms Collaboration et al. The cms electromagnetic calorimeter project: technical design report. *Technical Design Report CMS. CERN, Geneva*, 47, 1997.

[20] CMS collaboration et al. Measurements of the associated production of a w boson and a charm quark in proton-proton collisions at $\backslash\sqrt{\{s\}} = 8$ tev. *arXiv preprint arXiv:2112.00895*, 2021.

[21] CMS collaboration et al. Measurements of the associated production of a w boson and a charm quark in proton-proton collisions at $\backslash\sqrt{\{s\}} = 8$ tev. *arXiv preprint arXiv:2112.00895*, 2021.

[22] LHCb Collaboration, A Augusto Alves, LM Andrade Filho, AF Barbosa, I Bediaga, G Cernicchiaro, G Guerrer, HP Lima, AA Machado, J Magnin, et al. The lhcb detector at the lhc. *Journal of instrumentation*, 3(08):S08005–S08005, 2008.

[23] John C Collins, Davison E Soper, and George Sterman. Factorization for short distance hadron-hadron scattering. *Nuclear Physics, Section B*, 261(C):104–142, 1985.

[24] Gennaro Corcella, Ian G. Knowles, Giuseppe Marchesini, Stefano Moretti, Kosuke Odagiri, Peter Richardson, Michael H. Seymour, and Bryan R. Webber. Herwig 6: an event generator for hadron emission reactions with interfering gluons (including supersymmetric processes). *Journal of High Energy Physics*, 2001(01):010, feb 2001.

[25] TH Eichten, Helmut Faissner, FJ Hasert, S Kabe, W Krenz, J Von Krogh, J Morfin, K Schultze, GH Bertrand-Coremans, Jean Sacton, et al. Measurement of the neutrino-nucleon and antineutrino-nucleon total cross sections. *Physics Letters B*, 46(2):274–280, 1973.

[26] Lyndon Evans and Philip Bryant. Lhc machine. *Journal of instrumentation*, 3(08):S08001, 2008.

[27] Walter T Giele, EW Nigel Glover, and David A Kosower. Higher-order corrections to jet cross sections in hadron colliders. *Nuclear Physics B*, 403(3):633–667, 1993.

[28] WT Giele and EW Nigel Glover. Higher-order corrections to jet cross sections in e+ e- annihilation. *Physical Review D*, 46(5):1980, 1992.

[29] T. Gleisberg, Stefan. Hoeche, F. Krauss, M. Schonherr, S. Schumann, F. Siegert, and J. Winter. Event generation with SHERPA 1.1. *JHEP*, 02:007, 2009.

[30] M. Goncharov et al. Precise Measurement of Dimuon Production Cross-Sections in ν_μ Fe and $\bar{\nu}_\mu$ Fe Deep Inelastic Scattering at the Tevatron. *Phys. Rev. D*, 64:112006, 2001.

[31] Kaoru Hagiwara, K Hikasa, Kenzo Nakamura, M Tanabashi, M Aguilar-Benitez, CD Amsler, Matthew Robert Barnett, PR Burchat, CD Carone, C Caso, et al. Review of particle physics: Particle data group. *Physical Review D*, 66(1 I):100011–10001958, 2002.

[32] Vardan Khachatryan, D Anderson, A Apresyan, A Bornheim, J Bunn, Y Chen, J Duarte, A Mott, HB Newman, C Pena, et al. The cms trigger system. *Journal of Instrumentation*, 12(1):Art–No, 2017.

[33] Christiane Lefevre. The cern accelerator complex. Technical report, 2008.

[34] Michael Leyton, Bernhard Meirose, Kendall Reeves, M Aaboud, G Aad, B Abbott, J Abdallah, SH Abidi, Joseph M Izen, ATLAS Collaboration, et al. Measurement of the w-boson mass in pp collisions at s= 7 tev with the atlas detector. 2018.

[35] Don Bernett Lichtenberg and S Peter Rosen. Developments in the quark theory of hadrons. 1980.

[36] Alan D Martin, W James Stirling, Robert S Thorne, and G Watt. Parton distributions for the lhc. *The European Physical Journal C*, 63(2):189–285, 2009.

[37] Guthrie Miller, ED Bloom, G Buschhorn, DH Coward, H DeStaebler, J Drees, CL Jordan, Luke W Mo, Richard E Taylor, Jerome I Friedman, et al. Inelastic electron-proton scattering at large momentum transfers and the inelastic structure functions of the proton. *Physical Review D*, 5(3):528, 1972.

[38] Pavel M Nadolsky, Hung-Liang Lai, Qing-Hong Cao, Joey Huston, Jon Pumplin, Daniel Stump, Wu-Ki Tung, and C-P Yuan. Implications of cteq global analysis for collider observables. *Physical Review D*, 78(1):013004, 2008.

[39] Carlo Oleari. The POWHEG-BOX. *Nucl. Phys. B Proc. Suppl.*, 205-206:36–41, 2010.

[40] Keith A Olive, Kaustubh Agashe, Claude Amsler, Mario Antonelli, Jean-Francois Arguin, David M Asner, H Baer, Henry R Band, RM Barnett, Tullio Basaglia, et al. Review of particle physics. *Chinese physics C*, 38(9):090001, 2014.

[41] Oleg Samoylov, R Petti, S Alekhin, P Astier, D Autiero, A Baldisseri, M Baldo-Ceolin, M Banner, G Bassompierre, K Benslama, et al. A precision measurement of charm dimuon production in neutrino interactions from the nomad experiment. *Nuclear Physics B*, 876(2):339–375, 2013.

[42] Albert M Sirunyan, CMS Collaboration, et al. Performance of the cms muon detector and muon reconstruction with proton-proton collisions at s= 13 tev. 2018.

[43] Torbjörn Sjöstrand, Stephen Mrenna, and Peter Skands. A brief introduction to pythia 8.1. *Computer Physics Communications*, 178(11):852–867, 2008.

[44] Torbjörn Sjöstrand, Stephen Mrenna, and Peter Skands. A brief introduction to pythia 8.1. *Computer Physics Communications*, 178(11):852–867, 2008.

[45] Graeme Watt. Mstw pdfs and impact of pdfs on cross sections at tevatron and lhc. *Nuclear Physics B-Proceedings Supplements*, 222:61–80, 2012.